Using Statistical Emulation for Sensitivity Studies of Deep Convective Clouds

Zur Erlangung des akademischen Grades eines

DOKTORS DER NATURWISSENSCHAFTEN

von der KIT-Fakultät für Physik des

Karlsruher Instituts für Technologie (KIT)

genehmigte

DISSERTATION

von

M. Sc. Marie-Constanze Monika Wellmann, geb. Fischerkeller

aus Karlsruhe

Abstract

Severe storms have a large damage potential. Heavy precipitation, strong wind gusts and hail cause damage to buildings, infrastructure and crops. Therefore, the accurate modeling and the reliable prediction of severe storms and deep convective clouds are of interest in atmospheric research. Especially, it is necessary to better understand how changes in the environmental conditions and the model microphysics feed back into the dynamics and the development of deep convective clouds.

This study aims to identify those environmental conditions and microphysical parameters such as wind shear and strength of ice multiplication that lead to large uncertainties in the prediction of deep convective clouds. In an idealized setup of the cloud-resolving COSMO model including a two-moment microphysics scheme, the approach of statistical emulation is used to allow for a Monte Carlo sampling of the parameter space. This enables a comprehensive sensitivity analysis where the extended Fourier amplitude sensitivity test is used. Furthermore, it is investigated whether the sensitivities are robust for different trigger mechanisms of convection. Thus, the results are compared for three setups where the convection is triggered by either a warm bubble, a cold pool or flow over orography. In this thesis the analysis focuses on the vertically integrated content of six hydrometeor classes, the precipitation, the size distribution of surface hail and diabatic heating rates.

First, the impact of uncertainty in environmental conditions (cloud condensation nuclei concentration, ice nuclei concentration, wind shear, vertical temperature profile and trigger characteristics) on the output uncertainty is analyzed. It is found that the temperature profile and the cloud condensation nuclei number are the largest contributors to the uncertainties of the considered outputs. In addition, the wind shear contributes substantially to the uncertainty of these variables in the orography setup.

Second, uncertainty in seven cloud microphysics parameters (cloud condensation nuclei condensation, ice nuclei concentration, fall velocities of rain, graupel and hail, strength of ice multiplication and the size distribution of cloud droplets) is used for the sensitivity analysis. Here, three important input parameters can be identified. The cloud condensation nuclei concentration contributes to the uncertainties of the precipitation output and the diabatic heating rates while the fall velocity of graupel contributes to the uncertainties of the integrated hydrometeor contents and the diabatic heating rates. Moreover, the fall velocity of hail causes uncertainty in the prediction of the precipitation and the size distribution of surface hail.

Based on the results of the aforementioned analyses, the largest contributors to the uncertainty of both the environmental conditions and the microphysics (cloud condensation nuclei concentration, ice nuclei concentration, wind shear, vertical temperature profile and the fall velocities of graupel and hail) are

combined in a third analysis to determine the relative impact of the environmental conditions compared to microphysical parameters. The comparison reveals that in general the effect of the environmental conditions and the microphysics is comparable. Yet it depends on the output of interest as, for example, the microphysical parameters dominate the uncertainty of the precipitation whereas the uncertainty of the diabatic heating rate is controlled by environmental conditions.

Further, the results show that depending on the choice of the trigger mechanism, the contribution of the input parameters to the uncertainty varies where the largest differences are found between the orography setup and the thermal triggers. Thus, sensitivities obtained for one trigger mechanism cannot be completely transferred to other triggers.

Contents

1. Introduction

Severe storms are considered as natural hazards because of their large damage potential. Flooding caused by heavy precipitation, strong wind gusts and hail lead to serious damage to buildings, infrastructure and crops. For example, Germany was hit by two severe supercells on 27/28 July 2013 (Kunz et al., 2018) causing insured losses of USD 3.8 billion (SwissRe, 2014). Thus, the accurate modeling and the reliable prediction of severe storms and deep convective clouds are of interest in atmospheric research. Especially, it is necessary to better understand how changes in the environmental conditions and the model microphysics feed back into the dynamics and the development of deep convective clouds.

There are many studies investigating the impact of various parameters on deep convective clouds. As the wind shear is an important parameter controlling the organizational form of convective systems, its impact on deep convection has been examined over several decades (Schlesinger, 1978; Weisman and Klemp, 1984; Weisman and Rotunno, 2000; Dennis and Kumjian, 2017). The combined effect of the wind shear and the convective available potential energy (CAPE) is analyzed by Lee et al. (2008). In recent years, numerous studies have been published regarding the sensitivity of deep convective clouds to the concentration of cloud condensation nuclei (CCN) and aerosol load (Tao et al., 2007, 2012; Rosenfeld et al., 2008; Noppel et al., 2010; Khain et al., 2011; Cui et al., 2011; Morrison, 2012; Fan et al., 2013; Yang et al., 2017). However, the general outcome of these studies is not consistent and research is still ongoing. Furthermore, other microphysical processes such as the ice multiplication introduced by Hallet and Mossop (1974) are found to affect the composition of clouds for both simulations and observations (Phillips et al., 2007, 2017; Connolly et al., 2006; Crosier et al., 2011). Additional parameters influencing the prediction of precipitation are the fall speeds of hydrometeors which are parameterized according to empirical relations obtained from observations (Locatelli and Hobbs, 1974; Knight and Heymsfield, 1983; Yuter et al., 2006). Moreover, there are different mechanisms commonly used to trigger convection in model simulations such as a warm bubble (Weisman and Klemp, 1982; Storer et al., 2010), a cold pool (Adams-Selin et al., 2013) or orography (Chen and Lin, 2005).

These publications indicate that there are several parameters affecting the formation of deep convective clouds and the corresponding in-cloud processes. Therefore, the aim of this work is to address the following questions:

- Which parameters cause the main uncertainty in the predictions of convective cloud parameters? In particular also of hail occurrence and size?

- How much are the diabatic heating rates affected by variations of the input parameters?

- Are the results robust for different trigger mechanisms of deep convection?

So, here a comprehensive sensitivity study is conducted to determine the effect of both environmental conditions and model microphysics on the uncertainty of the prediction of deep convection. In idealized high-resolution model simulations selected input parameters are modified and their effect on the model output is analyzed. First, only parameters describing environmental conditions such as wind shear or vertical temperature profile are considered. Second, the impact of microphysical parameters like the strength of the ice multiplication and the fall speed of graupel is analyzed. In a third study, the set of input parameters is a combination of parameters describing environmental conditions and microphysics.
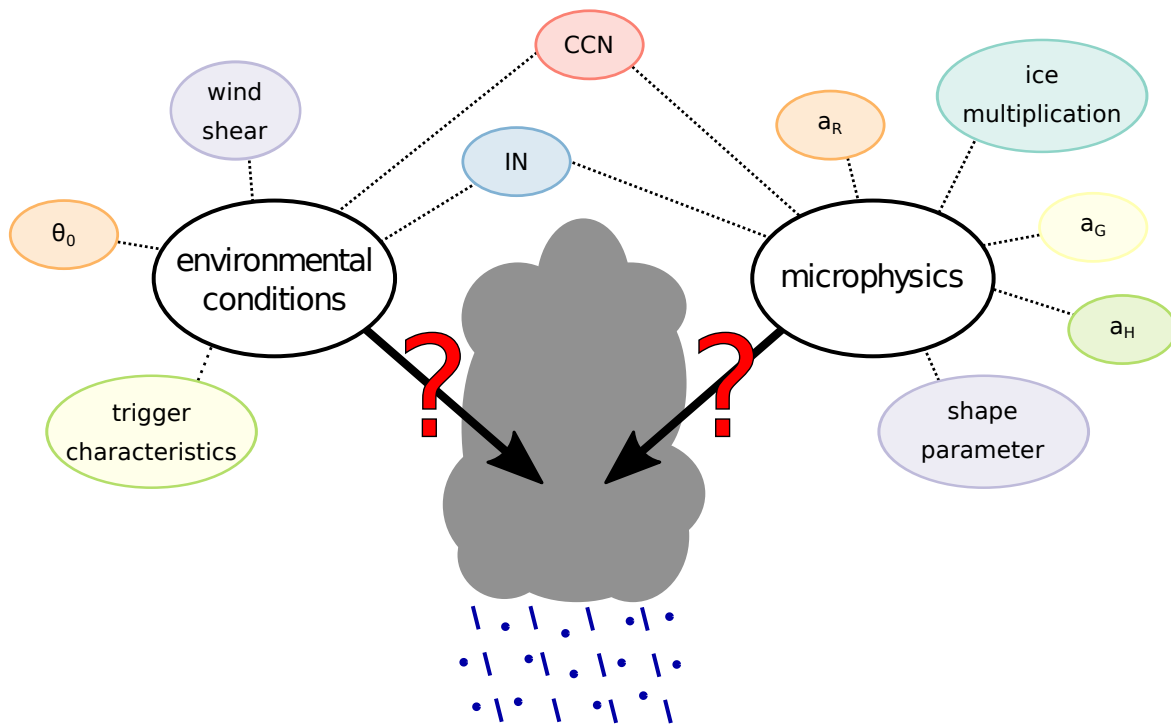
Fig. 1.1.: Schematic overview of the sensitivity studies conducted in this thesis. In a first study, the impact of environmental conditions on the prediction of deep convection and precipitation is analyzed. Second, the effect of the model microphysics is evaluated. The last study combines both environmental conditions and microphysics. The colored bubbles denote the considered parameters. Further descriptions are given in sections 4.3.1 and 4.4.1.

In general, the approach for the analysis of the sensitivity of model output to some input parameters is to vary a chosen parameter in a given range while other parameters are kept constant. This so-called *one-at-a-time* (OAT) analysis is applicable if the impact of a single model input is of interest. However, not only the effect of each input parameter independently should be assessed in this study, but also the amount of interactions that are happening between those parameters. In addition, the relative contribution of the input parameters to the uncertainty of the output is of interest. Hence, the methods of statistical emulation (O'Hagan, 2004, 2006) and variance-based sensitivity analysis (Saltelli, 2008) are applied where the uncertainty of the output is decomposed into the contributions of the individual model input parameters while simultaneously considering their interactions. The applicability of this approach for complex atmospheric models is demonstrated in Lee et al. (2011), Lee et al. (2013) and Johnson et al. (2015).

Chapter 2 gives an overview of previous research and the current understanding of deep convective clouds and affecting parameters. The methods of statistical emulation and variance-based sensitivity analysis are explained in chapter 3 followed by a general description of the model setup and the considered output variables in chapter 4. The results of the sensitivity analyses are presented in chapter 5 for different environmental conditions, in chapter 6 for perturbations of the microphysics and in chapter 7 for the set of input parameters combining environmental conditions and microphysics. A comparison of the results for the different sets of input parameters is found in chapter 8. Chapter 9 contains the summary and conclusions.

2. Previous Research and Scientific Context

Up to the present day numerous studies have been published on simulating deep convective clouds. Consequently, it has been investigated how various parameters affect the clouds in these simulations. The vertical wind profile has an apparent effect on the organization of convection and thus it has been analyzed since several decades. Vertical wind shear, directional shear in particular, determines the structure of deep convection such as separating up- and downdrafts which leads to an enhanced lifetime of storms. Moreover, strong wind shear induces pressure perturbations within the cloud that produce acceleration due to pressure gradients favoring the development of supercells (Houze, 1993). Schlesinger (1978) performs simulations of storms for either no wind shear, unidirectional shear or multi-directional shear. The comparison of the results reveals that in the mature stage, the storms become stronger and more persistent for increasing wind shear. At the same time rainfall is reduced while the in-cloud water content is increased. However, the ice phase is not included in their simulations. A similar study is conducted by Weisman and Klemp (1984). Here, the wind vector turns $180°$ in the lowest 5 km in each of the simulations while the wind velocity is varied. They find that the structure of the storm is determined by the wind shear. Single cells are detected for low wind shear, multicellular convection for medium wind shear and supercells for high wind shear. Yet, precipitation is not considered in their study. In contrast, Dennis and Kumjian (2017) analyze the impact of wind shear on deep convective clouds focusing on hail. The quarter circle profile of Weisman and Rotunno (2000) is used as initial wind profile. To alter the wind shear, the maximum wind speeds u_{max} and v_{max} reached in x- and y-direction, respectively, are increased. This elongates the hodograph either in north-south or east-west direction. If u_{max} is increased, statistically significant more hail is detected in the simulation. As the process rates are differing only slightly between the simulations, they find that by elongating the hodograph, the volume in which hail is produced becomes larger. If v_{max} is increased, the volume favoring hail production is reduced and thus less hail is detected.

Another parameter influencing deep convection is CAPE. It is defined as the integrated buoyancy of an air parcel between the level of free convection and the equilibrium level. In addition, the maximum vertical velocity in the updraft can be estimated by $w = \sqrt{2 \cdot \text{CAPE}}$ assuming that all of the potential energy is transformed into kinetic energy of an ascending air parcel. Therefore, higher values of CAPE are related to strong convection and severe weather (Lamb and Verlinde, 2011). Chen and Lin (2005) investigate the impact of variations of the unsaturated moist Froude number and CAPE on convection where they use flow over orography as convection trigger in their simulations. The results can be divided into

four different regimes of cloud structures which depend on the combination of the two considered parameters. For example, one regime is characterized by long-lasting convection over the mountain whereas another regime additionally includes a downstream propagating cloud system. Information about the impact on precipitation is not given.

Over the last decade the impact of the CCN concentration on clouds and climate has become a focus of research. In general, an increase of the CCN concentration is connected to a delay of precipitation and an extended lifetime of the clouds (Rosenfeld et al., 2008). In clean conditions with a low CCN concentration, there are few large cloud droplets which easily grow into raindrops falling to the ground leading to dissipation of the cloud. Contrary, in polluted conditions, approximately the same amount of water is distributed over a larger number of CCN leading to more numerous but smaller cloud droplets. These small droplets are less likely to collide and coalesce with other hydrometeors such that the growth of the hydrometeors and the formation of precipitation are slowed down. As the water remains in the cloud, the small droplets are lifted to heights above to freezing level. These supercooled droplets can form precipitation via the ice phase which precipitates in a later stage of the life cycle of the cloud. The diverse results of numerous studies indicate that the aerosol effect depends on various parameters such as wind shear and CAPE. Tao et al. (2007) simulate three deep convective cloud systems over different areas of the US. In all cases an increase of the CCN concentration leads to the suppression of rain in early stages, but in mature stages opposite effects are found. Precipitation is suppressed for a storm over Oklahoma and there is no effect for a storm over Florida whereas precipitation is enhanced for a storm over the Pacific. A hailstorm over Germany is simulated by Noppel et al. (2010) where the cloud droplet size distribution and the CCN concentration are varied. For some size distributions, the accumulated precipitation decreases for an increasing CCN concentration while for other size distributions an increase is observed. Overall, their results show a lower amount of hail for polluted conditions. Khain et al. (2011) simulate the same hailstorm using a different model. Besides the CCN concentration they also perturb the temperature gradient in the boundary layer. In contrast to Noppel et al. (2010), they find that an increase of the CCN concentration is linked to an increase of accumulated precipitation, especially an increase of hail mass and size. It can be assumed that these contrasting results arise from the use of different models including different microphysics schemes. The work of Morrison (2012) focuses on idealized supercell storms. During their simulations, different microphysical and thermodynamical processes are either turned on or off. Their analysis reveals that in some cases a weakening and in other cases an invigoration of the storm happens. Thus, the effect of the CCN concentration has opposite signs. Combined studies regarding the impact of several parameters are conducted by Lee et al. (2008) and Storer et al. (2010). Lee et al. (2008) analyze the effect of the CCN concentration on deep convective clouds for different regimes of wind shear and CAPE. On the one hand, an increase of the CCN concentration leads to more precipitation in environments with high CAPE and strong wind shear. On the other hand, a reduction of precipitation is found for an increasing CCN concentration in environments with low CAPE

and low wind shear. Storer et al. (2010) compare the effects of the CCN concentration and the CAPE. Different thermodynamic profiles are used to vary the CAPE. They see a higher amount of cloud water and ice and also more precipitation for high CAPE values. When the CCN concentration is increased, they detect more small cloud droplets and simultaneously a reduction of precipitation. They conclude that the relative impact of both parameters is comparable.

Not only thermodynamic profiles and environmental conditions affect the formation and structure of deep convective clouds, but also parameters related to cloud microphysics are of importance. Splinters of ice particles, which can be generated during the riming process, favor the growth of ice from both the vapor and liquid phase because of their crystal lattice structure (Houze, 1993). This process of secondary ice production was introduced by Hallet and Mossop (1974) who measured the number of ice particles in a chamber where rime was grown on a metal rod. They detected a decrease of the number of ice particles if the rod was not rimed. Thus, it is also referred to as Hallet-Mossop process. Phillips et al. (2007) identify the relevance of the Hallett-Mossop process in cloud simulations. They simulate two cases of deep convection over the tropical Pacific and find that the Hallet-Mossop process controls the ice particle concentration in the lower part of the mixed-phase region of the clouds. Connolly et al. (2006) simulate a thunderstorm over northern Australia to examine the impact of the CCN concentration and the ice nuclei (IN) concentration including variations of the strength of the Hallet-Mossop process. The results show that the height of the cloud top depends on the strength of the Hallet-Mossop process whereas the mean precipitation is rather insensitive to these changes.

Further relevant parameters are the size distributions and the fall speeds of hydrometeors. Moderate differences in the size of the particles result in a high collision efficiency. In contrast, the smaller the hydrometeors are and thus the larger the difference in size, the more the collision efficiency is reduced as the small particles rather follow the streamlines around the larger particles than colliding with them. Furthermore, a higher fall velocity, in particular of the larger hydrometeors, increases the volume in which smaller particles can be collected and thus the growth process is accelerated. In their study, Igel and van den Heever (2017) vary the shape parameter of the cloud droplet size distribution in simulations of shallow cumulus clouds. They notice an impact of this variation on the cloud droplet number concentration, the droplet diameter and the cloud fraction. They mention that some of these effects are on the same order of magnitude as aerosol effects. However, the impact on precipitation is not identified as the investigated cloud are non-precipitating. Adams-Selin et al. (2013) investigate the effect of graupel size and thus also of the fall speed on deep convection. The simulations are run for different sizes of graupel and in one case graupel is removed from the model. Their results show that "hail-like" graupel, which tends to be larger and denser, immediately falls out of the cloud leading to reduced convection. In contrast, smaller graupel particles stay in the cloud longer which results in more persistent convection. Moreover, field studies indicate that fall speeds of hydrometeors are observed in a broad range of veloc-

ities (Knight and Heymsfield, 1983; Yuter et al., 2006) which implies that there is some uncertainty in the result of the model parameterizations of the fall speeds.

As it is evident from the aforementioned studies, the development of deep convective clouds is sensitive to various parameters. However, these sensitivities are usually examined separately. There are a few studies such as Lee et al. (2008) and Storer et al. (2010) where the effect of several parameters is analyzed, yet the maximum number of considered parameters is three or less. This thesis combines all the parameters mentioned in this chapter, both environmental conditions and microphysics, into a single comprehensive sensitivity analysis. Thereby the relative contributions of each parameter to the uncertainty of the output can be quantified and the parameters causing much uncertainty can be identified. Moreover, the convection in these studies is triggered by a specific trigger mechanism, such as a warm bubble (Dennis and Kumjian, 2017; Storer et al., 2010), a cold pool (Weisman et al., 1997; Adams-Selin et al., 2013) or flow over orography (Chen and Lin, 2005). So far, sensitivities found for a specific trigger mechanism have not been compared. Therefore, the sets of simulations are performed for these three trigger mechanisms independently which allows for a comparison of the results. The large amount of data necessary for these sensitivity analyses is feasible through the application of statistical emulation where surrogate models are used instead of full model simulations, reducing the computational cost.

3. Statistical Emulation

A global sensitivity analysis is performed to identify contributions from both individual parameters and their interactions to the uncertainty of the model output using the numerical weather prediction model COSMO (**CO**nsortium for **S**mall-scale **MO**deling) developed by Deutscher Wetterdienst (see chapter 4). This is possible by variance-based sensitivity analysis (Saltelli, 2008) where the uncertainty of the output is decomposed into the contributions of the model inputs but also of their interactions (see 3.4). To infer those measures the variance-based approach requires a comprehensive sampling of the model output over the whole parameter uncertainty space. The necessary output is often produced by Monte Carlo simulations (Saltelli, 2008). Yet, the COSMO model is a complex numerical weather prediction model with high computational cost such that the generation of the data for the sensitivity analysis is not feasible in a reasonable time using a Monte Carlo approach. Thus, an alternative method is needed: statistical emulation. The idea behind emulation is to build a surrogate model using training data which describes the relationship between a particular model output and a set of uncertain input parameters. Hence, an emulator is able to estimate a specific model output for new input combinations without having to run full model simulations. Because of the low computational cost, the required data for the variance-based sensitivity analysis can easily be produced. To construct emulators for different model outputs over the range of the parameter uncertainty, first a set of uncertain input parameters has to be chosen and their ranges have to be defined. Then well-spaced input combinations are selected from within the parameter uncertainty space. The outputs of the COSMO simulations with these selected parameters are used to train the emulator. They are referred to as *training runs* (Johnson et al., 2015). Once the model output is evaluated, Gaussian process emulation is used to construct the surrogate model for each output of interest independently. Afterwards, the emulators need to be validated (Bastos and O'Hagan, 2009). An overview of the necessary steps for the construction of an emulator is given in Fig. 3.1. Finally, the validated emulators are able to generate output across the whole parameter uncertainty space as needed for the variance-based sensitivity analysis. In the following sections all of these steps are described in more detail.

3.1. Experiment design

As the emulator is required to predict the model output with a certain accuracy, sufficient input information via the training runs is needed. On the one hand, features of the output might get lost and thus cannot be reproduced by the emulator, if there are too few training runs. On the other hand, the emulator
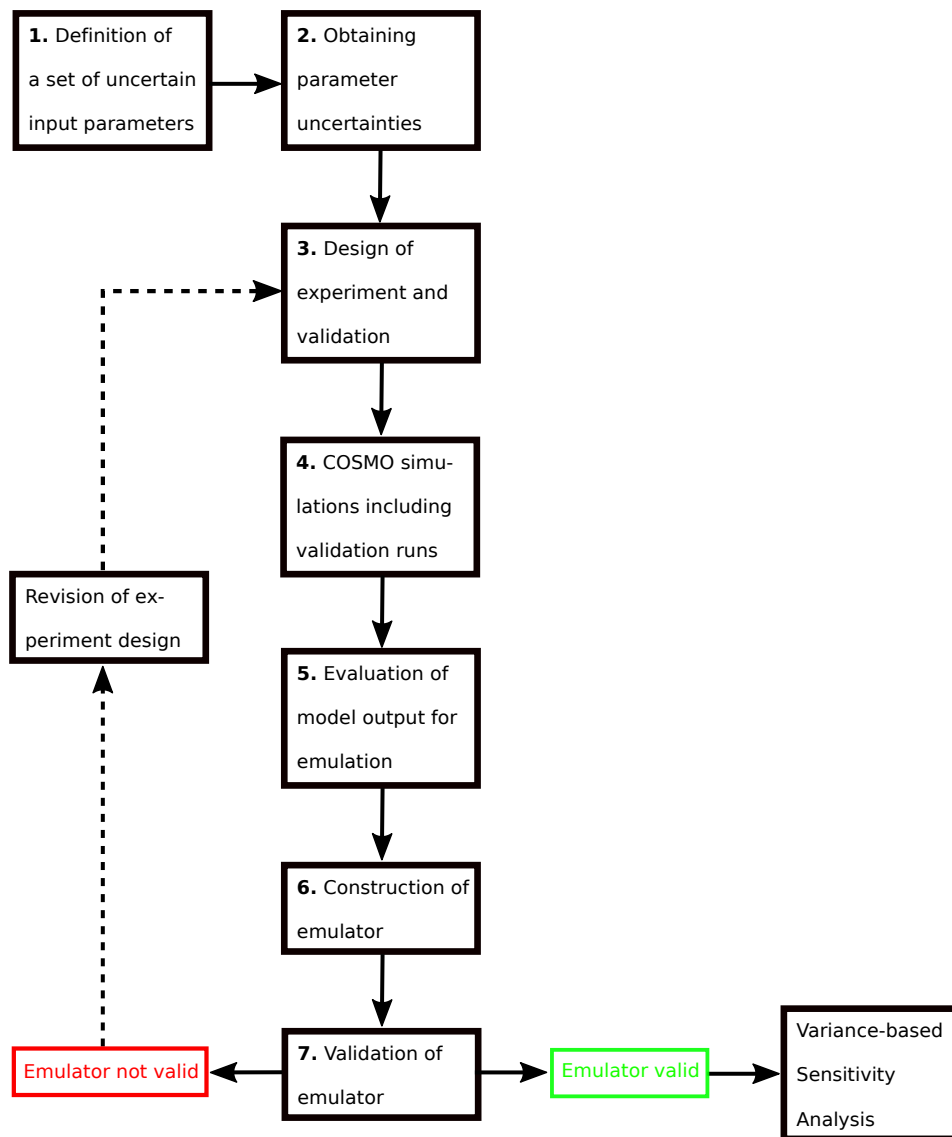
Fig. 3.1.: Schematic overview over the construction of an emulator, after Fig. 1 of Lee et al. (2011).

might reproduce the output almost perfectly but a lot of computational time is needed, if there are too many training runs. Loeppky et al. (2009) suggest a data set of $n = 10d$ training runs to obtain reliable results where d is the number of uncertain input parameters. However, the number can be increased, if the accuracy of the first result is not as high as expected. Here, the number is raised to $n = 15d$ in order to add information while keeping the computational effort feasible. Furthermore, the emulator is required to predict the model output across the whole multi-dimensional parameter uncertainty space. So the training data must have good coverage of this space and be well-spaced. Therefore, the maximin Latin hypercube sampling (Morris and Mitchell, 1995) is applied to place the input combinations for the training runs within the parameter space. This algorithm maximizes the minimum distance between the input combinations and thus ensures an optimal coverage of the parameter uncertainty space.

3.2. Gaussian process emulation

A Gaussian process is a generalization of the Gaussian distribution and the multivariate Gaussian distribution to an infinite number of variables (Rasmussen, 2004). This process is defined by a mean function $m(\mathbf{x})$ and a covariance structure $V(\mathbf{x}, \mathbf{x}')$, where $\mathbf{x} = (x_1, \ldots, x_d)$ and $\mathbf{x}'$ are input combinations within the defined parameter uncertainty. The mean function is specified by

$$m(\mathbf{x}) = \mathbf{h}(\mathbf{x})^T \beta \qquad [3.1]$$

where $\mathbf{h}(\mathbf{x})$ contains known regression functions of $\mathbf{x}$ and β consists of unknown coefficients. The regression functions are arbitrary, however they should be chosen such that they reflect prior beliefs about the form of the emulator (Oakley and O'Hagan, 2004; Johnson et al., 2015). Here, a linear trend is assumed. The covariance structure is given by

$$V(\mathbf{x}, \mathbf{x}') = \sigma^2 c(\mathbf{x}, \mathbf{x}') \qquad [3.2]$$

where σ^2 is an unknown scale parameter and the function $c(\mathbf{x}, \mathbf{x}')$ is a correlation function. The correlation function is designed to decrease as $|\mathbf{x} - \mathbf{x}'|$ increases and furthermore $c(\mathbf{x}, \mathbf{x}) = 1$ has to be valid. Here, the Matérn correlation structure is chosen

$$c_{\text{Matern}}(r) = \frac{2^{1-v}}{\Gamma(v)} \left(\frac{\sqrt{2vr}}{l} \right)^v K_v \left(\frac{\sqrt{2vr}}{l} \right) \qquad [3.3]$$

with positive parameters v and l, Gamma function $\Gamma(v)$ and a modified Bessel function K_v. The Matérn choice leads to a stationary and isotropic covariance function since it only depends on $r = |\mathbf{x} - \mathbf{x}'|$. Thus, it is invariant to rigid motions (Rasmussen and Williams, 2006). This specification of the mean function and the covariance structure induces additional parameters such as v and l. There is no prior information about these so-called *hyperparameters*, hence they are estimated from the training data. This is done by optimizing the marginal likelihood which is the probability of the data given the hyperparameters (Rasmussen, 2004; Rasmussen and Williams, 2006).

To construct the emulator, these prior specifications of the Gaussian process are updated through a Bayesian statistical framework using the information in the training runs to produce a posterior Gaussian process specification that has an updated mean and covariance conditioned on the training data. Known values for the training data and a set of unknown inputs are assumed and both are combined in a joint Gaussian process which is given by (O'Hagan, 2004)

$$\begin{bmatrix} \mathbf{y} \\ \mathbf{y}^* \end{bmatrix} \sim GP \left(\begin{bmatrix} \mathbf{m} \\ m(x) \end{bmatrix}, \begin{bmatrix} \mathbf{C} & \mathbf{c}(x)^T \\ \mathbf{c}(x) & c(x,x) \end{bmatrix} \right) \qquad [3.4]$$

where

$$\mathbf{m} = (m(x_1), m(x_2), \ldots, m(x_n))^T \qquad , \qquad \mathbf{c}(x) = (c(x_1, x), c(x_2, x), \ldots, c(x_n, x))^T \qquad ,$$

$$
\text{and} \qquad \mathbf{C} = \begin{pmatrix} c(x_1,x_1) & c(x_1,x_2) & \dots & c(x_1,x_n) \\ c(x_2,x_1) & c(x_2,x_2) & \dots & c(x_2,x_n) \\ \vdots & \vdots & \ddots & \vdots \\ c(x_n,x_1) & c(x_n,x_2) & \dots & c(x_n,x_n) \end{pmatrix}.
$$

As the training data is known, the goal is to find the conditional distribution of $\mathbf{y}^*$ given $\mathbf{y}$ which is defined by (Rasmussen, 2004):

$$
\mathbf{y}^*|\mathbf{y} \sim GP\left(m(x) + \mathbf{c}(x)^T \mathbf{C}^{-1}(\mathbf{y}-\mathbf{m}), c(x,x') - \mathbf{c}(x')^T \mathbf{C}^{-1}\mathbf{c}(x)\right). \tag{3.5}
$$

From eq. [3.5] it is evident that the posterior mean $m^*(x)$ and the posterior variance $\mathbf{c}^*(x,x)$ are described by

$$
m^*(x) = m(x) + \mathbf{c}(x)^T \mathbf{C}^{-1}(\mathbf{y}-\mathbf{m}) \tag{3.6}
$$

and

$$
c^*(x,x') = c(x,x') - \mathbf{c}(x)^T \mathbf{C}^{-1}\mathbf{c}(x'). \tag{3.7}
$$

Using the assumptions for $m(x)$ and $V(x,x')$ given in eq. [3.1] and eq. [3.2], respectively, and choosing β as $\beta \sim \mathcal{N}(\mathbf{b}, \mathbf{B})$ yields the final result for the posterior mean and covariance in the case of weak prior information ($\mathbf{B}^{-1} = 0$) (O'Hagan, 2004; Johnson et al., 2015):

$$
m^*(x) = \mathbf{h}(x)^T \hat{\beta} + \mathbf{c}(x)^T \mathbf{C}^{-1}\left(\mathbf{y} - \mathbf{H}^T\hat{\beta}\right) \tag{3.8}
$$

$$
\begin{aligned}
V^*(x,x') &= \hat{\sigma}^2 c^*(x,x') \\
&= \hat{\sigma}^2 \left[c(x,x') - \mathbf{c}(x)^T \mathbf{C}^{-1}\mathbf{c}(x') + \left[\mathbf{h}(x) - \mathbf{H}\mathbf{C}^{-1}\mathbf{c}(x)\right]^T \left[\mathbf{H}\mathbf{C}^{-1}\mathbf{H}^T\right]^{-1} \left[\mathbf{h}(x') - \mathbf{H}\mathbf{C}^{-1}\mathbf{c}(x')\right] \right]
\end{aligned}
$$
$$
\tag{3.9}
$$

where

$$
\begin{aligned}
\hat{\beta} &= \left[\mathbf{H}\mathbf{C}^{-1}\mathbf{H}^T\right]^{-1}\mathbf{H}\mathbf{C}^{-1}\mathbf{y}, \\
\mathbf{H} &= (\mathbf{h}(x_1), \mathbf{h}(x_2), \dots, \mathbf{h}(x_n)), \\
\hat{\sigma}^2 &= \frac{\mathbf{y}^T\left(\mathbf{C}^{-1}\mathbf{H}\left(\mathbf{H}^T\mathbf{C}^{-1}\mathbf{H}\right)^{-1}\mathbf{H}^T\mathbf{C}^{-1}\right)\mathbf{y}}{n-q-2}.
\end{aligned}
\tag{3.10}
$$

A detailed derivation and additional information regarding statistical emulation can be found in O'Hagan (2004); Oakley and O'Hagan (2004); O'Hagan (2006); Lee et al. (2011); Johnson et al. (2015).

In the following a schematic overview of the steps described above is given. In this example, there are two uncertain input parameters: the CCN concentration and the wind shear (represented by the factor F_{shear}). Thus, the input parameter uncertainty space is two-dimensional. Via the Latin hypercube sampling the input combinations of the training data are well-spaced within the uncertainty space to guarantee for good coverage (Fig. 3.2).
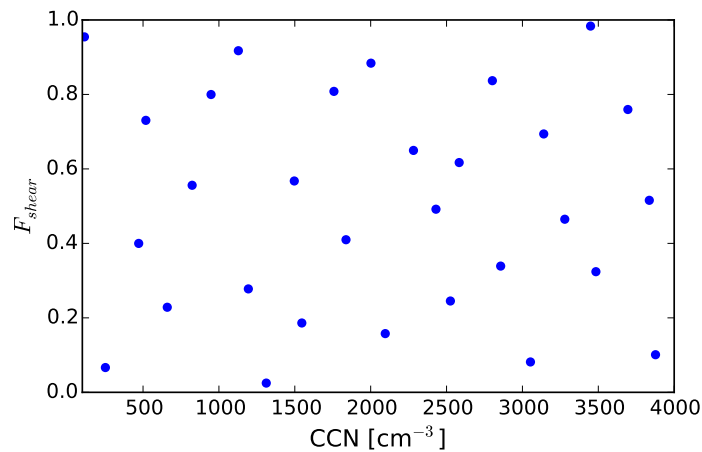
Fig. 3.2.: Experiment design for a toy emulator with two uncertain input parameters. The input combinations for the training runs are depicted by blue dots. The points are placed within the uncertainty space using the Latin hypercube sampling.
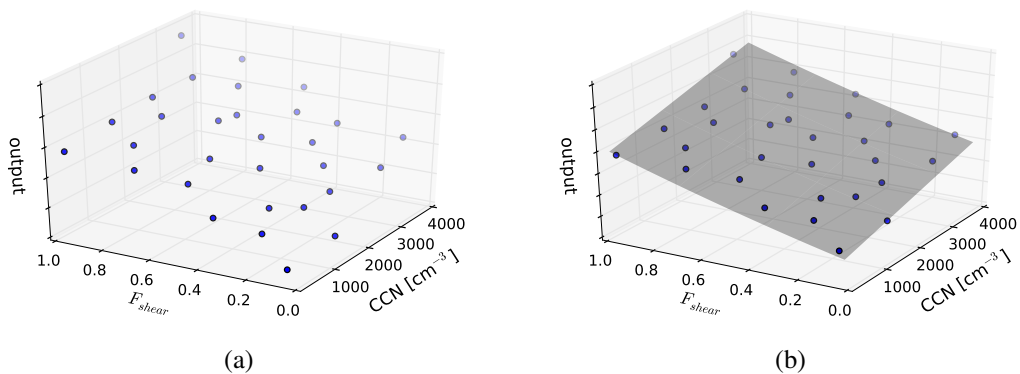
Fig. 3.3.: (a) Corresponding output values (z-axis) for the training runs spanning the input uncertainty space (xy-plane). (b) Same as (a) with an additional surface to represent the emulator fit.

The numerical weather prediction model is run for all of the input combinations marked in Fig. 3.2. Then, an output of interest is evaluated for each training run such that the output values corresponding to the input combinations can be displayed on the z-axis (Fig. 3.3a). Once the training data and their corresponding outputs are available, the emulator is fitted using Gaussian processes. Figuratively speaking, this means that a surface is fitted to the points (Fig. 3.3b). This surface is subsequently used to predict output values at new input combinations that are not part of the training data.

In this work the Gaussian process emulation is performed using the statistical software R (R Core Team, 2017) and the R package 'DiceKriging ' (Roustant et al., 2012).

3.3. Validation

Once an emulator is built, it is necessary to determine whether it produces an accurate estimation of the model for input combinations that where not originally included in the training data. Bastos and O'Hagan (2009) present a wide range of diagnostics to validate Gaussian process emulators of which some are described in the following paragraphs.

At first, the consistency of the emulator is examined by an internal leave-one-out validation. For this purpose, the prediction of the output for each point of the training data is computed when this specific point is removed from the training data and not used for the emulator fit. The emerging residuals between the model output and the prediction follow a standard Student-t distribution (Bastos and O'Hagan, 2009) and thus a quantile-quantile plot is a useful figure. In this plot the theoretical quantiles of the Student-t distribution are plotted against the quantiles of the distribution of the residuals. If the hypothesis is true and both distributions are in good agreement, the points in the quantile-quantile plot lie close to the 45 degree line (line of equality). Points following a line with different slope indicate an over- or underestimation of the variability. An example is given in Fig. 3.4.
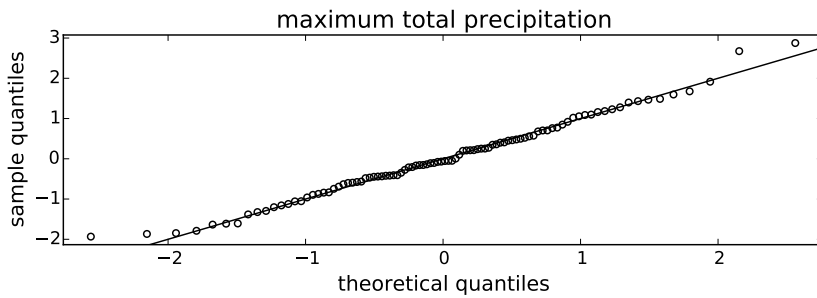
Fig. 3.4.: Quantile-quantile plot for the emulator of the maximum total precipitation.

The other measures make use of the comparison between model output and the prediction of the emulator for new input combinations which are not included in the training data. Therefore, 45 additional model runs are performed whose input combinations are generated by the maximin Latin hypercube algorithm to cover the parameter space (*validation data*). The same input combinations are fed into the emulator to obtain the predictions. The individual prediction error E_k^i for the output k is given by

$$E_k^i = \frac{y_k - \eta(x_k)}{\sigma(\eta(x_k))} \qquad [3.11]$$

where y_k is the model output, $\eta(x_k)$ the prediction of the emulator and $\sigma(\eta(x_k))$ the standard deviation of the prediction. Accordingly, large values of E_k^i imply disagreement between the model and the emulator. The individual prediction error can be plotted against different parameters such as the index of the simulation, the model output or the input parameters in order to analyze possible systematic errors which can be seen in Fig. 3.5. An interpretation of noticeable patterns, where a large number of points is not

within the thresholds denoted by the dashed lines, is described in Bastos and O'Hagan (2009). However, these patterns are not found in this study.
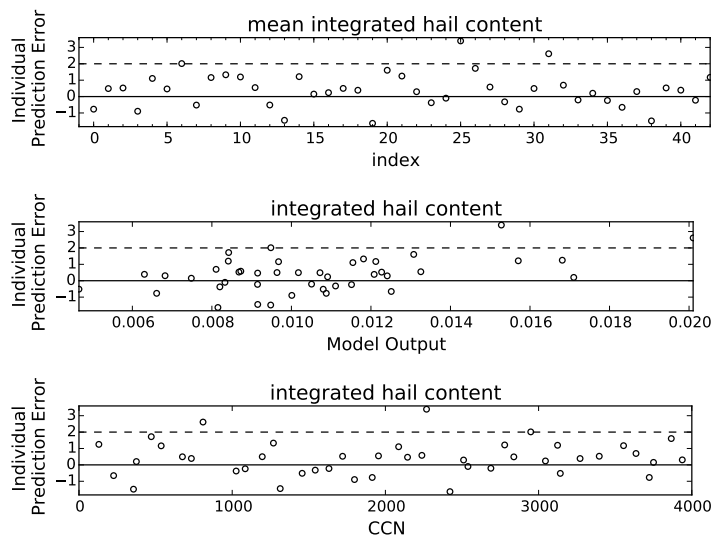
Fig. 3.5.: Individual prediction errors for the integrated hail content plotted against the simulation index, the model output and an input parameter (CCN concentration). The dashed lines denote the threshold given in Bastos and O'Hagan (2009).

Furthermore, not only the individual prediction error but also the actual prediction can be plotted against the model output. As both quantities are supposed to be almost equal, the points should follow the 45 degree line if the emulator is a reasonable representation of the model. Moreover, the 95% confidence bounds on the emulator prediction can be obtained from the Gaussian process posterior specification of the emulator. An emulator is considered valid, if the 95% confidence bound on the emulator prediction crosses the line of equality for at least 95% of the validation points. Fig. 3.6 shows this validation plot for the maximum amount of hail at the ground.

As it can be seen, not all points of the validation data capture the model result within their confidence bounds. However, those points are still close to the 45 degree line and their confidence bounds are reasonably sized. Thus, this emulator could still be considered valid although more than 5% of the validation points are outliers.

Finally, the robustness of the emulators is evaluated in order to rule out potential dependencies of the result on the choice of the training data. Therefore, a random sample of 45 new validation runs is generated from the training data and the original validation data is assigned to the training data. Although the new training data does not guarantee for a well-spaced coverage of the parameter space as two different Latin hypercube samplings are mixed, it is still used to build another emulator and a certain error is taken into account. This is done for a total sum of ten random samples which leads to a set of independent emulators describing the same conditions. The results of these emulators and the original
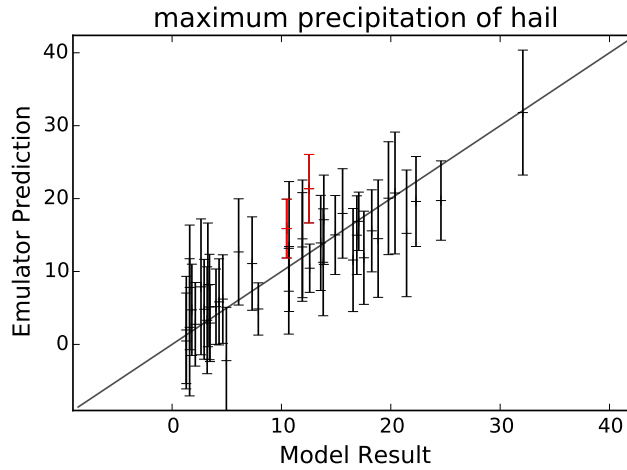
Fig. 3.6.: Emulator prediction of the maximum precipitation of hail with 95% confidence interval plotted versus the model output. Outliers are depicted in red.

one are compared and the deviations are evaluated. If they are in a reasonable range, the emulator is robust to changes in the training data.

3.4. Variance-based sensitivity analysis

When running a model or emulator with different combinations of d different input parameters, it is common to induce an uncertainty in the output's value which can be quantified as variance. The goal of the variance-based sensitivity analysis is to decompose this output variance into different contribution sources related to the input parameters that were varied. The decomposition of the variance includes not only contributions from each parameter individually, but also contributions from interactions between two or more input parameters. Thus, assuming independence between the input parameters, the decomposition can be written as (Oakley and O'Hagan, 2004)

$$V = \sum_i V_i + \sum_{i<j} V_{ij} + \ldots + V_{1\ldots p} \qquad [3.12]$$

where V_i are contributions from each parameter. Terms with more than one index indicate contributions from parameter interactions where the number of indices corresponds with the number of interacting parameters. V_{ij} are contributions of two interacting parameters, while $V_{1\ldots p}$ describes the contribution from all considered parameters interacting with each other. Here, the extended Fourier amplitude sensitivity test (FAST) introduced by Saltelli et al. (1999) is used to generate this variance decomposition. The concept of FAST is a transformation to 1D Fourier space such that the d-dimensional input space can be explored by a monodimensional curve specified by s. This has the advantage that along the path all input parameters x_i change simultaneously which means that FAST offers a global sensitivity analysis. In contrast, local sensitivity analysis considers the variation of one parameter only while the remaining ones are kept constant (OAT approach). In order to gain a space-filling curve and to avoid possible

overlap with upper frequencies, a sample size of several thousand runs is desirable (Saltelli et al., 1999). As this amount of simulations is not feasible with the conservative approach of running the full numerical weather prediction model, the emulators are necessary to simulate the required model output. The transformation to the 1D Fourier space is defined by

$$x_i = \frac{1}{2} + \frac{1}{\pi} \arcsin\left(\sin\left(\omega_i s\right)\right) \qquad [3.13]$$

where $s \in (-\pi; \pi)$. The frequencies ω_i depend on the sampling size and are taken from Saltelli (2008). After the transformation the output y is given by

$$y = f(s) \qquad [3.14]$$

where f is the model or rather the emulator in this case. According to Weyl's theorem (Weyl, 1938) the variance V can be computed by the first and second moment of y:

$$V = \bar{y}^{(2)} - \left(\bar{y}^{(1)}\right)^2 = \frac{1}{2\pi} \int\limits_{-\pi}^{\pi} f^2(s)ds - \left(\frac{1}{2\pi} \int\limits_{-\pi}^{\pi} f(s)ds\right)^2 \qquad [3.15]$$

where the probability density functions are omitted without the loss of generality. Now the model f can be rewritten as a Fourier series

$$y = f(s) = \sum_{j=-\infty}^{\infty} A_j \cos(js) + B_j \sin(js) \qquad [3.16]$$

with the coefficients $A_j = \frac{1}{2\pi} \int_{-\pi}^{\pi} f(s)\cos(js)ds$ and $B_j = \frac{1}{2\pi} \int_{-\pi}^{\pi} f(s)\sin(js)ds$. Inserting eq. [3.16] in eq. [3.15] the output variance can be approximated by

$$\begin{aligned} V &\approx \sum_{j=-\infty}^{\infty} \left(A_j^2 + B_j^2\right) - \left(A_0^2 + B_0^2\right) \\ &\approx 2\sum_{j=1}^{\infty} \left(A_j^2 + B_j^2\right). \end{aligned} \qquad [3.17]$$

In order to get the amount of output variance V_i caused by input i, the sum is not taken over all possible frequencies j, instead just ω_i and its harmonics $p\omega_i$, $p \in \mathbb{N}$, are considered. As the amplitude decreases for higher harmonics, only contributions up to the fourth order are taken into account. Thus, the variance of the output due to the uncertainty of input i reads

$$V_i = 2\sum_{p=1}^{4} \left(A_{p\omega_i}^2 + B_{p\omega_i}^2\right). \qquad [3.18]$$

The so-called *main effect* S_i of each input parameter is obtained by normalizing eq. [3.18] with the overall variance in the output

$$S_i = \frac{V_i}{V} \qquad [3.19]$$

which is a measure of the contribution of input i to the output variance. Hence, the main effect shows the percentage by which the output variance could be decreased if there was no uncertainty in the input

i. Furthermore, the *total effect* S_{T_i} generated by this method includes all terms that are linked to input *i*, i.e. both individual contribution and interaction terms. Similarly to eq. [3.18] the variance $V_{\sim i}$ caused by all input parameters except *i* is computed by summing over all frequencies and their harmonics except for ω_i. Consequently, the total effect is given by

$$S_{T_i} = 1 - \frac{V_{\sim i}}{V} \quad . \tag{3.20}$$

As the total effect includes both individual and interaction contributions and the individual contributions are accessible through the main effect, the *interaction effect* S_{I_i} can be determined by

$$S_{I_i} = S_{T_i} - S_i \tag{3.21}$$

giving an indication of how much the input parameter *i* interacts with other parameters.

Fig. 3.7 shows a bar plot, which is used for graphical presentations of the above mentioned measures, for an exemplary output. The individual contributions S_i from the input parameters to the output uncer-
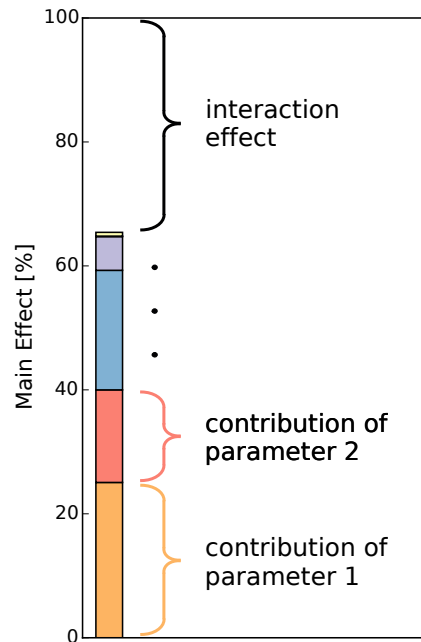
Fig. 3.7.: Bar plot of an exemplary result of the sensitivity analysis. Main effects S_i are depicted by colored bars. The blank space above the bar represents the sum of all interaction effects S_{I_i}.

tainty are depicted by the colored parts of the bar. Thus, the height of the bar shows the percentage of the uncertainty that can be explained by the main effects S_i. Consequently, the space above the bar to fill 100% represents interaction effects S_{I_i}.

In this work the sensitivity measures of the FAST approach are computed using the statistical software R (R Core Team, 2017) and the R package 'sensitivity' (Pujol et al., 2017).

4. COSMO Model and Model Setup

For this study the limited-area numerical weather prediction model COSMO (Consortium for Small-Scale Modeling) (Baldauf et al., 2011; Schättler et al., 2016) developed by Deutscher Wetterdienst (DWD) and the COSMO consortium is used. The model is based on primitive hydro-thermodynamical equations describing the conservation of momentum, mass and heat that are solved for a compressible non-hydrostatic flow in a moist atmosphere. These equations are formulated on a rotated geographical grid to avoid numerical singularities near the poles (Doms and Baldauf, 2015). The model domain is discretized on an Arakawa C-grid and the time integration is executed by a two time-level Runge-Kutta scheme (Wicker and Skamarock, 2002). Several setups of the COSMO model have been run operationally by DWD. The domain of COSMO-EU covers Europe with a horizontal resolution of 7 km while COSMO-DE focuses on Central Europe and Germany with an increased resolution of 2.8 km. However, since December 2016 COSMO-EU is replaced by the new model ICON-EU and since May 2018 COSMO-DE is replaced by COSMO-D2. In the operational setup a single-moment microphysics scheme is employed and, depending on the resolution, subgrid-scale processes such as convection or turbulence are parameterized.

For the simulations in this study, COSMO is run in an idealized setup with 700 x 500 grid points where the horizontal resolution is 1 km. Consequently convection is explicitly resolved. The domain extends to a height of 23 km which is resolved by 64 vertical levels. These layers follow the transformation given in Gal-Chen and Somerville (1975) such that they are denser near the ground and further apart with increasing height. Open boundary conditions are used to prevent the simulated hailstorm from influencing itself. Moreover, the radiation scheme is switched off and the Coriolis force is neglected in the simulations. The initial temperature and humidity profiles are taken from Weisman and Klemp (1982), hereinafter referred to as WK, to maintain atmospheric conditions that favor the development of deep convection. The temperature profile is given by eq. [4.7]. The maximum specific humidity q_{v0} according to WK is set to a value of 12 g kg^{-1} at the lowest level. The vertical profile of the wind speed is chosen similar to Fig. 3b of Weisman and Rotunno (2000), where they present a hodograph for quarter-circle shear. Furthermore, the two-moment mixed-phase bulk microphysics scheme by Seifert and Beheng (Seifert and Beheng, 2006a) is implemented in the idealized setup, which predicts both the mass mixing ratios and the number densities of six hydrometeors, namely cloud droplets, rain, cloud ice, snow, graupel and hail. Moreover, Igel et al. (2015) state that single moment schemes may cause large errors in the representation of clouds and thus they strongly recommend to use multi-moment microphysics schemes. In this study, the results are compared for three different trigger mechanisms

which initiate deep convection: a warm bubble, a cold pool and a bell-shaped mountain ridge. Cross-sections of these trigger mechanisms are shown in Fig. 4.1.

(a) warm bubble   (b) cold pool   (c) orography
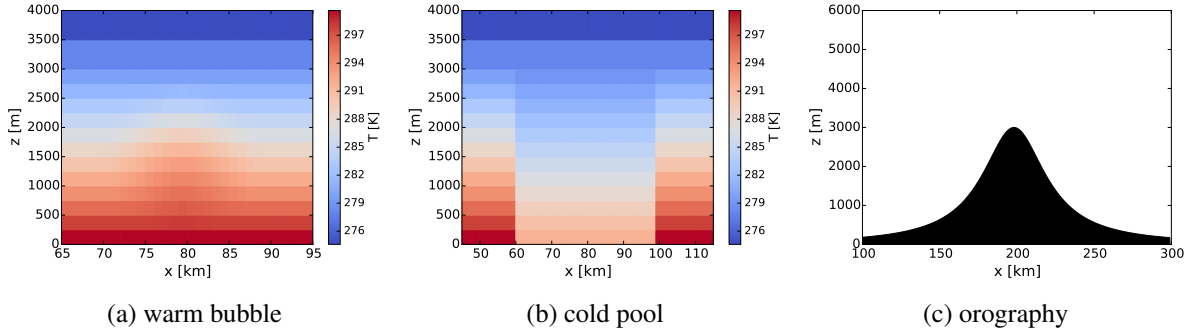
Fig. 4.1.: Triggers of deep convection used in this study. **(a)** Ellipsoidal warm bubble with a temperature perturbation of $\Delta T = 2$ K and a horizontal radius of $R_{hor} = 10$ km. **(b)** Cylindrical cold pool with a temperature perturbation of $\Delta T = -8$ K and a radius of $R_{hor} = 20$ km. **(c)** Bell-shaped mountain ridge with a height of 3000 m and a half-width of 25 km.

First, the frequently used approach of a warm bubble (WB) is employed (4.1a). As in WK the maximum temperature excess ΔT lies between 2 K and 5 K and is located in the center of the bubble. The perturbation decreases towards the edges following a $\cos^2$ function. The vertical extent of the warm bubble is fixed at $R_z = 1400$ m whereas the horizontal radius is varied between $R_{hor} = 5$ km and $R_{hor} = 15$ km. At model initialization the bubble is released at a distance of $\Delta x = 80$ km from the model boundary to the west and at a distance of $\Delta y = 200$ km from the boundary to the south where it ascends and triggers convection. Second, a cold pool (CP) is employed as trigger mechanism (4.1b). It is a negative temperature perturbation (-10 K $\leq \Delta T \leq -6$ K) in the shape of a cylinder which is placed on the ground and reaches a height of $z = 3000$ m. The strongest temperature contrast is found at the bottom of the cylinder and the difference in temperature to the ambient air decreases linearly with increasing height. Within the cold pool the conditions are horizontally homogeneous. The simulations are initialized with the cold pool located at the same position as the warm bubble. The third trigger mechanism is a straight bell-shaped mountain ridge (Oro) which extents from the northern to the southern boundary of the domain (4.1c). Its height and halfwidth range from 2000 m to 5000 m and 5 km to 50 km, respectively. The center of the ridge is situated at a distance of $\Delta x = 200$ km from the boundary to the west and a distance of $\Delta y = 200$ km from the boundary to the south. As the directional wind shear in the lower atmosphere is altered during the simulations, the angle between the axis of the crest and a north-to-south axis is coupled to the directional shear in order to guarantee a roughly perpendicular flow over the mountain ridge. In contrast to the thermal triggers, the ridge constantly produces small clouds right above the crest, which reduce the comparability to the warm bubble and the cold pool setup. Therefore, a larger domain of 1200 km x 500 km is used to give room to the orography. For the analysis the western part of the domain containing the mountains is removed and only an area of 700 km x 500 km located in the east is considered. The time step of the simulation is set to $\Delta t = 6$ s. All simulations run for six

hours except for the orography case where a five hour spin up is required to allow for more persistent convective development. Thus, the warm bubble and cold pool simulations are evaluated from 0 h to 6 h and the orography simulations from 5 h to 11 h.

4.1. Structure of the simulated storms

A short overview of the typical development and the structure of the simulated clouds is given in this section using the warm bubble as trigger mechanism. In this example, the CCN concentration is 1972 cm^{-3} and the wind shear factor is 0.5370 such that intermediate pollution and wind shear are represented. Furthermore, the factor for the ice nuclei concentration is chosen to be 0.0322 and the potential temperature θ_0 of the Weisman-Klemp vertical profile amounts to 295.66 K. The warm bubble is characterized by a horizontal radius of 10.668 km and a temperature perturbation of 2.78 K. Detailed descriptions of these parameters are given in the section 4.3.1. Horizontal and vertical cross-sections of the simulated cloud are found in Fig. 4.2.
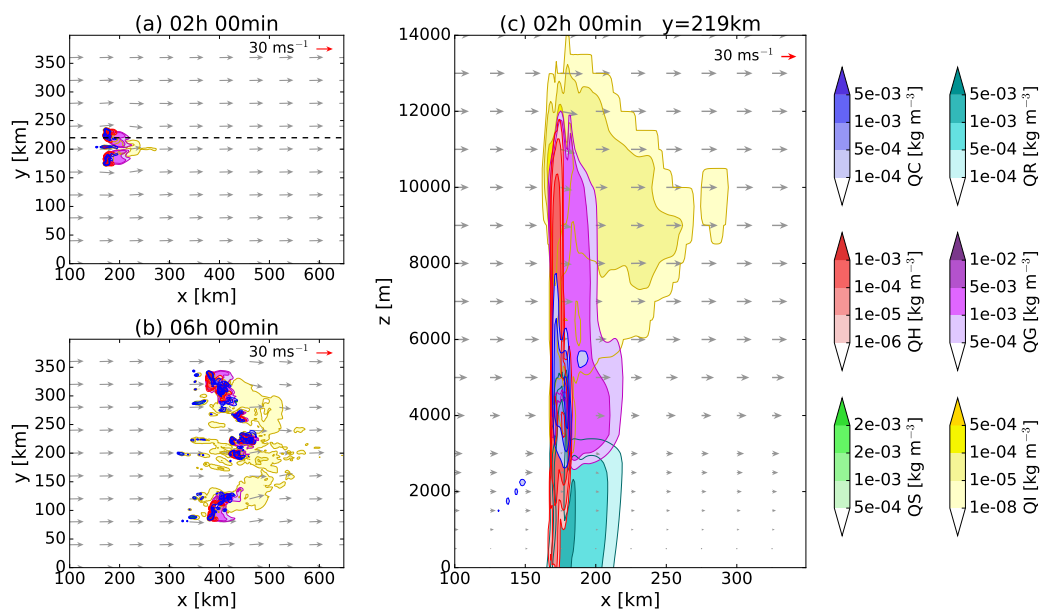
Fig. 4.2.: Cross-sections of the cloud at different time steps.
(a) & (b) Horizontal cross-section at a height of z=5000 m for (a) 2 h and (b) 6 h after the start of the simulation. (c) Vertical cross-section at y=219 km for 2 h after the start of the simulation. The colors denote the different hydrometeors (QC: cloud water, QR: rain, QH: hail, QG: graupel, QS: snow, QI: ice) and the dashed line in (a) denotes the location of the vertical cross-section of (c). The arrows illustrate the wind field. The colors represent the six hydrometeor classes cloud water (dark blue), rain (light blue), hail (red), graupel (purple), snow (green) and ice (yellow).

The warm bubble initiates a single cell which develops further. After two hours the storm has split into two cells (Fig. 4.2a). The updraft regions contain graupel, hail and cloud water; graupel is also present in

larger areas outside of the updrafts. After six hours, the convective cells have moved to the East, but have developed into a curved structure extending in the y-direction (Fig. 4.2b). The vertical cross-section depicting the structure of the storm after two hours (Fig. 4.2c) shows that graupel and hail appear in all heights of the cloud, whereas ice is found in the anvil near the tropopause and cloud water is found mainly between $z = 2000$ m and $z = 6000$ m. Rain, graupel and hail reach the ground as precipitation.

The spatial distribution of the accumulated precipitation of hail is presented in Fig. 4.3 where the black cross marks the center of the initial warm bubble.
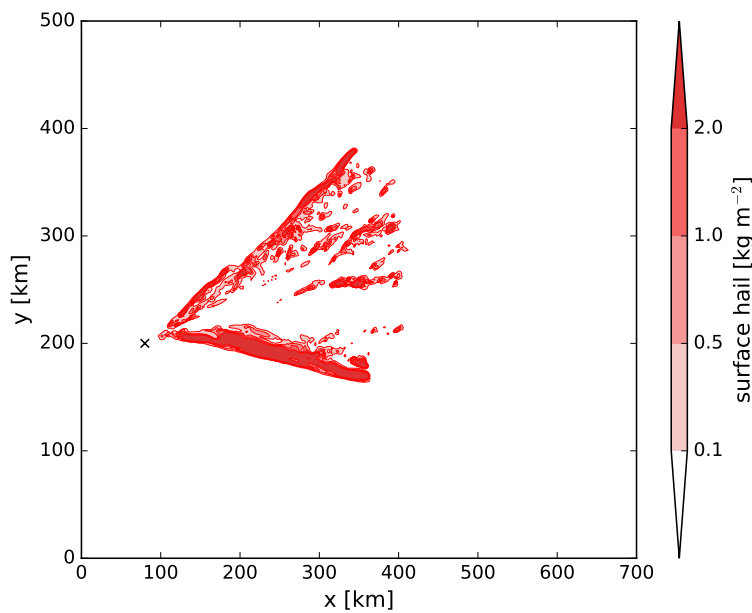
Fig. 4.3.: Accumulated amount of hail at the surface after six hours of simulation. The black cross denotes the location of the initial warm bubble that is used as convection trigger.

The separation into two cells is clearly visible as two lines of intense precipitation are seen in the plot. The right cell moves about 300 km to the East and 50 km to the South. Following its track, the amount of hail at the ground is constantly more than 2 kg m^{-2}. The left cell also travels about 300 km to the East. But because it is moving along the y-component of the prescribed wind field, its track covers a distance of 200 km to the North. In contrast to the right cell, the intensity of the precipitation of hail varies along the track such that precipitation with more than 2 kg of hail per square meter is confined to small areas. Thus, the right cell develops more intensely and produces more precipitation as described in previous studies (Rotunno and Klemp, 1985; Bluestein, 2013; Davies-Jones, 2015). Moreover, there are smaller areas where hail is observed at the ground between the two main cells once the storm has developed a structure similar to a squall line.

After six hours of simulation, the deep convective cloud still develops and produces precipitation such that a full life cycle of a hailstorm cannot be modeled in that time period. Presumably this is caused by the choice of open boundary conditions which supply an infinite amount of energy and thus prevent the storm from an excessive decay.

4.2. Output variables

Many aspects are of interest when analyzing the sensitivities of clouds and hail formation to different conditions. We focus on cloud variables, precipitation, diabatic heating rates and the size distribution of hail. As an emulator is only able to relate a single output value to a set of input parameters either countless emulators are necessary to represent the temporal evolution of three-dimensional fields or the output information has to be condensed, e.g. to mean or maximum values, to reduce the number of emulators, which is done here.

The cloud variables are given by the vertically integrated specific content of each particle class (cloud water, graupel, hail, ice, rain, snow). They are directly connected to the cloud itself as they describe its composition and also its volume. The spatial and temporal mean is taken over the whole domain and all time steps which results in a single value for each particle class for every simulation.

As the forecast of precipitation is important for most people, we also analyze the simulated precipitation. Here, we look at the sum of precipitation by hail, the precipitation rate of hail, the sum of total precipitation and the total precipitation rate. The maximum values of these output variables are used for the emulator studies except for the precipitation of hail where both the mean and the maximum value are evaluated.

Moreover, the size distribution of hailstones reaching the ground is of interest regarding the damage potential of hail events. Especially large hailstones may cause injuries when hitting persons and thus an accurate forecast of the size distribution is important. In the two-moment scheme of Seifert and Beheng (2006a) a generalized Γ-distribution is implemented for the size distributions of hydrometeors:

$$\frac{dN}{dx} = A x^{\nu} \exp\left(-\lambda x^{\mu}\right) \qquad [4.1]$$

where N is the number density, x is the particle mass and ν and μ are parameters of the Γ-distribution. The coefficients A and λ are given by gamma distributions and the number and mass density, respectively (Seifert and Beheng, 2006a). Via a conversion from mass x to particle diameter D the term $\frac{dN}{dx}$ can be transformed to $\frac{dN}{dD}$ and thus a measure for the number of particles per diameter is available. Emulators are constructed for the number density at twelve fixed diameters for the temporal and spatial mean of the size distribution of hail at the ground. In addition, there are emulators for the maximum number density and the corresponding diameter for two, four and six hours after the initialization of the simulation to also track parts of the temporal evolution.

Deep convective clouds usually cover a large area and thus are able to influence to surrounding atmosphere. Furthermore, diabatic processes cause a redistribution of energy such as heating due to conden-

sation and freezing or cooling due to evaporation and melting. So to examine the impact of the simulated storm on the ambient conditions, we interpret the vertical profiles of the diabatic heating rates. Joos and Wernli (2011) separate the temperature changes into contributions from phase transitions between the different hydrometeors such that it can be described as

$$\frac{\partial T}{\partial t} = \frac{L_v}{c_p}(S_c + S_r) + \frac{L_s}{c_p}(S_i + S_g + S_h + S_s) \qquad [4.2]$$

where L_v and L_s are the latent heat of vaporization and sublimation and c_p is the specific heat capacity of dry air for isobaric processes. The terms S_x specify the conversion processes producing cloud water (c), rain (r), ice (i), graupel (g), hail (h) or snow (s) that include phase transitions and therefore either supply energy or subtract energy from the surrounding air. Thus, the heating rate $\frac{\partial T}{\partial t}\big|_x$ related to each hydrometeor class x is defined as

$$\left.\frac{\partial T}{\partial t}\right|_x = \frac{L_{v/s}}{c_p} \cdot S_x \qquad [4.3]$$

where L_v is chosen for transitions between vapor and liquid, L_s for transitions between vapor and ice and $L_s - L_v$ for transitions between liquid and ice. The spatial mean of the heating rates is calculated for each particle class in each layer such that vertical profiles of the heating rates are available. The temporal means of these profiles are predicted by the emulators.

For a more detailed analysis the processes summarized by S_x are considered separately. Tab. 4.1 gives an overview of the conversions included in each S_x that are part of the microphysics scheme of the COSMO model. The corresponding parameterizations are described in Seifert and Beheng (2006a).

The emulators are built to predict the temporal evolution of the spatial mean of these conversion rates.

4.3. Setup for different environmental conditions

4.3.1. Uncertain input parameters

A set of six input parameters is defined describing different regimes of atmospheric conditions. This set consists of the CCN concentration, the concentration of ice nuclei (IN), the directional wind shear and the surface potential temperature θ_0 determining the WK temperature profile. Furthermore, the temperature perturbation and the radius of the warm bubble and the cold pool are perturbed, whereas in the orography case the height and the halfwidth of the mountain ridge are perturbed. An overview over the chosen input parameters and their ranges is given in Tab. 4.2, along with a detailed description of each parameter in the following sections.

Concentration of cloud condensation nuclei

The number of CCN plays an essential role in the formation of cloud droplets where water vapor molecules settle onto the surface of the aerosols until the whole surface is covered. A certain amount of supersaturation is necessary to reach a critical radius where no further supersaturation is necessary to

Tab. 4.1.: Overview of the considered phase transitions used to calculate the diabatic heating rates.

S_x	conversion
S_c	• saturation adjustment (condensation) • droplet nucleation • melting of ice
S_r	• evaporation • melting processes ($S^{r+i=r}$, $S^{r+s=r}$, S^g_{melt}, S^h_{melt}, S^s_{melt})
S_i	• ice nucleation and deposition • riming and freezing processes ($S^{c+i=i}$, $S^{r+i=i}$, S^c_{freeze}, $S^{r \to i}_{freeze}$)
S_g	• evaporation • deposition • riming and freezing processes ($S^{c+g=g}$, $S^{r+g=g}$, $S^{c+i=g}$, $S^{r+i=g}$, $S^{c+s=g}$, $S^{r+s=g}$, $S^{r \to g}_{freeze}$)
S_h	• evaporation • deposition • riming and freezing processes ($S^{c+h=h}$, $S^{r+h=h}$, $S^{r \to h}_{freeze}$)
S_s	• evaporation • deposition • riming processes ($S^{c+s=s}$, $S^{r+s=s}$)

Tab. 4.2.: Overview over the uncertain input parameters and their ranges.

input	min	max	units
CCN concentration	100	4000	cm^{-3}
IN concentration	0.01	10	factor
wind shear (F_{shear})	0	1	factor
potential temperature at the ground θ_0 (WK profile)	295	302	K
temperature perturbation ΔT (WB)	2	5	K
temperature perturbation ΔT (CP)	-10	-6	K
height of ridge (Oro)	2000	5000	m
radius of warm bubble R_{hor}	5	15	km
radius of cold pool R_{hor}	10	30	
halfwidth of ridge (Oro)	5	50	

grow to cloud droplets. Depending on the size and the chemical composition of the aerosols, the supersaturation required for the activation can be reduced (Houze, 1993; Dusek et al., 2006). Thus, from the early stage of cumulus cloud formation to the dissipation, the CCN concentration influences the development and dynamics as well as the microphysics (Cui et al., 2006; Seifert and Beheng, 2006b; Rosenfeld et al., 2008; Noppel et al., 2010; Khain et al., 2011; Cui et al., 2011; Morrison, 2012; Tao et al., 2012; Fan et al., 2013). A cloud droplet activation scheme based on grid-scale supersaturation and empirical power law activation spectra is implemented in COSMO using look-up tables introduced by Segal and Khain (2006). Furthermore, the aerosol is assumed to have the largest concentration in the lowest 2 km above the ground, followed by an exponential decrease towards higher altitudes with a scale height of 1 km. In this study, the maximum CCN concentration is varied between $100\,\mathrm{cm}^{-3}$ and $4000\,\mathrm{cm}^{-3}$, which corresponds to a change from maritime to polluted conditions.

Concentration of ice nuclei

Similar to CCN, the IN are particles that support the formation of cloud ice (Houze, 1993) and therefore primarily affect the number of ice particles in the cloud. Here, a scaling factor f_{IN} is applied to three microphysical processes: the deposition nucleation of cloud ice, where ice is formed on an IN directly from the vapor phase, the immersion freezing of cloud droplets and the immersion freezing of rain drops, where supercooled drops freeze that contain a nucleus enhancing ice nucleation (Houze, 1993; de Boer et al., 2010). In case of the formation of cloud ice, the heterogeneous nucleation scheme of ice from Huffman and Vali (1973) is used in the simulations. After the number of ice particles N_{IN} is calculated according to their formula, it is multiplied by f_{IN} which represents variations of the IN concentration. For the freezing of cloud droplets and raindrops, a stochastical model is implemented in the two-moment scheme (Seifert and Beheng, 2006a) following the measurements of Bigg (1953). The values for the parameters are taken from Pruppacher and Klett (1997). The rates of heterogeneous freezing of cloud droplets and rain drops are given by (Seifert and Beheng, 2006a)

$$\left.\frac{\partial N}{\partial t}\right|_{het} = -L \cdot J_{het}(T) \qquad [4.4]$$

where N is the number density and L the mass density of either cloud droplets or rain drops. J_{het} describes the temperature function for heterogeneous freezing. To simulate variations of the IN concentration for the freezing of cloud droplets and raindrops, J_{het} is multiplied by f_{IN} leading to

$$\left.\frac{\partial N}{\partial t}\right|_{het} = -L \cdot J_{het}(T) \cdot f_{IN} \ . \qquad [4.5]$$

In this study, f_{IN} is varied from 0.01 to 10 on a logarithmic scale. This range is chosen according to DeMott et al. (2010) to represent measurements of different field campaigns. For all three processes the same value of the scaling factor is used.

Wind shear

In general, wind shear describes the difference in wind velocity and wind direction between two heights and thus characterizes the wind field of the environment in an embedded layer. Here, the focus is on directional shear as this is most important for the organization of convection (Davies-Jones, 2015). The vertical profile of velocity is not varied between the simulations. A factor F_{shear} is introduced which determines the vertical profile of the wind direction WD according to

$$WD(z) = \begin{cases} 270° - F_{shear} \cdot 90° + \frac{F_{shear} \cdot 90°}{6000\,\text{m}} \cdot z & , z \leq 6000\,\text{m} \\ 270° & , z > 6000\,\text{m} \end{cases} \qquad [4.6]$$

where $F_{shear} \in [0;1]$. For example, $F_{shear} = 0$ represents westerly wind at all heights and the maximum value of $F_{shear} = 1$ indicates southerly wind near the ground, which gradually turns into a westerly wind with increasing height. A graphical presentation of eq. [4.6] for different values of F_{shear} is given in Fig. 4.4.
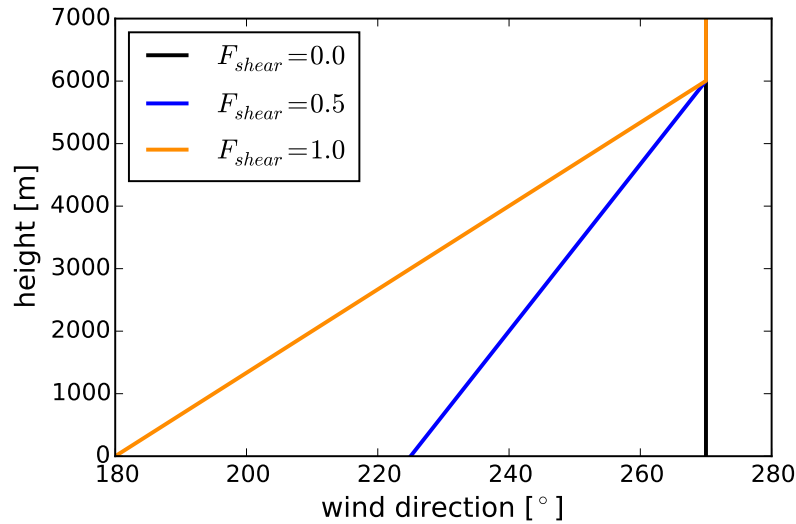
Fig. 4.4.: Wind direction as a function of height for three different wind factors.

Potential temperature θ_0

The WK vertical profile of the potential temperature provides atmospheric conditions favoring deep convection and is calculated as

$$\theta(z) = \begin{cases} \theta_0 + (\theta_{tr} - \theta_0)\left(\frac{z}{z_{tr}}\right)^{\frac{5}{4}} & , z \leq z_{tr} \\ \theta_{tr} \cdot \exp\left[\frac{g}{c_p T_{tr}}(z - z_{tr})\right] & , z > z_{tr} \end{cases} \qquad [4.7]$$

with the potential temperature at the tropopause $\theta_{tr} = 343\,\text{K}$, the height of the tropopause $z_{tr} = 12\,\text{km}$, the gravity acceleration $g = 9.80665\,\text{m s}^{-2}$, the specific heat of dry air $c_p = 1005\,\text{J kg}^{-1}\,\text{K}^{-1}$ and the

temperature at the tropopause $T_{tr} = 213\,\mathrm{K}$. The near-surface potential temperature θ_0 is initially set to $300\,\mathrm{K}$ (Weisman and Klemp, 1982), but in this study θ_0 is varied between $295\,\mathrm{K}$ and $302\,\mathrm{K}$ in order to simulate different atmospheric conditions. Skew-T log-p diagrams of temperature and dew point profiles are shown in Fig. 4.5 for $\theta_0 = 295$ K and $\theta_0 = 302$ K, respectively.

(a)   (b)
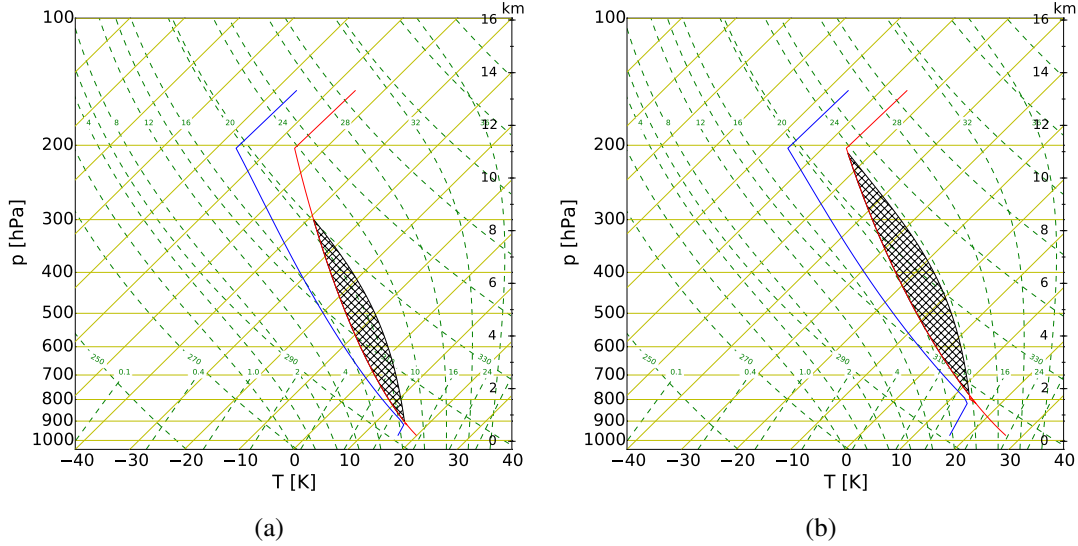
Fig. 4.5.: Skew-T log-p diagrams of temperature profiles (red) and dew point profiles (blue) for (a) $\theta_0 = 295$ K and (b) $\theta_0 = 302$ K. CAPE is represented by the hatched areas.

This variation of the vertical temperature profile with constant surface humidity of 12 g kg^{-1} results in a change of the convective available potential energy (CAPE) from 1048 J kg^{-1} to 1410 J kg^{-1}.

Warm bubble and cold pool characteristics

The thermal triggers, warm bubble and cold pool, are characterized by a temperature perturbation ΔT and a radius R_{hor}. The temperature perturbation describes the maximum initial deviation between the core temperature of the warm bubble or the cold pool and the ambient air. In the warm bubble setup, ΔT ranges from $2\,\mathrm{K}$ (Weisman and Klemp, 1982) to $5\,\mathrm{K}$ (Brooks, 1992). For the cold pool setup ΔT is varied between $-10\,\mathrm{K}$ and $-6\,\mathrm{K}$ (Weisman et al., 1997; Adams-Selin et al., 2013). The radius R_{hor} specifying the horizontal extent of the thermally perturbed air mass ranges from $5\,\mathrm{km}$ to $15\,\mathrm{km}$ for the warm bubble and from $10\,\mathrm{km}$ to $30\,\mathrm{km}$ for the cold pool. Varying the temperature perturbation and the radius leads to different buoyancy gradients of the initial perturbation, which is a measure of the strength of the trigger.

Height and half width of ridge

While the warm bubble and the cold pool are defined by a temperature perturbation and a radius, the ridge is characterized by the height and the half width. The height ranges between $2000\,\mathrm{m}$ and $5000\,\mathrm{m}$, hence it is similar to the height of the Alps and the Rocky Mountains. The half width specifies the horizontal

extent from the center of the mountain ridge to its edge in x-direction at an elevation equal to the half of the maximum height. In this study, the half width is varied between 5 km and 50 km representing both steep and extensive mountains.

4.3.2. Emulator validation

The methods described in section 3.3 are used to evaluate the quality of each emulator fit. Showing all of the available validation plots for all different trigger mechanisms is beyond the scope of this section and thus only a representative selection is presented. The quantile-quantile plots in Fig. 4.6 illustrate the result of the leave-one-out validation for the mean integrated cloud water, the maximum precipitation rate of hail and the integrated graupel content.
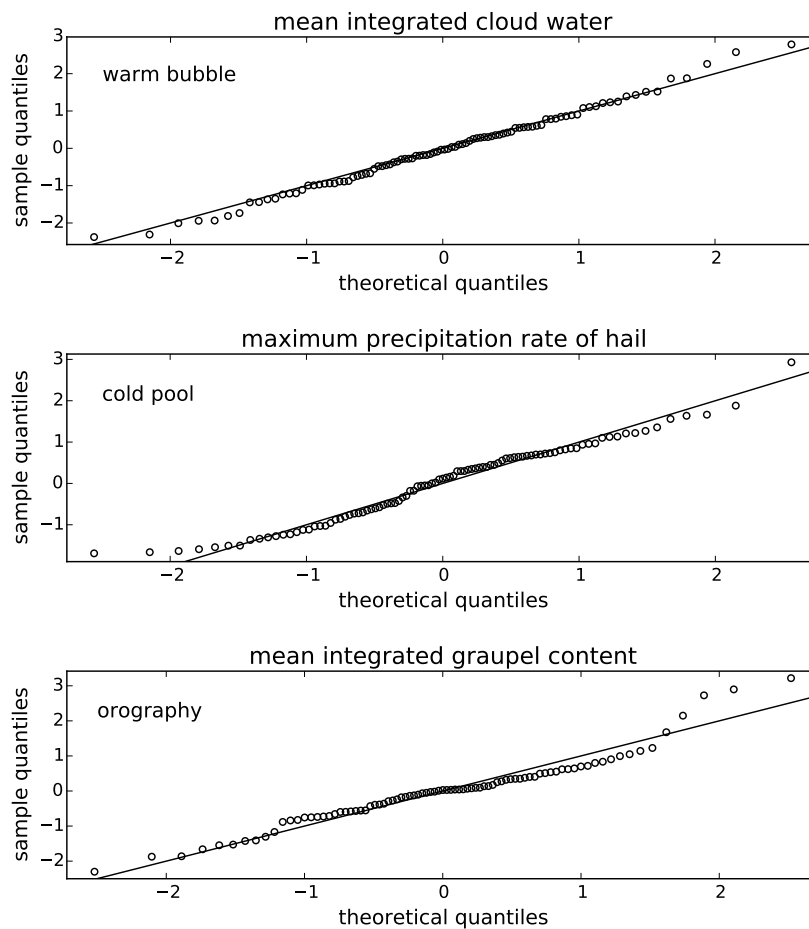
Fig. 4.6.: Quantile-quantile plots for the leave-one-out validation of the emulator for the mean integrated cloud water (warm bubble), the emulator for the maximum precipitation rate of hail (cold pool) and the emulator for the mean integrated graupel content (orography).

It can be seen that in all cases the data points follow the 45 degree line well for the majority of the data range. So no significant under- or overestimation of the variance occurs. However, the points slightly deviate from the 45 degree line towards both the lowest and highest values given on the x-axis.

The individual prediction errors of the validation data sets are shown in Fig. 4.7 where they are plotted against the index of the simulation (4.7a - 4.7c), the model output (4.7d - 4.7f) and the input parameters (4.7g - 4.7o).

The dotted lines denote the absolute values of the individual prediction errors of 2 which is stated by Bastos and O'Hagan (2009) as an approximate threshold indicating discrepancies between the model and the emulator. For the mean integrated snow content, the mean integrated cloud water and the maximum total precipitation there are several outliers visible in Fig. 4.7a to 4.7c, respectively. This could point at fitting problems at parts of the parameter space which can be clarified by Fig. 4.7d to 4.7o. The outliers are rather randomly distributed across the ranges of the respective x-axes and they do not culminate in specific areas. So there is no distinctive pattern visible which leads to the conclusion that there are no systematic errors involved. However, due to the number of outliers, the prediction of the emulator has room for improvement. We obtain the same result when evaluating the emulator prediction versus the model output (Fig. 4.8).

In general the points follow the line of equality but by definition only two to three outliers are acceptable in a set of 45 validation runs. For the example for the cold pool setup (Fig. 4.8a) there are four outliers marked red. Throughout the validation plots of all emulators the number of outliers frequently exceeds the allowed amount (not shown) and thus the emulators cannot be completely validated. Therefore, ten new points are added to the experiment design which are placed in the uncertainty space by a Latin hypercube sampling to fill the gaps between the initial points. The gained results are used to complement the information contained in the training data. New emulators are fitted for the extended training data and the validation results are presented in Fig. 4.8b. For clarity the same points as in Fig. 4.8a are depicted in red. Comparing the two figures shows that the additional training runs improve the emulator predictions: In Fig. 4.8b the 45 degree line is found within the confidence intervals of most of the outliers of Fig. 4.8a. Based on this increase of the prediction accuracy, the number of outliers decreases and the majority of the emulators can be fully validated. There are still some emulators where more than two points do not cross the line of equality but due to the absence of structural errors as shown by the previous validation methods, we consider these as validated, too.

Finally, the robustness of the emulators is evaluated by comparing the results for the variance-based sensitivity (see section 3.4) of emulators generated by ten random samples of the training data. Tab. 4.3 summarizes the mean of the main effect for each input parameter of the warm bubble setup and gives the corresponding range of values for all ten analyses for the robustness test. We find that the smaller the main effect the larger the deviations are; especially for the IN concentration where the main effect is rather small. However, the main contributors to the overall main effect such as the potential temperature show negligible deviations. A visual presentation of Tab. 4.3 is given in Fig. 4.9 where stacked bar charts of the main effects are presented for a selection of four test analyses.
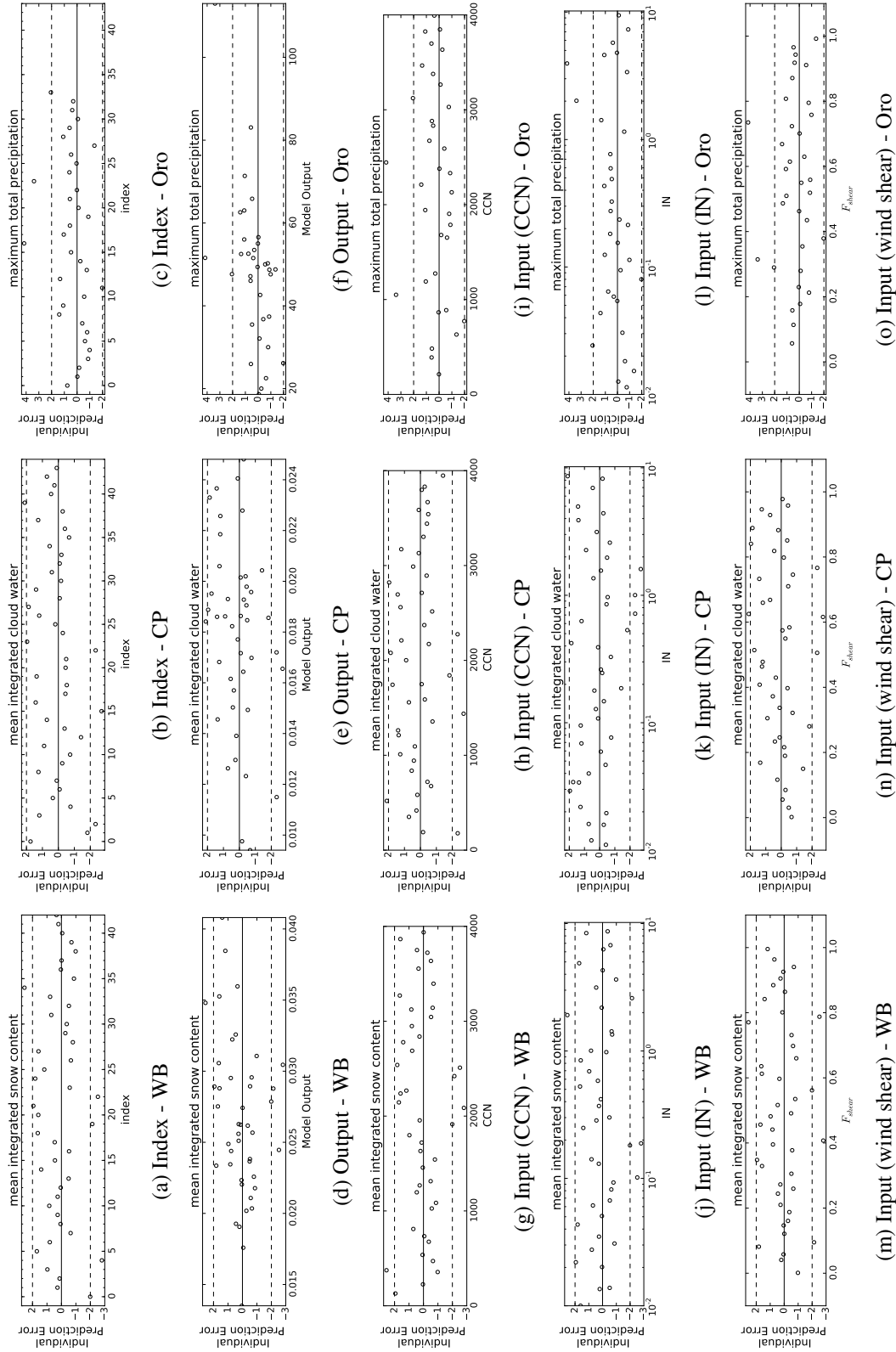
Fig. 4.7.: Individual prediction errors for the validation data of the integrated snow content (warm bubble), the integrated cloud water (cold pool) and the maximum total precipitation (orography) plotted against the index a)-c), the output d)-f) and several input parameters g)-o).
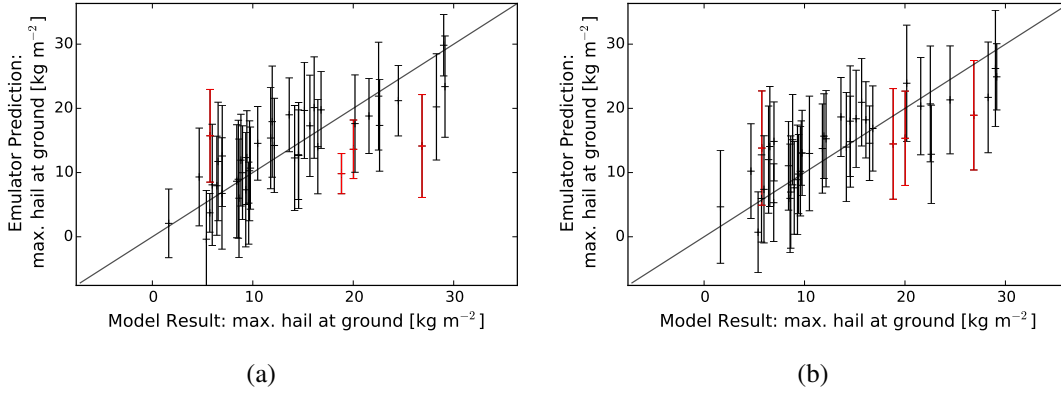
Fig. 4.8.: (a) Emulator predictions of the maximum amount of hail at the ground with 95% confidence intervals versus the model output (cold pool setup). Outliers are depicted in red. (b) Same as (a) but with a larger training data set. For comparison the same points as in (a) are depicted in red.

Tab. 4.3.: Mean main effect and corresponding average deviation per input and output parameter for the warm bubble setup. All numbers are given in %.

	TQC	TQH	TQI	TQG	TQS	TQR
CCN concentration	40.16 ± 2.92	13.98 ± 2.14	4.87 ± 1.28	0.68 ± 0.25	3.36 ± 0.97	5.86 ± 0.66
IN concentration	0.19 ± 0.12	5.51 ± 1.25	0.15 ± 0.12	1.93 ± 0.42	7.82 ± 0.89	0.21 ± 0.15
wind shear (F_{shear})	19.12 ± 1.44	25.53 ± 3.21	8.40 ± 1.07	6.82 ± 1.06	15.87 ± 1.38	42.26 ± 2.25
potential temperature θ_0	13.33 ± 1.80	14.98 ± 1.64	54.54 ± 2.14	51.25 ± 1.90	35.05 ± 1.25	19.56 ± 2.16
temperature perturbation ΔT	8.03 ± 0.73	8.12 ± 2.51	8.76 ± 1.08	10.87 ± 1.43	10.97 ± 1.22	10.20 ± 1.68
radius of warm bubble R_{hor}	9.56 ± 1.02	6.24 ± 1.28	8.71 ± 1.00	13.00 ± 1.01	13.01 ± 0.59	10.90 ± 1.35

It is apparent from Fig. 4.9 that the composition and the relative contributions by the individual input parameters are maintained and that no major changes emerge in the results. Accordingly, we find that the emulator results are robust with respect to variations in the process of building the emulators.

4.4. Setup for variations of the cloud microphysics

4.4.1. Uncertain input parameters

Seven input parameters describing different aspects of cloud microphysics are varied. To compare the impact of CCN and IN in a cloud microphysics context to the aforementioned environmental conditions, these two input parameters are included in this setup as well. Further uncertain input parameters are the fall velocities of the precipitating hydrometeors rain, graupel and hail. Moreover, the intensity of the ice multiplication and the shape parameter of the cloud droplet size distribution are modified. Tab. 4.4 summarizes the considered parameters and their respective ranges. A more detailed description of these
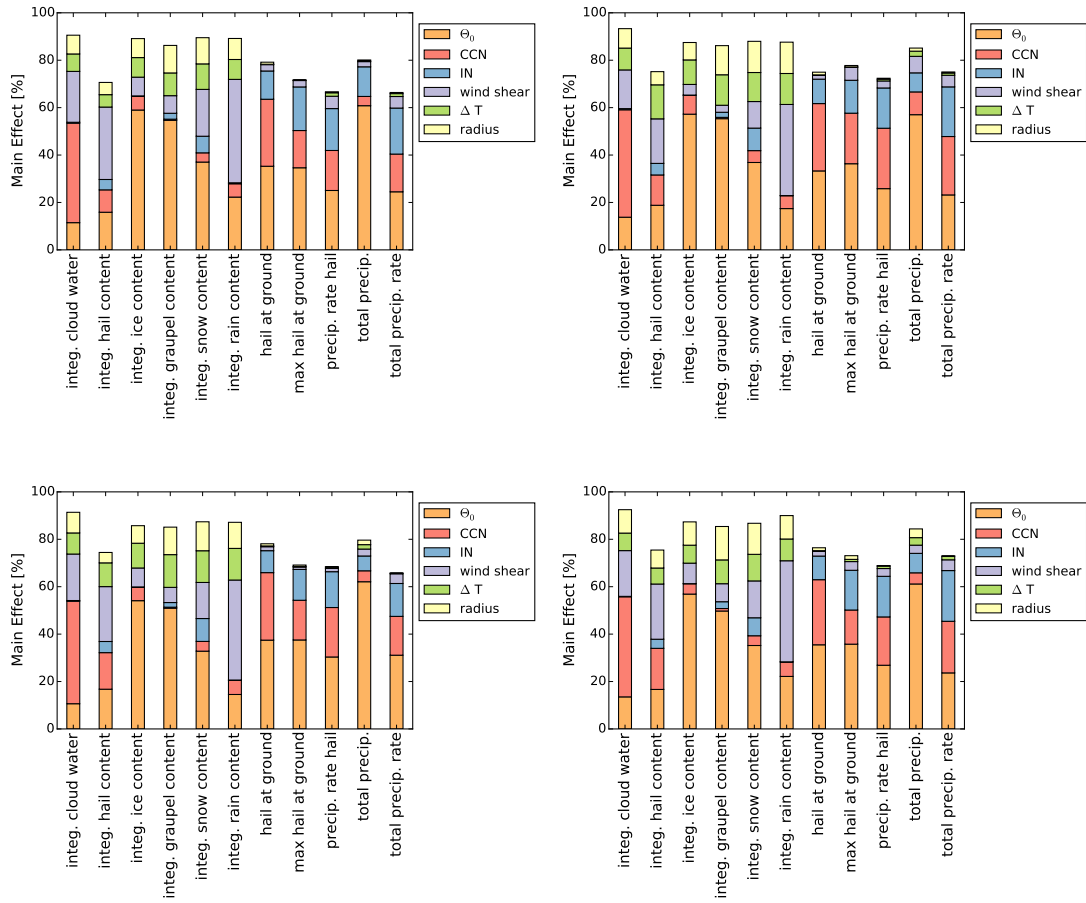
Fig. 4.9.: Results of the sensitivity analysis for four different random samples of the training data when the convection is triggered by a warm bubble.

parameters is given in the following paragraphs. The descriptions of CCN and IN are found in section 4.3.1.

Tab. 4.4.: Overview over the uncertain input parameters and their ranges for the microphysics setup.

input	min	max	comments
CCN concentration	100	4000	cm^{-3}
IN concentration	0.01	10	factor
fall velocity of rain (a_R)	0.3	1.7	factor
fall velocity of graupel (a_G)	0.3	1.7	factor
fall velocity of hail (a_H)	0.7	1.3	factor
ice multiplication	$0.1 \cdot 10^8$	$7 \cdot 10^8$	kg^{-1}
shape parameter	0	8	

Fall velocity of rain, graupel and hail

The fall velocities of the precipitating hydrometers rain, graupel and hail depend on various parameters, for example size, air density and drag coefficient (Houze, 1993) which complicates a physical description of the terminal fall speeds. Thus, mainly empirical equations based on measurements describe the relation between the size or other characteristics of the particles and their fall velocities (Locatelli and Hobbs, 1974; Knight and Heymsfield, 1983). This uncertainty propagates in the microphysics scheme as the fall velocity impacts collision processes such as accretion and riming. In the two-moment scheme, the fall velocities are generally parameterized by

$$v = \alpha x^{\beta} \qquad \qquad [4.8]$$

where x is the mass of the considered particles, the parameters α and β are chosen accordingly (Seifert and Beheng, 2006a). To assess the uncertainty, scaling factors are multiplied to the fall velocities of rain (a_R), graupel (a_G) and hail (a_H) leading to

$$v_S = a_S \cdot \alpha_S x_S^{\beta_S} \qquad \qquad [4.9]$$

where $S \in \{R, G, H\}$. The ranges of the scaling factors are chosen based on the measurements of Yuter et al. (2006) and Knight and Heymsfield (1983) which suggest a spread of about 70% around the mean of the fall velocities of rain and graupel and a spread of about 30% of the fall velocity of hail, respectively.

Ice multiplication

Several studies agree that the number of ice particles in clouds can be orders of magnitude higher than the observed IN concentration (Hobbs et al., 1980; Harris-Hobbs and Cooper, 1987). Different processes are responsible for this finding such as the fragmentation of ice crystals due to collisions (Hobbs and Rangno, 1985). Furthermore, the production of ice splinters during the riming process introduced by Hallet and Mossop (1974) is an additional source of secondary ice particles. As their measurements show a large spread (Hallet and Mossop (1974), Fig. 2), the splintering coefficient of the COSMO model is varied between $0.1 \cdot 10^8$ kg^{-1} and $7 \cdot 10^8$ kg^{-1} to represent the range of their measurements.

Shape parameter of the cloud droplet size distribution

Each of the hydrometeor classes is made up of a broad range of particle sizes. For instance, cloud droplets are defined to a maximum diameter of 0.1 mm. Droplets larger than that are referred to as rain drops that also exist at various sizes (Houze, 1993; Lamb and Verlinde, 2011). The size distribution of the hydrometeors is substantial as various microphysical processes such as condensation or sedimentation depend on the size of the hydrometeors. Thus, uncertainties in the size distributions have several possibilities to affect the processes in the microphysics scheme. By modifying the shape parameter of the cloud droplet size distribution, the variation of the model output due to these input uncertainties is assessed. In the

two-moment scheme of the COSMO model, the size of the cloud droplets is described by a generalized Γ-distribution (eq. [4.1]) (Seifert and Beheng, 2006a) where μ and ν are parameters of the distribution. The default values are $\mu = 0.3333$ and $\nu = 0.0$, respectively. Here, the shape parameter ν is varied between 0 and 8 similar to Igel and van den Heever (2017). Fig. 4.10 shows the size distribution of cloud droplets for these two extreme values. In case of a small value of the shape parameter, the distribution is rather broad whereas it becomes narrow for a large value of ν.
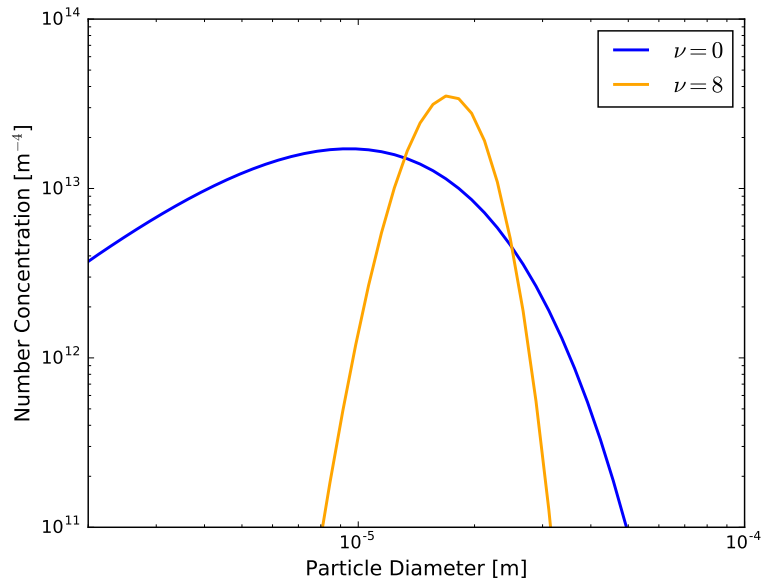
Fig. 4.10.: Size distribution of the cloud droplets for shape parameter values of $\nu = 0$ and $\nu = 8$.

4.4.2. Emulator validation

The emulators are validated via the methods described in section 3.3. A selection of plots gives an overview of the validation methods. In Fig. 4.11, quantile-quantile plots are shown for an example output of each setup. The points are supposed to follow the $45°$ line for a good agreement of the theoretical and sample quantiles. It can be seen from Fig. 4.11 that the $45°$ line is well represented except for the edges where small deviations occur. Thus, the variance is not considerably under- or overestimated. The individual prediction errors are illustrated in Fig. 4.12 for the total precipitation rate in the warm bubble setup, the integrated ice content in the cold pool setup and the integrated rain content in the orography setup. Fig. 4.12a-4.12c show the individual prediction error for the index of the validation runs, Fig. 4.12d-4.12f for the corresponding output and Fig. 4.12g-4.12o for different input parameters. The dashed lines represent the threshold for outliers given by Bastos and O'Hagan (2009). It can be seen that the outliers are not connected to specific values of the in- or output as they are randomly distributed in Fig. 4.12d-4.12o.
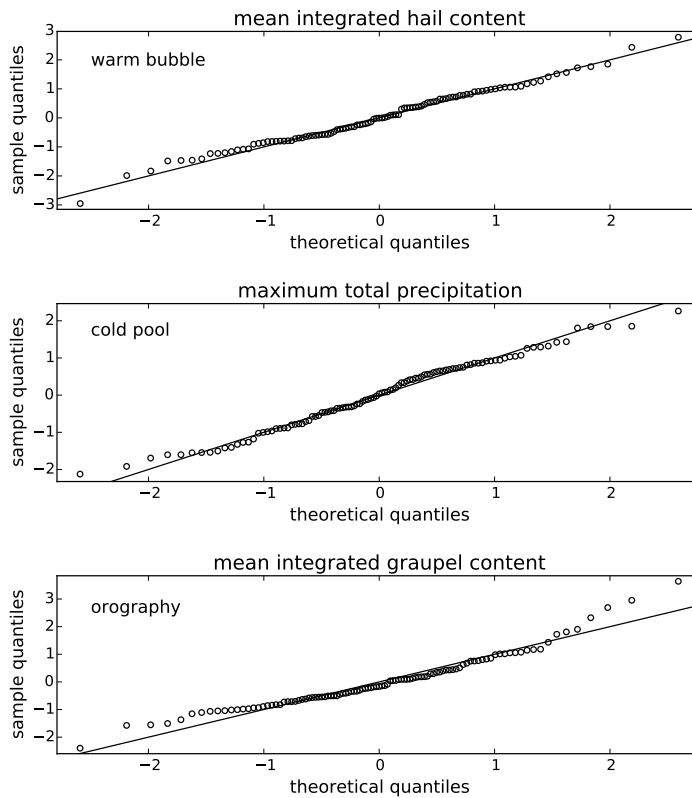
Fig. 4.11.: Quantile-quantile plots for the leave-one-out validation of the emulator for the mean integrated hail content (warm bubble), the emulator for the maximum total precipitation (cold pool) and the emulator for the mean integrated graupel content (orography) for the sensitivity experiment varying cloud microphysics parameters.

In addition, the emulator prediction is plotted against the actual model output for a chosen output of each trigger mechanism in Fig. 4.13. The bars denote the 95% confidence bounds and outliers are colored red. If the emulator represents the model well, the points follow the line of equality. An emulator is considered valid, if there is a maximum number of two to three points whose confidence bounds do not cross the line of equality. As Fig. 4.13 reveals, the number of outliers for these examples is within the allowed amount and the emulators are able to reproduce the original model data. Several emulators for other variables exhibit up to five or six outliers (not shown). However, the confidence bounds of these outliers are still close to the 45° line. In addition, the quantile-quantile plots and the plots of the individual prediction errors do not suggest systematic errors and therefore all of the constructed emulators are considered valid.

Finally, the robustness of the validated emulators is tested. For this purpose ten random sets of new validation runs are generated from the training data set and the remaining runs are used as new training data. The results of the variance-based sensitivity analysis are compared. In Tab. 4.5 the mean main effect of all ten scenarios is evaluated and the corresponding average deviations are given.
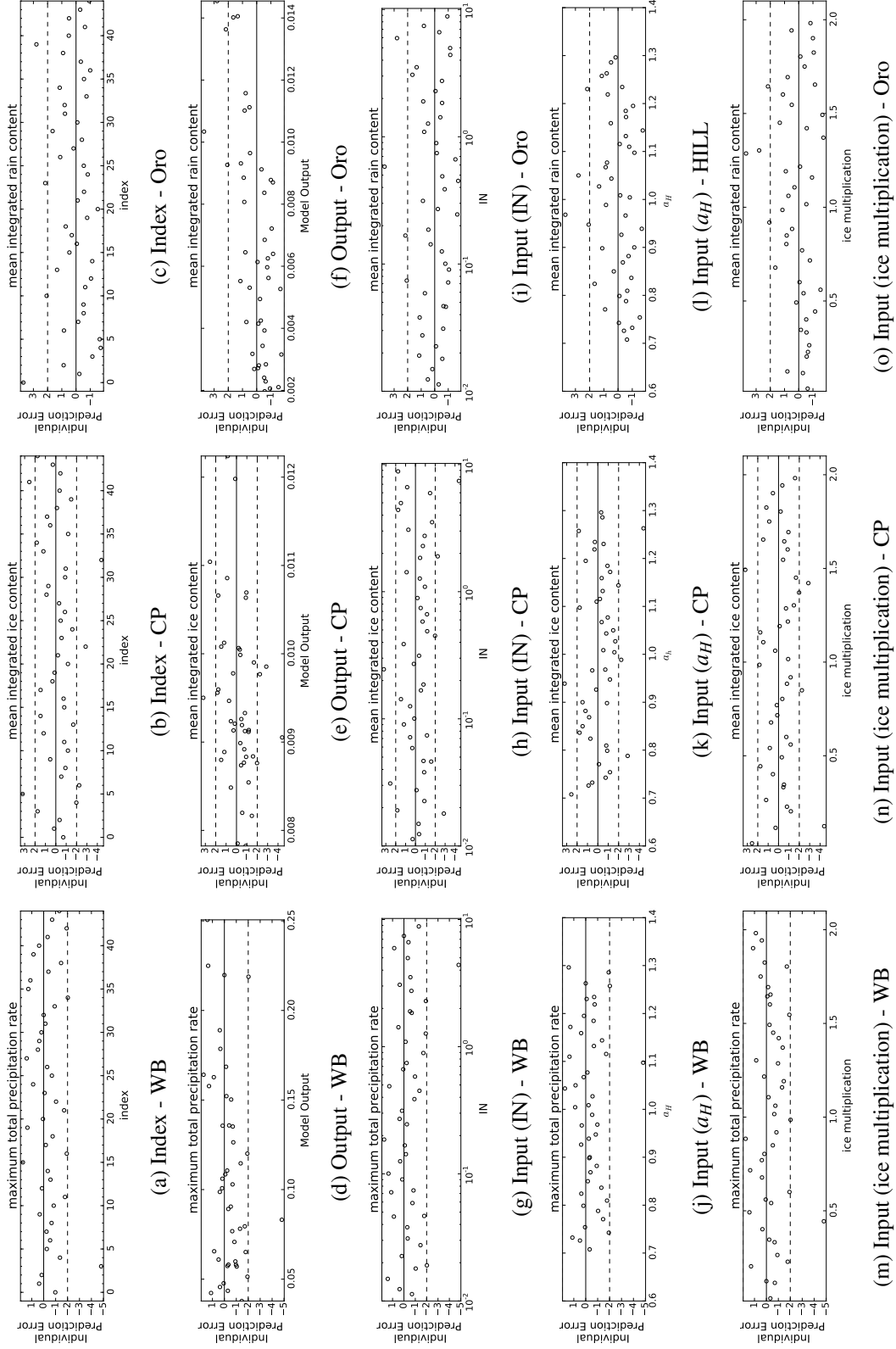
Fig. 4.12.: Individual prediction errors for the validation data of the maximum total precipitation rate (warm bubble), the mean integrated ice content (cold pool) and the mean integrated rain content (orography) plotted against the index a)-c), the output d)-f) and several input parameters g)-o) for the sensitivity experiment varying cloud microphysics parameters.

| (a) warm bubble | (b) cold pool | (c) orography |
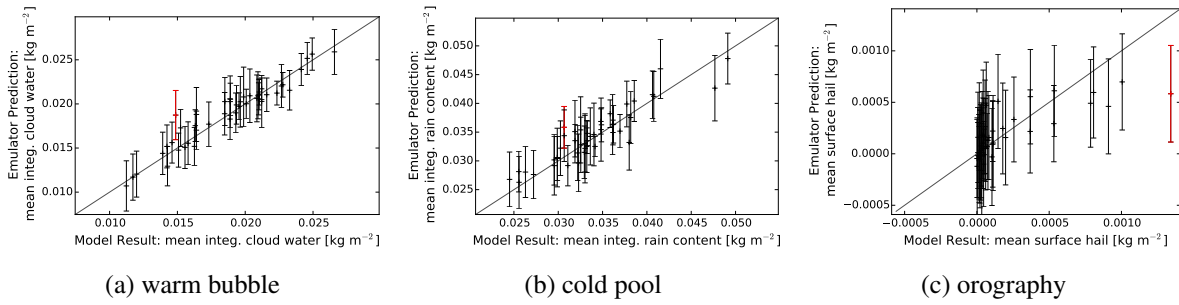
Fig. 4.13.: Emulator prediction with 95% confidence bounds plotted versus the original model output for example output of (a) the warm bubble setup, (b) the cold pool setup and (c) the orography setup for the sensitivity experiment varying cloud microphysics parameters. Outliers are depicted in red.

Tab. 4.5.: Mean main effect and corresponding mean difference per input and output parameter for the orography setup. All numbers are given in %.

	TQC	TQH	TQI	TQG	TQS	TQR
CCN concentration	20.19 ± 1.76	0.51 ± 0.44	9.57 ± 1.67	0.16 ± 0.13	7.70 ± 1.61	0.76 ± 0.58
IN concentration	3.06 ± 0.61	9.00 ± 1.09	39.98 ± 2.49	4.14 ± 0.69	12.38 ± 2.75	11.66 ± 3.58
fall velocity of rain (a_R)	0.42 ± 0.26	2.39 ± 1.18	0.41 ± 0.33	0.55 ± 0.28	0.58 ± 0.43	0.81 ± 0.92
fall velocity of graupel (a_G)	63.53 ± 4.35	68.00 ± 3.80	36.52 ± 1.57	77.37 ± 3.06	64.16 ± 3.61	66.80 ± 7.10
fall velocity of hail (a_H)	0.41 ± 0.37	7.41 ± 1.89	0.38 ± 0.16	0.35 ± 0.34	0.68 ± 0.47	0.69 ± 0.50
ice multiplication	4.04 ± 1.53	0.35 ± 0.29	2.27 ± 0.47	5.76 ± 1.28	3.99 ± 1.55	7.70 ± 2.41
shape parameter v	0.42 ± 0.47	1.20 ± 0.57	2.91 ± 1.17	1.00 ± 0.53	0.31 ± 0.28	2.76 ± 1.66

For small mean values of the main effect the deviations are quite high being almost as large as the mean itself, whereas for higher mean values of the main effect the deviations are comparably low. This means that the key features and the composition of the overall main effects are generally the same and thus the emulators are robust to changes in the training data set. Fig. 4.14 presents four results of the variance-based sensitivity analysis for the orography setup as stacked bar plots.

It is found that the composition and the main contributors to the overall main effect are well represented in each plot. Although the amount of interaction effects slightly varies, each plot leads to the same result and the conclusion found from Tab. 4.5 is emphasized.
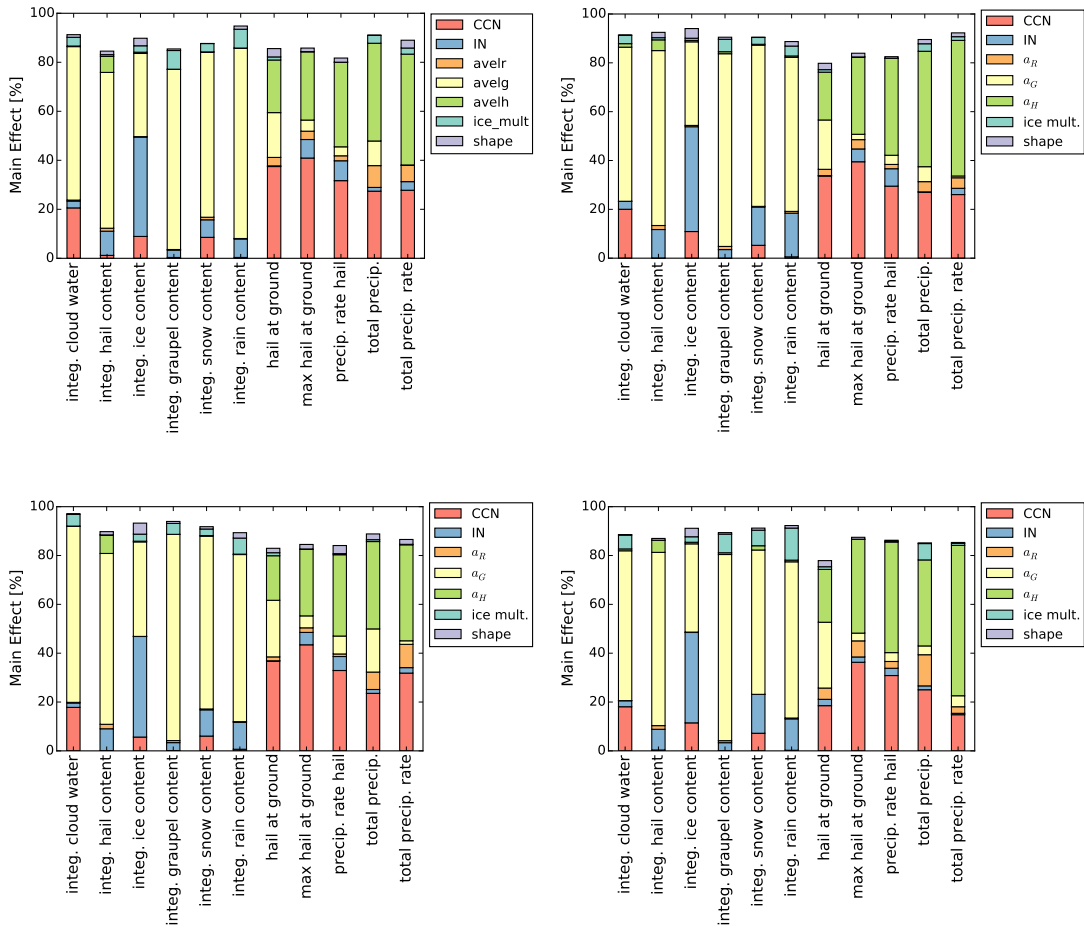
Fig. 4.14.: Results of the sensitivity analysis for four different random samples of the training data when the convection is triggered by a mountain ridge.

4.5. Setup for variations of both the environmental conditions and the cloud microphysics

4.5.1. Uncertain input parameters

Based on the results of the previous two setups, where the environmental conditions and the cloud microphysics are treated separately, the input parameters of this combined setup are chosen such that the most important parameters of both environmental conditions and microphysics are considered in addition to the CCN and IN concentrations. For the variations of the environmental conditions the parameters identified to affect the uncertainty most are the wind shear and the potential temperature θ_0. The relevant parameters of the microphysics setup are the fall velocity of graupel and the fall velocity of hail. Detailed descriptions of the input parameters are found in section 4.3.1 and section 4.4.1. Moreover, the same parameter ranges as in the previous setups are used. Tab. 4.6 summarizes the considered parameters and their ranges.

Tab. 4.6.: Overview over the uncertain input parameters and their ranges for the third setup combining variations of the environmental conditions and the microphysics.

input	min	max	comments
CCN concentration	100	4000	cm^{-3}
IN concentration	0.01	10	factor
wind shear	0	1	factor
θ_0	295	302	K
fall velocity of graupel (a_G)	0.3	1.7	factor
fall velocity of hail (a_H)	0.7	1.3	factor

4.5.2. Emulator validation

The methods described in section 3.3 are used to validate the emulators. First, quantile-quantile plots are considered for each trigger mechanism in Fig. 4.15. As the residuals of the sample follow a Student-t distribution, the sample quantiles and the theoretical quantiles of the Student-t distributions are supposed to be equal. Thus, the closer the points are to the 45° line the better the theoretical distributions is represented.

Fig. 4.15 shows that the center parts of the distribution are well approximated. Towards the lower and upper limits the sample deviates from the theoretical distribution, however the differences are small such that the variability is neither under- nor overestimated.

The individual prediction error is illustrated as a function of the index, the output and some input parameters in Fig. 4.16. This figure reveals that for most of the validation data, the emulator prediction is within the allowed range. The few outliers are not connected to specific output values or parts of the input parameter space as they are quite distributed and not accumulating in a particular region of the plots. Therefore, there are no systematic errors and the emulators are validated via this method despite the small number of outliers.

Another approach to validate the emulators is to plot the emulator prediction and its confidence bounds as a function of the model output. This is done in Fig. 4.17. As the 95% confidence bounds are depicted, 95% of the validation points are required to cross the 45° line with their confidence bounds to validate the emulator. Thus, two to three outliers are allowed for a set of 45 validation points.

The examples in Fig. 4.17 indicate that for all trigger mechanisms the allowed number of outliers is not exceeded for these chosen outputs. In the warm bubble and cold pool setups, the two validation points marked red are quite close to the 45° line which means that the prediction is still close to the model output. In the orography setup, three outliers are found. While one of them is close to the line of equality, there is a gap between the other two points and the 45° line. Yet, this emulator of the orography
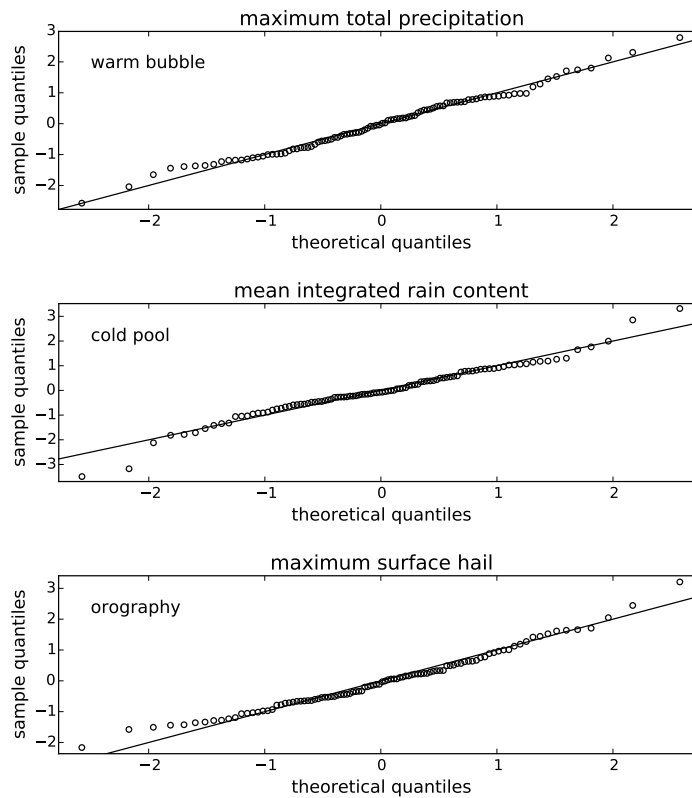
Fig. 4.15.: Quantile-quantile plots for the leave-one-out validation of the emulator for the maximum total precipitation (warm bubble), the emulator for the mean integrated rain content (cold pool) and the emulator for the maximum precipitation of hail (orography).

setup is validated as three outlier are still acceptable. In general, there are emulators where more than three validation points do not cross the line of equality. However, all validation methods are taken into account such that an emulator where four or five validation points are outliers is still considered valid as long as no validation method indicates systematic errors.

Finally, the robustness of the emulators is analyzed. Thus, from the combined data set of training and validation data a new set of validation points is randomly chosen and the remaining data points are considered as training data. This process is repeated ten times and the results of the sensitivity analysis are compared. The mean of the main effects of each input parameter and the corresponding mean difference are listed in Tab. 4.7 for the cloud variables of the cold pool setup.

Overall, the result of the sensitivity analysis is quite robust. The spread of the results scales inversely with the main effect such that relative deviations are larger for small main effects and smaller for large main effects. This means that the main contributions to the output uncertainties vary only in a limited range, whereas the variations of the minor contributions are larger. Thus, the composition of the overall main effect is similar as the same main contributions are found in all random data sets. That behavior is underlined by the graphical representation given in Fig. 4.18.
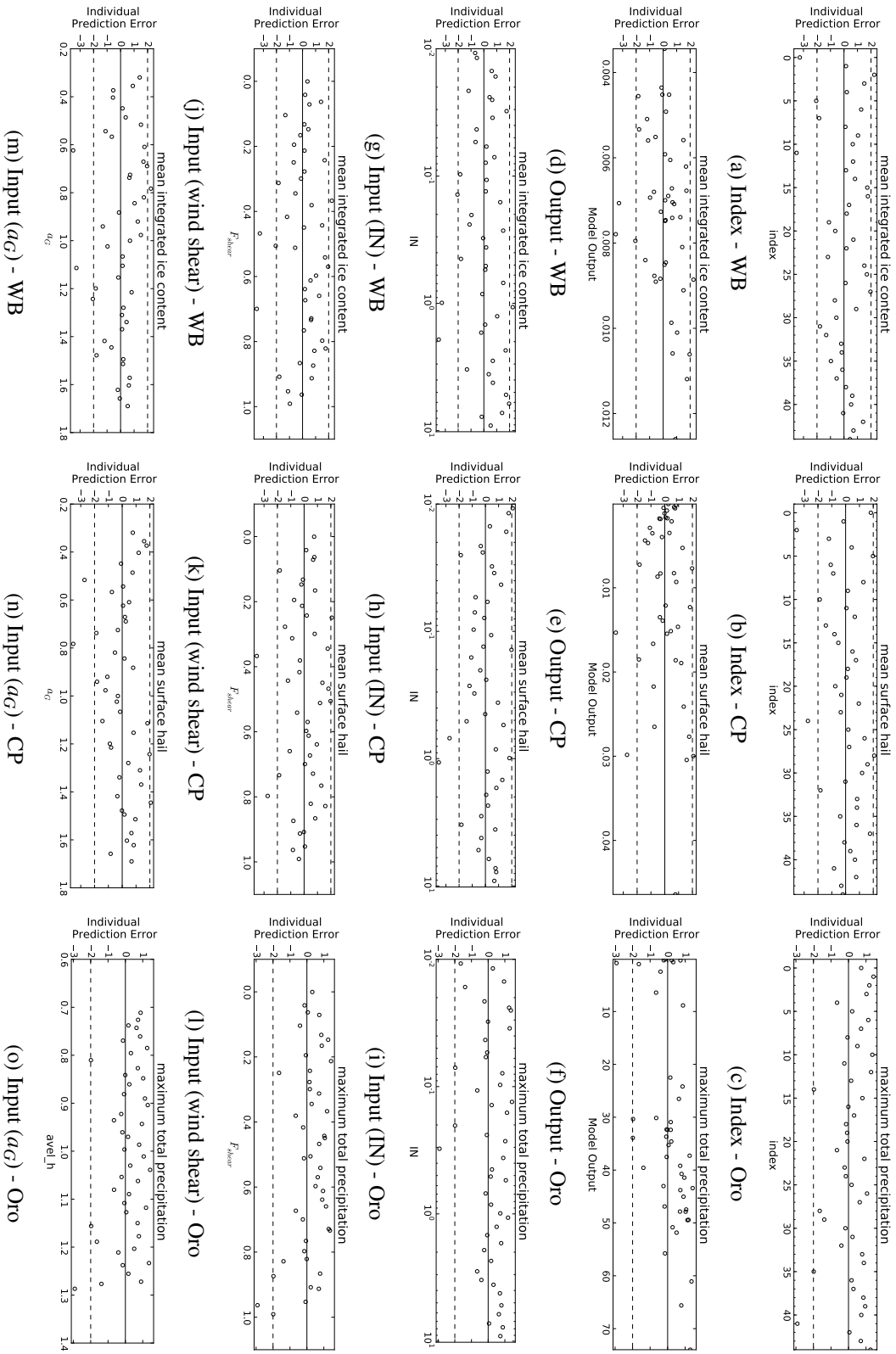
Fig. 4.16.: Individual prediction errors for the validation data of the integrated ice content (warm bubble), the mean precipitation of hail (cold pool) and the maximum total precipitation (orography) plotted against index a)-c), output d)-f) and several input parameters g)-o).

(a) warm bubble   (b) cold pool   (c) orography
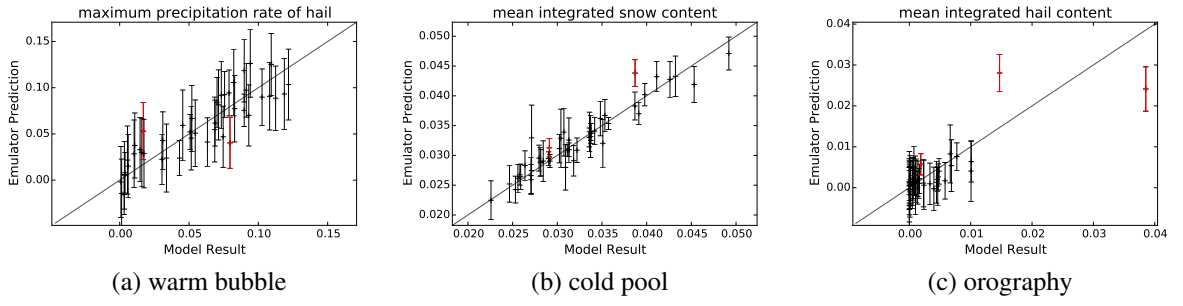
Fig. 4.17.: Emulator prediction with 95% confidence bounds plotted versus the original model output for example output of (a) the warm bubble setup, (b) the cold pool setup and (c) the orography setup. Outliers are depicted in red.

Tab. 4.7.: Mean main effect and corresponding mean difference per input and output parameter for the cold pool setup. All numbers are given in %.

	TQC	TQH	TQI	TQG	TQS	TQR
CCN concentration	61.77 ± 1.15	8.02 ± 0.90	8.31 ± 1.16	1.16 ± 0.10	7.46 ± 0.60	10.33 ± 0.56
IN concentration	0.06 ± 0.09	1.95 ± 0.63	0.79 ± 0.37	0.65 ± 0.11	10.66 ± 0.66	0.17 ± 0.12
wind shear (F_{shear})	8.62 ± 1.12	3.51 ± 0.92	3.44 ± 0.95	0.46 ± 0.13	12.46 ± 1.21	29.69 ± 1.24
potential temperature θ_0	21.27 ± 0.95	13.22 ± 0.46	53.24 ± 2.33	5.22 ± 0.22	13.52 ± 0.61	21.06 ± 1.40
fall velocity of graupel (a_G)	1.76 ± 0.34	27.00 ± 0.97	16.18 ± 2.00	87.58 ± 0.24	40.50 ± 1.39	18.15 ± 1.10
fall velocity of hail (a_H)	0.06 ± 0.03	31.70 ± 2.02	0.04 ± 0.02	0.03 ± 0.02	0.06 ± 0.03	12.71 ± 0.98

Here, the main effects of four of these training data sets, which are randomly chosen from all training and validation runs, are shown. As indicated by Tab. 4.7 the main contributions to the output uncertainty vary only marginally such that all four plots look approximately the same.

To sum up, the emulators built for this analysis, where both the environmental conditions and the cloud microphysics are perturbed, are validated by various approaches which allows the conclusion that the emulators can be employed for the sensitivity studies without restrictions.
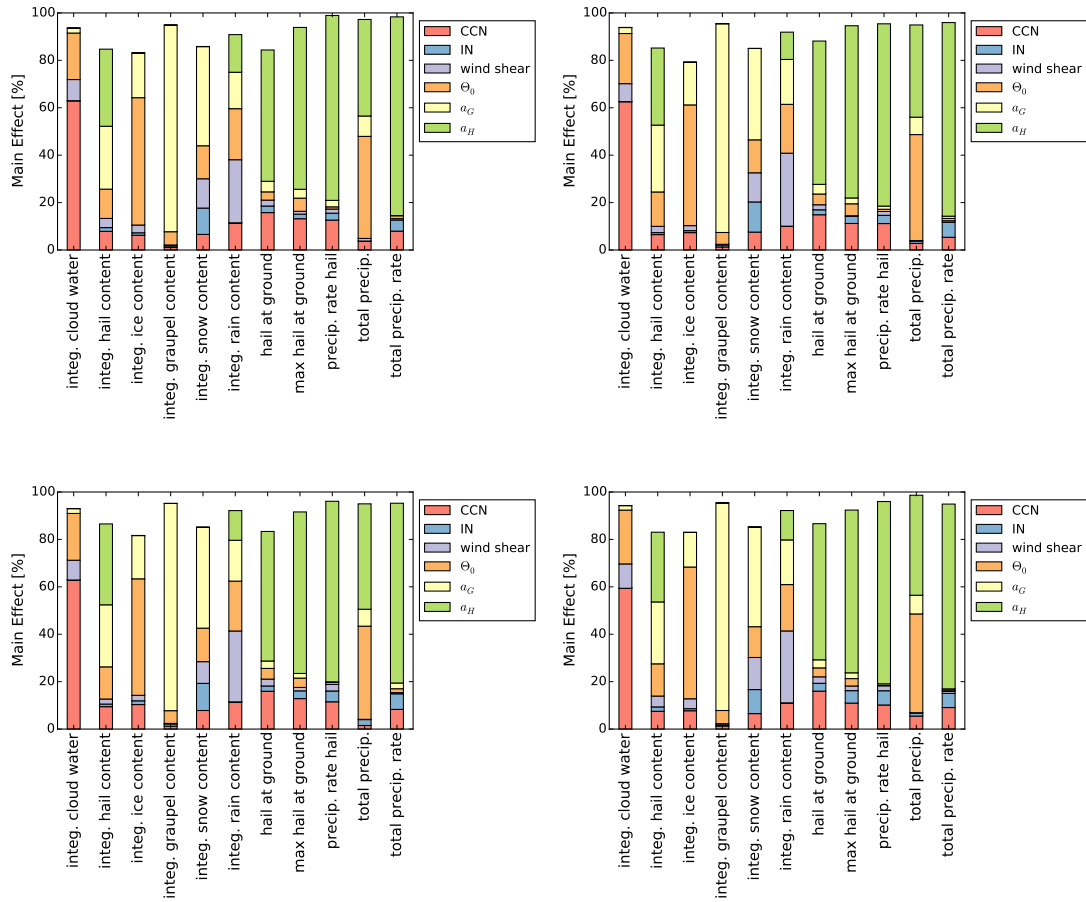
Fig. 4.18.: Results of the sensitivity analysis for four different random samples of the training data when the convection is triggered by a cold pool.

5. Emulator Studies for Different Environmental Conditions

This chapter contains the results of the study where the impact of the environmental conditions is analyzed. The CCN and IN concentrations, wind shear, θ_0 and the trigger characteristics (temperature perturbation and the radius for the warm bubble and cold pool setups; height and half width of the mountain ridge for the orography setup) are used as uncertain input parameters. A detailed description of the input parameters is given in section 4.3.1.

Part of the results and discussion presented in this chapter are published in a modified version as Wellmann et al. (2018).

5.1. Cloud variables and precipitation

In order to distinguish the contribution of the input parameters to the uncertainty of the model output, a variance-based sensitivity analysis is performed where the input parameters are varied according to Tab. 4.2. The main effects, which state the individual contribution of each input parameter to the output variance, are shown as stacked bar plots in Fig. 5.1. If the main effects do not add up to 100%, this means that there are further contributions from interacting parameters.

Comparing the overall appearance of Fig. 5.1a - 5.1c, it can be found that the added values of the main effects reach 80% for most of the output variables in the warm bubble and cold pool setups, whereas in the orography setup only few bars reach this percentage. Hence, on the one hand large parts of uncertainty in the warm bubble and cold pool output can be explained by first order main effects. On the other hand, interaction effects, which are represented by the difference to 100%, contribute substantial parts to the output uncertainty in the orography setup. This implies that the input parameters are interacting more to jointly affect the uncertainty. A possible explanation for this is that the bell-shaped mountain ridge may trigger several cells along the ridge simultaneously forming a complex system where the parameters are interacting more compared to the single cell triggered in the warm bubble and cold pool setups. Looking at the mean of the integrated cloud variables in Fig. 5.1a - 5.1c reveals that for all three trigger mechanisms the potential temperature at the ground θ_0, used in the Weisman-Klemp thermodynamic profiles, contributes to the uncertainty of these variables. Via eq. [4.7] θ_0 directly determines CAPE which is transformed into kinetic energy of ascending air parcels. So CAPE affects the updraft velocity and thus the storm organization. In addition, θ_0 is a controlling factor of the moisture availability. Consequently, it acts as source of uncertainty for the integrated masses of the hydrometeors. In the warm

(a) warm bubble

(b) cold pool

(c) orography
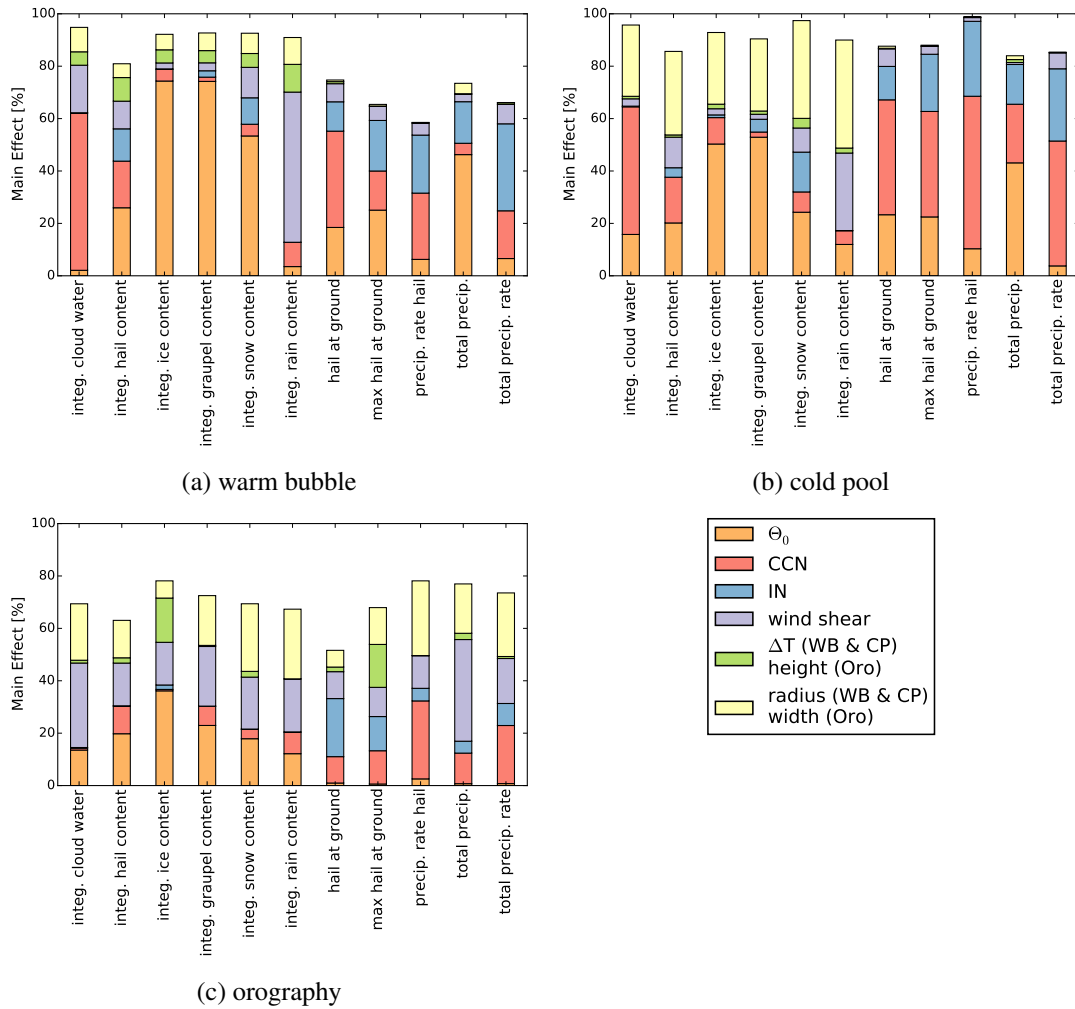
Fig. 5.1.: Bar plot of the main effect for integrated cloud variables and precipitation when (a) a warm bubble, (b) a cold pool, (c) a mountain ridge is used as trigger mechanism.

bubble and cold pool setups, the main effect of θ_0 reaches the highest values for the integrated content of ice and graupel. For the integrated cloud water and rain content, the potential temperature θ_0 has only a minor contribution compared to the other uncertain input parameters. In the orography setup, θ_0 adds 36% to the output uncertainty of the integrated ice content and about 20% to the other variables. The CCN concentration has a considerable main effect of 60% for the integrated cloud water in the warm bubble setup and of 49% in the cold pool setup. The effect on the remaining variables is about 17% or less. In contrast, the main effect of the CCN concentration is less than 1% for the integrated cloud water and less than 10% for the other hydrometeors in the orography setup. In the warm bubble and the cold pool setup, the uncertainty of the IN concentration takes an effect only on the integrated snow, graupel and hail content where the contribution reaches up to 15% for the integrated snow content in the cold pool setup. In the orography setup, the IN concentration adds less than 2% for all integrated cloud variables. The percentage of the main effect of the wind shear varies for the considered output variables

in the warm bubble and cold pool setup. While for the integrated ice and graupel content the contribution of the wind shear is almost negligible, there are contributions for the remaining variables, going up as high as 40% for the rain content in the warm bubble setup. This relates to the impact of the wind shear on the convectively generated cold pool and the connected evaporation of rain, as discussed e.g. by Weisman and Klemp (1982) and Weisman et al. (1997). Furthermore, rain is advected in COSMO for high-resolution simulations (Doms and Baldauf, 2015) and thus it is directly affected by variations of the wind field. In the orography setup, the contribution of the wind shear is comparable for all cloud variables varying between 32% for the integrated cloud water and 16% for the hail and ice content. The contribution from the trigger characteristics to the uncertainties varies for each trigger mechanism. In the warm bubble setup, both the temperature perturbation ΔT and the radius of the warm bubble add about 14% to the overall main effect of all cloud variables. In the cold pool setup, the initial size of the cold pool affects the results more clearly. For example up to about 41% of the uncertainty in the amount of the integrated rain content can be attributed to the radius. However, the contribution of the temperature perturbation is hardly visible. In the orography setup, the properties of the mountain ridge explain in combination approximately the same amount of uncertainty as the wind shear where the half-width is more dominant than the height. For the precipitation variables, the main effects in the warm bubble and cold pool setup show a similar behavior where the overall main effect consists of contributions from θ_0, the CCN concentration and the IN concentration. The main effect of θ_0 is below 20% except for the total precipitation where it is above 40% in both setups. The contribution from the CCN concentration varies between 4% for the total precipitation and 37% for the mean amount of hail at the ground in the warm bubble setup, whereas it varies between 22% and 48% in the cold pool setup. Further, the IN concentration accounts for about $7 - 33\%$ of the overall main effect. Compared to θ_0 and the CCN and IN concentrations, the remaining input parameters have only minor contributions. In the orography setup, the potential temperature does not contribute. However, there are additional contributions from the height and the half width of the mountain ridge that add up to 30% to the output uncertainties. These results allow for the conclusion that the properties of the orography lead to higher uncertainty in the output of the precipitation variables than the properties of the thermal perturbations.

Summing up, the analysis of the main effect shows that for most output variables the uncertainty in the input of the potential temperature is the largest contributor to their uncertainty. The contribution of the remaining parameters varies for each output parameter. For example, there are significant contributions from the CCN and IN concentrations to the output uncertainty of the precipitation variables in the warm bubble and cold pool setups, whereas in the orography setup the wind shear shows moderate contributions to the uncertainty of all considered output variables. Furthermore, it can be seen that the composition of an output's main effect differs for each of the trigger mechanisms. In addition, the role of interaction effects changes depending on the chosen setup. This leads to the conclusion that for this particular set of input parameters the convection trigger determines how the uncertainty in the input proceeds to the output uncertainty of integrated cloud variables and precipitation variables.

So far the whole parameter space has been considered for the analysis which was chosen to cover a wide range of atmospheric conditions. For example, the potential temperature was varied in a range of 7 K. By definition the main effect indicates how much the variance in the output could be reduced if the input parameter was known exactly (Johnson et al., 2015). However, the forecast of the temperature is typically more precise. Thus, as a second step, the parameter space used for the sensitivity analysis is now related to an approximate typical uncertainty of the numerical weather prediction model COSMO in an operational setup for Central Europe. Tab. 5.1 gives an overview of the adapted input parameter ranges.

Tab. 5.1.: Changes of the parameter ranges of the uncertain input parameters when related to forecast errors.

input	min	max	units
wind shear (F_{shear})	0.3333	0.6666	factor
θ_0 (WK profile)	299	301	K
height of ridge (Oro)	3000	4000	m
halfwidth of ridge (Oro)	26500	28500	m

The ranges of the wind shear and θ_0 are derived from their root mean square errors of the COSMO prediction (provided by Felix Fundel, DWD, personal communication). The ranges for the height and the halfwidth of the mountain ridge are estimated as the maximum change of terrain that is not resolved by the model grid. These new ranges are centered around the center of the original parameter ranges. The remaining input parameters are not part of the operational model forecast and thus their possible range cannot be restrained. Nevertheless, the trigger characteristics of the warm bubble and the cold pool represent values used in other studies before (Brooks, 1992; Brooks and Wilhelmson, 1992; Adams-Selin et al., 2013; James et al., 2006). Also the chosen ranges of CCN and IN concentrations are found throughout Europe (Bougiatioti et al., 2009; Boose et al., 2016). As the possible parameter range is now reduced to average forecast errors or resolution errors, the overall composition of the bar plots changes. Mainly, the main effect of the potential temperature, which was dominant in Fig. 5.1, is considerably reduced.

In the warm bubble setup (Fig. 5.2), the highest contribution of θ_0 is found for the total precipitation where it reaches up to 8% compared to values of about 46% in the full parameter range. For all other variables the contribution is less than that. Thus, other input parameters emerge to explain the output uncertainty. For the integrated cloud variables, the characteristics of the warm bubble are responsible for up to 50% of the uncertainty and also the contribution from the CCN concentration has more than doubled for the hydrometeors of the ice phase. However, the IN concentration adds 48% being the largest contributor for the integrated snow content. A noticeable amount of the main effect of the wind shear and the IN concentration can be found for all variables of the ice phase, whereas their main effect is
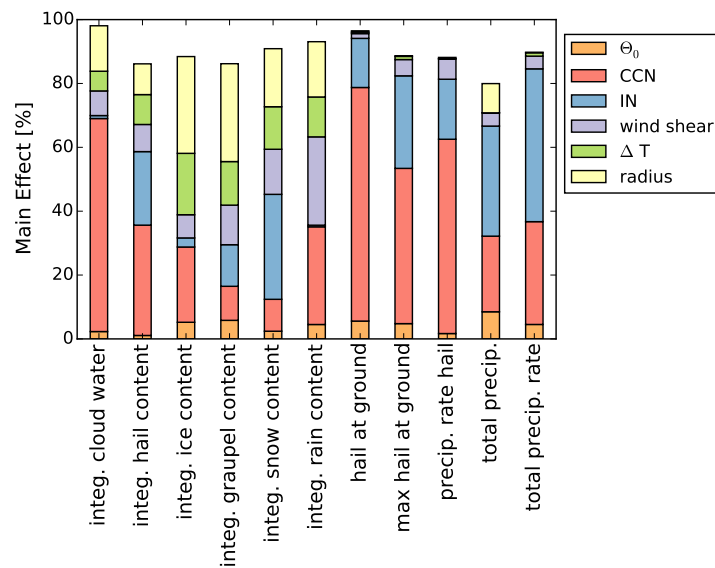
Fig. 5.2.: Bar plot of the main effect for integrated cloud variables and precipitation using a warm bubble as trigger mechanism when the parameter space is restrained by mean forecast errors.

reduced for the integrated cloud water and rain content. Regarding the precipitation variables, the warm bubble characteristics and wind shear are only of minor importance; instead the overall main effect is dominated by the CCN and IN concentrations. For the variables describing precipitation of hail, the CCN concentration covers at least 49% whereas for the total precipitation, the IN concentration is the major contributor with values up to 48%. Additionally, the overall main effect is higher which means that less interaction effects arise.
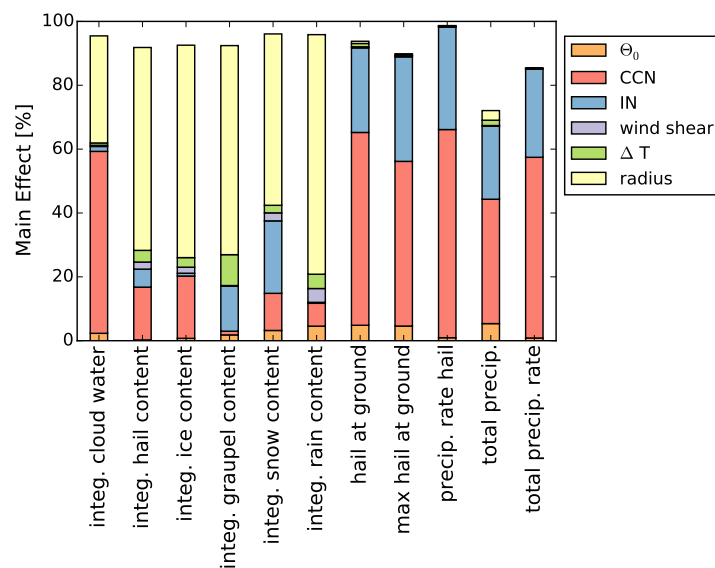
Fig. 5.3.: Bar plot of the main effect for integrated cloud variables and precipitation using a cold pool as trigger mechanism when the parameter space is restrained by mean forecast errors.

In the cold pool setup (Fig. 5.3), the main effect of θ_0 is clearly reduced compared to the original parameter range and thus the output uncertainty of the integrated cloud variables is dominated by the main effect of the radius of the cold pool. In addition to the contribution from the radius, the variables show a contribution from the CCN concentration while a contribution from the IN concentration is also found for the snow and graupel contents. In contrast, the uncertainty of the precipitation variables hardly depends on the radius of the initial cold pool. For these variables mainly the CCN concentration and the IN concentration contribute to the overall main effect.
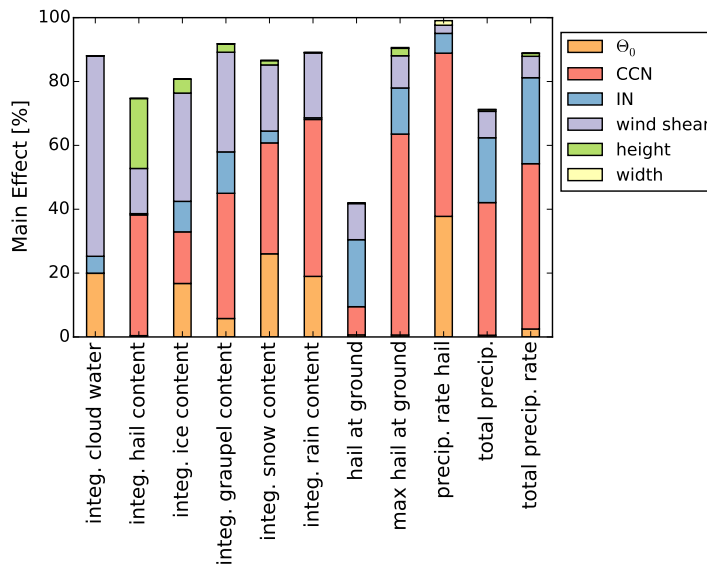
Fig. 5.4.: Bar plot of the main effect for integrated cloud variables and precipitation using a mountain ridge as trigger mechanism when the parameter space is restrained by mean forecast errors.

In the orography setup (Fig. 5.4), the impact of θ_0 is not reduced as much as in the warm bubble and cold pool setups. Nevertheless, the main effect of the CCN concentration has the largest contribution varying between 16% and 49%. Furthermore, the main effect of the wind shear ranges around 14% for the integrated hail content and around 63% for the integrated cloud water. Looking back at Fig. 5.1c, the sensitivity analysis using the whole parameter space showed that the sum of the main effects cannot explain all of the output uncertainty and that there is a considerable contribution from interaction effects. However, when restraining the parameter space as given in Tab. 5.1, the main effect of the input parameters is responsible for more than 80% of the uncertainty of the output except for the integrated hail content. This leads to the conclusion that these interactions were mainly happening between the restrained parameters θ_0, wind shear and height and half-width of the mountain ridge. In order to confirm this hypothesis the interaction effect using the whole parameter space is plotted in Fig. 5.5. This interaction effect states how much each of the input parameters is involved in joint contributions to the output uncertainty of two or more parameters. For example, if the combined effect of the wind shear and

θ_0 is 10%, this amount is added to the interaction effect of both the wind shear and θ_0. Thus, the height of these bars is larger than the blank space above the bars in Fig. 5.1c.
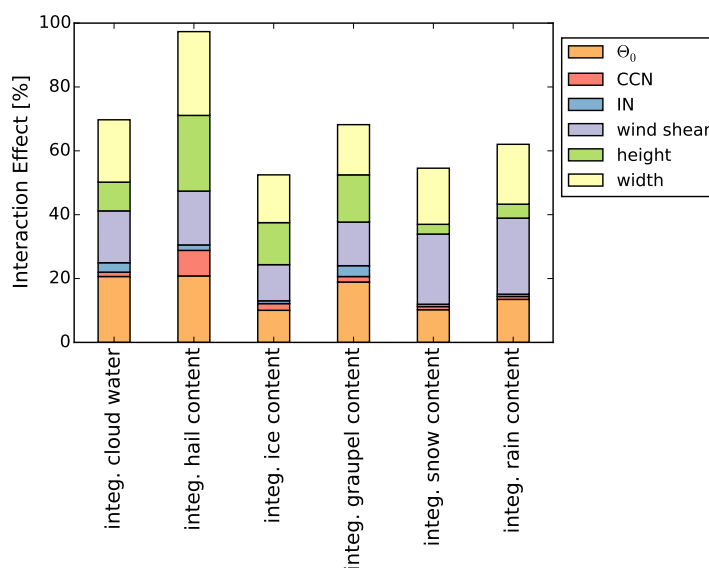
Fig. 5.5.: Bar plot of the interaction effect for integrated cloud variables and precipitation using a mountain ridge as trigger mechanism.

It can be seen that for the integrated cloud variables primarily θ_0, wind shear, the height and the half-width of the ridge contribute to interaction effects. As these parameters are restricted in Fig. 5.4 the interactions between them are limited and thus the main effect explains more of the output uncertainty. For the precipitation output (Fig. 5.4), a similar behavior arises: the overall main effect is increased and the interactions are decreased. The main contributors to the overall main effect are the CCN concentration with values up to 63% followed by the IN concentration (up to 27%) and wind shear (up to 11%).

Our results indicate that looking at the forecast errors the uncertainty of the cloud variables is mainly controlled by the trigger characteristics ΔT and the radius in the warm bubble and the cold pool setup. In contrast, the wind shear has the largest main effect regarding the cloud variables in the orography setup. For the precipitation, the CCN concentration and the IN concentration affect the output uncertainty remarkably in all three setups. As orography is also included in operational forecasts the result of the orography setup presumably reflects the sensitivities of an operational forecast better than those of the warm bubble and the cold pool. Thus, improving the forecast of the wind profile may lead to a clear reduction of the output uncertainty of cloud variables and precipitation.

5.2. Size distribution of surface hail

First, the mean size distributions of a large ensemble of randomly generated emulator predictions are inspected for all three convection triggers and afterwards the response of the size distribution of surface hail to different environmental conditions is analyzed. In this first part, the emulators are used to predict the size distributions at given diameters for a set of 1000 randomly generated combinations of the input parameters which cover the whole parameter space. Besides the temporal and spatial mean of the size distribution, emulators have been constructed predicting the hail diameter and number concentration of the maximum at two, four and six hours after starting the simulation. These are used to include the temporal evolution in the analysis. Fig. 5.6 shows the 1000 size distributions and their mean as well as the mean locations of the maximum at the given time period into the simulations.

(a) warm bubble

(b) cold pool

(c) orography

(d) mean distribution for all triggers
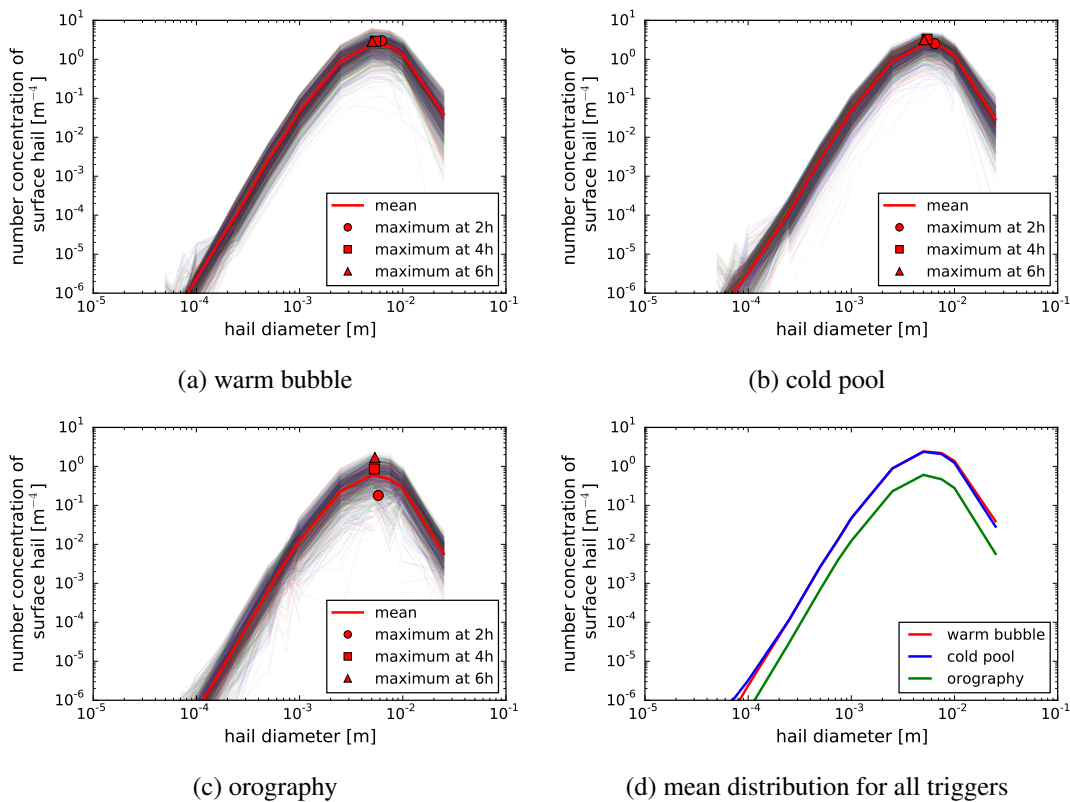
Fig. 5.6.: Size distributions of surface hail of 1000 randomly generated simulations for the warm bubble setup, the cold pool setup and the orography setup. The bold red line denotes the sample mean and the markers stand for the mean position of the maximum of the distribution after two hours, four hours and six hours into the simulation.

For the warm bubble setup (Fig. 5.6a), the ensemble of 1000 simulations has a moderate spread which is quite homogeneous across the considered diameters. The highest number concentration of about $2\,\mathrm{m}^{-4}$ is reached at a hail diameter of 5 mm. However, the location of the maximum varies in time. After two hours of simulation time, the maximum number concentration is approximately the same as for the mean

distribution but it is shifted towards larger diameters. As the simulation proceeds, the number concentration stays constant while the hail diameter decreases. This leads to the conclusion that the larger hailstones fall to the ground while the smaller sizes are left in the cloud later in the simulation. Fig. 5.6b reveals that for the cold pool setup the spread of the distributions is similar to that of the warm bubble setup. In addition, the maximum value of the number concentration is close to that of the warm bubble setup as it can be seen from Fig. 5.6d. The temporal evolution reveals that early in the simulation larger hailstones develop which are then replaced by more and smaller hailstones in the course of the simulation. The size distributions of the orography setup are rather wide spread around the maximum (Fig. 5.6c). The maximum is located at a diameter of 5 mm and at a number concentration of about 0.6 m^{-4}. Thus, the amount of surface hail is smaller in the orography setup which is also depicted in Fig. 5.6d. As the domain mean is shown in Fig. 5.6, the lower amount of in-cloud hailstones can also be partly attributed to a smaller number of cloudy grid points in the orography setup. After two hours of simulation time, the maximum is located at larger diameters but lower number concentrations than the maximum of the mean. But after four and six hours the position of the maximum moves to smaller diameters and higher number concentrations. Hence, the hailstones transform from few and being large to more and being smaller in the orography setup.

Summarizing, it is found that the mean size distribution of surface hail does not differ prominently between the three trigger mechanisms, except for lower number concentrations in the orography setup. Although the shift of the size distribution in the temporal evolution is small, it is systematic for all trigger mechanisms as few large hailstones are replaced by more smaller hailstones during the simulation. However, in the warm bubble setup and the cold pool setup the maximum rather shifts from larger to smaller hailstones whereas in the orography setup the change in the number concentration is larger than the change in the diameter.

The focus of the following part is on the behavior of the size distribution of hail in different environmental regimes. Therefore, each of the uncertain input parameters is assigned two discrete values representing the regimes of the parameter ranges with lower values and higher values, respectively. The two regimes are denoted by "-" and "+". The values were chosen such that a reasonable difference occurs without the necessity of using the full parameter ranges and such that there is always a reasonable amount of wind shear. The chosen values are given in Tab. 5.2.

For each setup and for all 64 possible combinations of these parameters, emulators are used to simulate the size distribution of hail. The emulators predict the number concentration at given particle diameters. Fig. 5.7 shows the mean size distribution in the updraft region at a height of 5000 m where the vertical wind velocity exceeds 20 m s^{-1} for the warm bubble setup. Each of the lines denotes the result for one of the 64 environmental regimes.

Tab. 5.2.: Input values representing both lower and higher regimes of the parameter ranges which are used to analyze the size distribution of hail.

input	lower value (-)	higher value (+)	units
CCN concentration	500	3000	cm^{-3}
IN concentration	0.1	10	scaling factor
wind shear (F_{shear})	0.5	1.0	scaling factor
potential temperature θ_0	298	302	K
temperature perturbation ΔT (WB)	2	5	K
temperature perturbation ΔT (CP)	-10	-6	K
height of ridge (Oro)	2000	5000	m
radius of warm bubble R_{hor}	7	13	km
radius of cold pool R_{hor}	14	26	km
halfwidth of ridge (Oro)	14	41	km
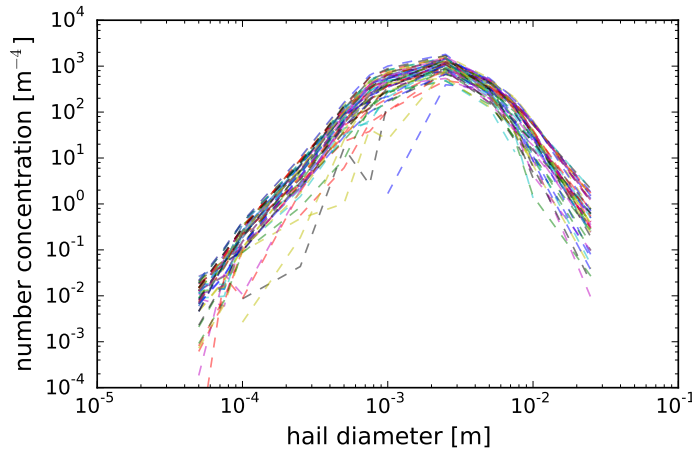
Fig. 5.7.: Size distributions of hail in the updraft area at $z = 5000$ m where the vertical velocity is larger than $20\,\mathrm{ms}^{-1}$. Each line represents the distribution in one of the 64 different environmental conditions. The convection is triggered by a warm bubble.

In all environmental conditions the highest amount of hail is found at a size of $D = 2.5$ mm where the number concentration adds up to $\mathcal{O}(10^3)\,\mathrm{m}^{-4}$. Only minor differences appear and the distributions are rather similar. Thus, it can be assumed that the in-cloud processes determining the hail size are mostly independent on the ambient conditions outside of the cloud. The findings are the same for both the cold pool setup and the orography setup and the plots are not shown separately. However, when looking at the distribution of surface hail differences arise between the trigger mechanisms. Fig. 5.8a shows the mean

size distributions of surface hail for the warm bubble setup where the shading denotes the areas in which the surface hail size distributions are found for the environmental conditions specified by the legends.

(a) size distribution (WB)

(b) main effect (WB)

(c) size distribution (CP)

(d) main effect (CP)

(e) size distribution (Oro)

(f) main effect (Oro)
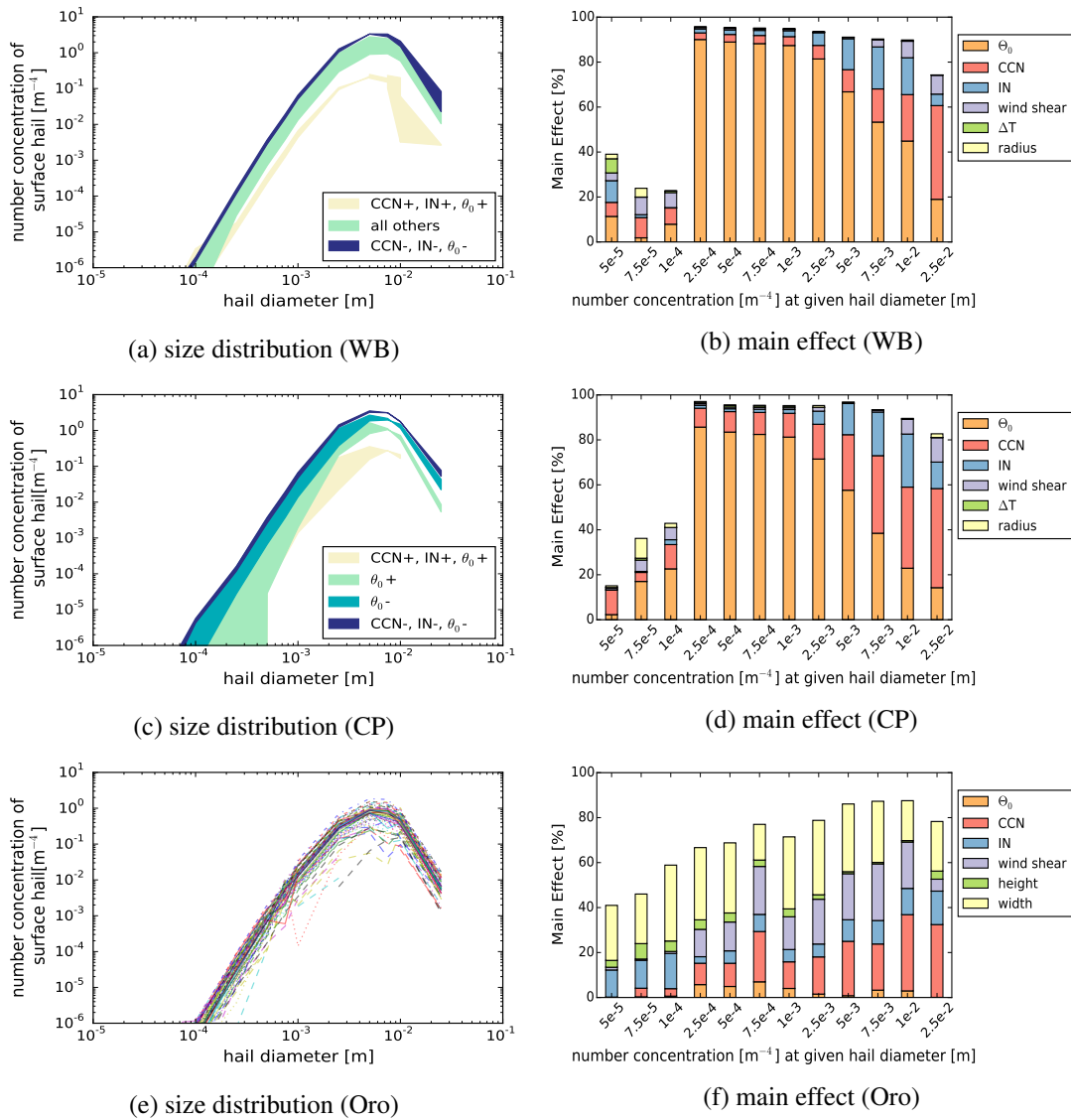
Fig. 5.8.: Left: Size distributions of hail at $z = 0$ m for all trigger mechanisms. The shading in (a) and (c) illustrates regimes of the size distributions controlled by CCN and IN concentrations and θ_0. Each line in (e) represents the distribution in one of the 64 environmental conditions. Right: Bar plots of the main effect for the mean size distribution of surface hail for all trigger mechanisms using the whole parameter range.

The maximum of the size distribution of surface hail is located at a diameter of 5 mm and an amount in the order of $\mathcal{O}(10)$ m^{-4}. The size distributions can be subjectively divided into three clusters. By analyzing the input combinations of each cluster three governing input parameters can be identified: the CCN concentration, the IN concentration and the potential temperature θ_0. If the values of CCN concentration, IN concentration and θ_0 represent the higher values, the least amount of hail is produced. Conversely, the largest amount of hail is produced when the CCN concentration, the IN concentration

and θ_0 take the lowest values. Medium amounts of hail are produced for other combinations of the governing parameters. To summarize, the least amount of hail at the ground is found for conditions with a high number of CCN and IN and rather warm temperatures with high CAPE, whereas few CCN and IN and colder conditions produce more hail when a warm bubble is used as trigger mechanism.

The parameter main effects for the size distribution shown in Fig. 5.8b confirm the result found above. Mostly θ_0 contributes to the output uncertainty of the number concentrations at the given diameters. In the medium size range with diameters between $2.5 \cdot 10^{-4}$ m and $2.5 \cdot 10^{-3}$ m the potential temperature θ_0 is responsible for more than 80% of the output uncertainty. On the one hand, the main effect of θ_0 decreases to roughly 20% towards larger diameters and on the other hand the sum of the uncertainty contributions from the CCN and IN concentrations increases to a total of 47%. Contributions to the overall main effect of other input parameters are only of minor importance and thus the three parameters causing the largest uncertainty in the size distribution are the potential temperature θ_0 and the CCN concentration and the IN concentration.

When using a cold pool as trigger mechanism, the analysis of the size distribution yields similar results with some differences. As it can be seen from Fig. 5.8c, the maximum of the distribution is also found at a diameter of 5 mm. However, four groups of size distributions can be distinguished. Identical to the warm bubble setup, a group of simulations identified by high CCN and IN concentrations and high temperatures can be separated towards higher number concentrations. In addition, a group characterized by low CCN and IN concentrations and low temperatures can be separated towards lower number concentrations. Furthermore, the remaining size distributions can be divided into a group with medium high number concentrations related to high potential temperatures and a group with medium low number concentrations related to low potential temperatures. A possible explanation for this can be found in Fig. 5.8d, which shows the main effects for the size distribution of surface hail for the cold pool setup. From a diameter of $1 \cdot 10^{-4}$ m to a diameter of $1 \cdot 10^{-3}$ m over 80% of the uncertainty is dominated by θ_0. From a diameter of $2.5 \cdot 10^{-3}$ m onward the influence of θ_0 gets smaller and the contributions of the CCN and IN concentrations start to grow reaching values of 44% and 24%, respectively. Compared to the warm bubble setup, the absolute difference of the contribution of θ_0 between small and large diameters is increased. Therefore, an enhanced effect on the number concentration is detectable allowing for an additional separation into a θ_0- regime and a θ_0+ regime.

Contrasting results can be found when a mountain ridge is used to trigger convection (Fig. 5.8e and 5.8f). Compared to the warm bubble and cold pool setups, the shape of the distributions is more diverse. Some of them peak at a diameter of 5 mm, whereas others peak at a diameter of 7.5 mm or have similar values at both diameters. A small number of simulations shows size distributions with lower number concentrations. However, these differences are only distinct in the range of the maxima and thus a clear separation into clusters is not possible. The sum of the main effects in each case varies around 70%, which means that more parameter interactions occur in the orography setup as already seen in section 5.1. Several input parameters contribute almost equally to the output uncertainty: the CCN concentration

($\sim 20\%$), the IN concentration ($\sim 10\%$), the wind shear ($\sim 20\%$) and the half width of the mountain ridge ($\sim 20\%$). Furthermore, there are also minor contributions from θ_0 and the height of the ridge. The fact that various input parameters have similarly large contributions to the uncertainty in the size distribution here prevents us from naming a specific key parameter in this case.

To sum this up, the sensitivity of the surface hail distribution to environmental conditions depends on the trigger mechanism. When a warm bubble is used the number concentration is controlled by the CCN and IN concentrations and the potential temperature θ_0 dividing the test ensemble into three regimes. The combination of CCN+, IN+ and θ_0+ yields the lowest number concentration, whereas the highest number concentration is reached for the combination of CCN-, IN- and θ_0-. In the cold pool setup, the ensemble can be separated into four groups with the potential temperature θ_0 being more dominant. This leads to an additional regime. However, in the orography setup, no controlling parameters are identifiable as several parameters interact and determine the size distribution. A possible explanation for the importance of both CCN and IN concentration and also θ_0 is given by the size of the hailstones. Small hailstones do not fall as fast as large hailstones, as the fall speed depends on the mass (Seifert and Beheng, 2006a). Thus they have more time to interact with the surrounding air. Combining this with a high value of θ_0 leads to the conclusion that small hailstones melt or sublimate before they can reach the ground and therefore low number concentrations are found for the input combination of CCN+, IN+ and θ_0+. On the contrary, larger hailstones in less polluted and cooler environments are not completely melted before reaching the ground and a high number concentration is observed.
Overall, a shift of the size distributions towards smaller or lager diameters caused by the changes in the environment is not visible.

5.3. Diabatic heating rates

In this study, the diagnostics of diabatic heating rates are implemented similar to Joos and Wernli (2011). Thus, the total diabatic heating rate is decomposed into contributions of each hydrometeor and their respective impact can be identified. A more detailed description of this method is given in section 4.2. In order to get statistically significant results and to minimize the effect of single extreme events, the emulators are used to generate $10,000$ simulations of the vertical profiles of the heating rates covering the whole parameter space. Subsequently, the mean and the standard deviation of these profiles are calculated which are analyzed in this section. Fig. 5.9 shows the domain mean vertical profiles of the heating rates for the warm bubble setup.

The evaporation of rain causes diabatic cooling up to four kilometers above the ground which leads to a net cooling in the lowest kilometers. Processes producing cloud water, such as the saturation adjustment of the model, warm the atmosphere in the height between 1 km and 9 km with a maximum of about
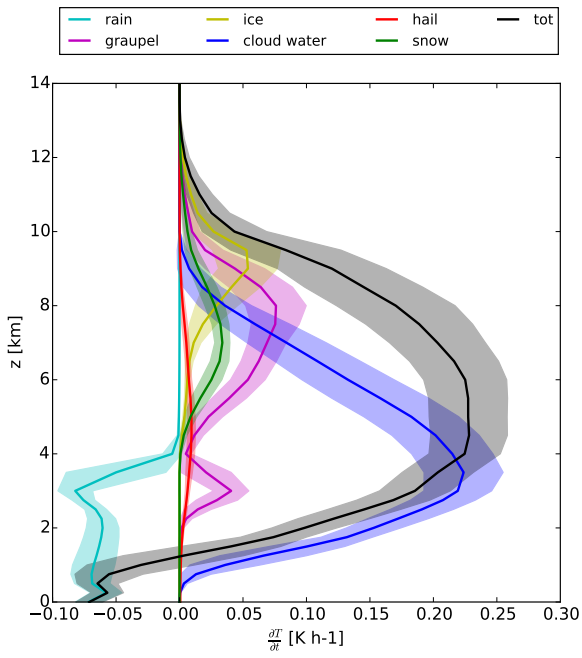
Fig. 5.9.: Vertical profiles of the mean diabatic heating rates by each hydrometeor and the mean total diabatic heating rate for the warm bubble setup. The shaded areas denote the standard deviation.
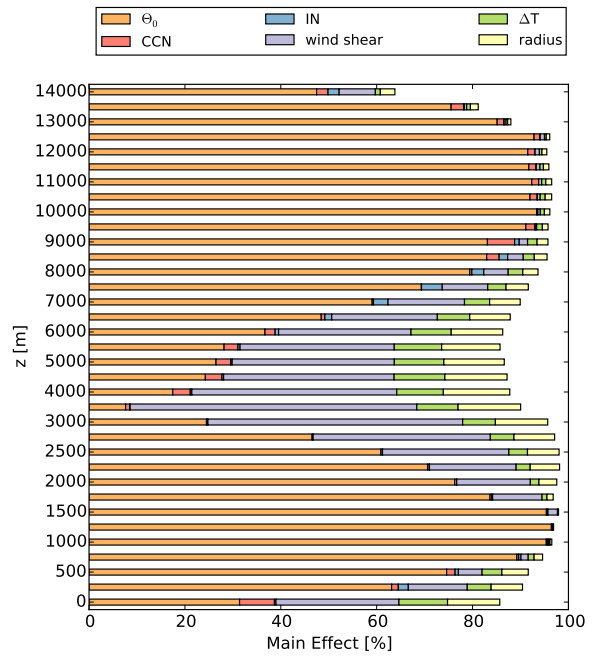
Fig. 5.10.: Bar plot of the main effect for the total diabatic heating rates when a warm bubble is used to trigger convection.

0.22 K h^{-1} at 3.5 km. At altitudes between 6 and 9 km, there are only smaller contributions of 0.08 K h^{-1} and 0.04 K h^{-1} from the graupel and snow processes, respectively. Thus, the net warming rapidly decreases above 8 km. The conversions producing hail do not impact the total heating rates considerably as they peak at 4 km with a maximum heating rate of 0.01 K h^{-1}. The standard deviation approximately scales with the absolute value of the mean heating rates with larger variance for the cloud water and the net rates. Overall, the maximum range of the standard deviation is 0.003 K h^{-1} which suggests some moderate variations but no extreme fluctuations. Fig. 5.10 is a stacked bar plot of the main effects of the vertical profile of the total heating rate. Similar to section 5.1, the potential temperature θ_0 impacts the output uncertainty of the heating rates to a great extent adding up to more than 80%, especially in the below 2000 m and above 7500 m. However, in the mid-levels between 2000 m and 7500 m, the contribution from θ_0 is reduced giving way to contributions from the wind shear, the radius of the initial bubble and also its temperature perturbation ΔT. This change of the composition of the overall main effect coincides with the vertical profile of the heating rate of cloud water (Fig. 5.9) which is the dominant contributor to the total heating rate between 2000 m and 7000 m. Hence, it can be assumed that the shape of the initial bubble and its deformation due to the wind shear influence the volume in which cloud droplets are produced and thus affect the heating rates. In general, the radius and the wind shear have larger impact on the vertical profile of the total heating rate than the potential temperature as θ_0 shows large contributions

only at those height levels where the heating rates are close to zero.

Moreover, the results of the simulations where a cold pool triggers the convection are analyzed. Fig. 5.11 depicts the mean vertical heating rates for each particle class and their standard deviations.
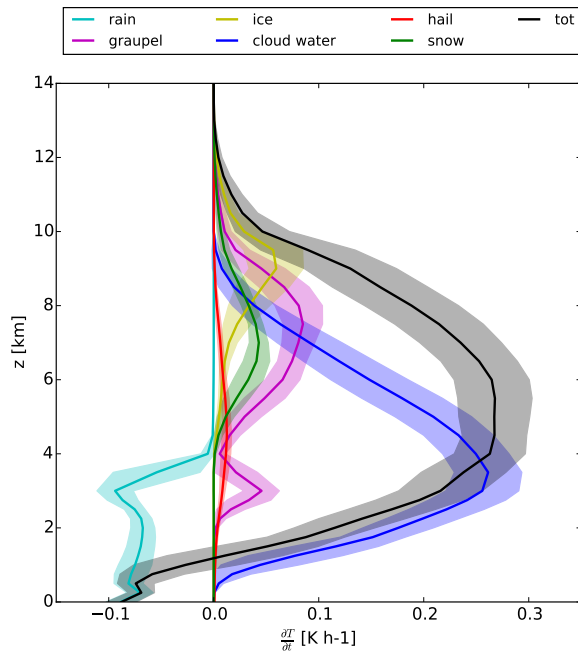
Fig. 5.11.: Vertical profiles of the mean diabatic heating rates by each hydrometeor and the mean total diabatic heating rate for the cold pool setup. The shaded areas denote the standard deviation.
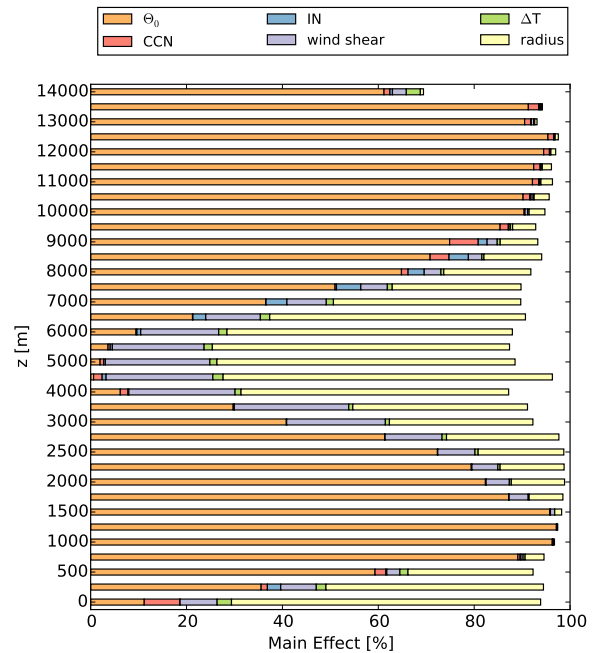
Fig. 5.12.: Bar plot of the main effect for the total diabatic heating rates when a cold pool is used to trigger convection.

Similar to Fig. 5.9, the total heating rates are negative in the lowermost 1000 m of the atmosphere which leads to diabatic cooling near the ground. Above 1 km altitude the total heating rate rapidly increases until it reaches a plateau with a maximum of $0.27 \, \text{K} \, \text{h}^{-1}$ at a height of 4 km. Between 7 km and 10 km the heating rate decreases to values below $0.05 \, \text{K} \, \text{h}^{-1}$. The described structure of the total heating rate is mainly determined by contributions from rain, cloud water and graupel. The evaporation of rain causes the cooling near the ground and the condensation of cloud droplets affects the positive heating rates in the lower and middle troposphere. In the upper troposphere the formation of graupel adds $0.08 \, \text{K} \, \text{h}^{-1}$ to the total heating rate. Furthermore, the height dependence of the remaining ice categories is visible through their contributions. The heating rate due to ice has a maximum of $0.06 \, \text{K} \, \text{h}^{-1}$ at a height of 9 km and the maximum of $0.04 \, \text{K} \, \text{h}^{-1}$ of the heating rate due to snow is located at $z = 7$ km. The production of hail adds to the heating rate in heights between 2 km and 8 km where the maximum of

0.01 K h^{-1} is found at $z = 4 \text{ km}$. Similar to Fig. 5.9, the highest variance is found in the plateau region. In general, the shaded areas are smaller in the cold pool setup which shows that there are less variations of the heating rates than in the warm bubble setup. Fig. 5.12 is a stacked bar plot of the main effects for the total heating rate which reveals the sources of the standard deviation in Fig. 5.11. As seen in Fig. 5.10 for the warm bubble setup, the potential temperature θ_0 has a main effect of more than 80% for the total heating rate in the lower and upper troposphere. In the middle troposphere between 2000 m and 7500 m, the main effect of the radius of the cold pool is increased and decreases with a maximum of 65% at a height of 4000 m. At these altitudes, the wind shear contributes approximately $15 - 20\%$ to the overall main effect and the impact of the potential temperature is diminished. This change in the composition is co-located with the maximum regions of the heating due to the production of cloud water and the total heating rate. Analogous to the warm bubble setup, the conclusion can be drawn that mainly the radius of the initial cold pool and to some extent the wind shear control the location and volume in which cloud water is generated and which is therefore responsible for the strong contribution to the heating rate.

Finally, Fig. 5.13 illustrates the domain mean vertical profiles of the total heating rates and the heating rates per hydrometeor class for the orography setup.
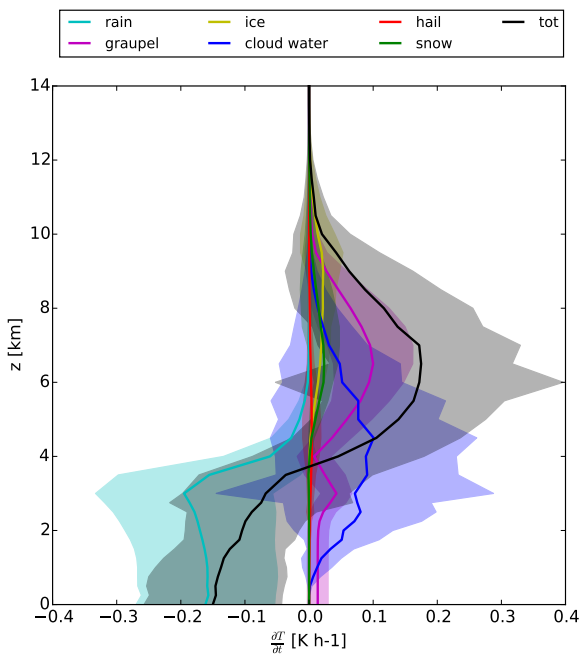
Fig. 5.13.: Vertical profiles of the mean diabatic heating rates by each hydrometeor and the mean total diabatic heating rate for the orography setup. The shaded areas denote the standard deviation.
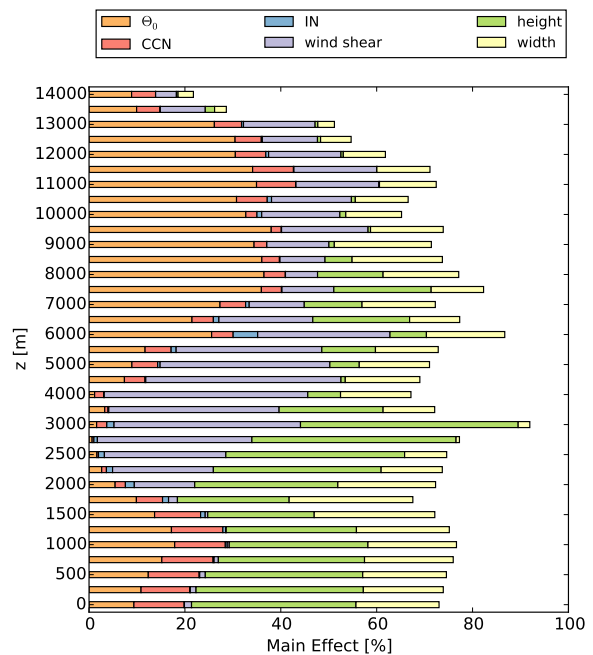
Fig. 5.14.: Bar plot of the main effect for the total diabatic heating rates when a mountain ridge is used to trigger convection.

The diabatic cooling in the lowest 4 km above the ground due to the evaporation of rain reaches values of -0.2 K h^{-1} and is thus stronger than in the warm bubble and cold pool setups. Consequently, the transition between net cooling and heating is raised to a height of about 3500 m. The total heating rate reaches its maximum of 0.17 K h^{-1} at $z = 6500$ m. The generation of cloud water adds to the heating between $z = 1500$ m and $z = 7000$ m with maximum values of 0.1 K h^{-1} and also the generation of graupel contributes with values up to 0.09 K h^{-1} in the upper troposphere. Smaller contributions of snow and ice are found at heights of 7500 m and 9000 m, respectively. Contributions to the total heating rate from the formation of hail can be neglected. Although the general structure of cooling near the ground and heating above is the same for all three trigger mechanisms, the vertically integrated rates of cooling and heating are rather balanced in the orography setup whereas the heating of the atmosphere is clearly dominant for the thermal triggers. Another difference are the large standard deviations in the orography setup. The standard deviations reach values even higher than the absolute value of the mean heating rates. For instance, the standard deviation of the cloud water amounts to 0.16 K h^{-1} for a mean of 0.10 K h^{-1} and the standard deviation of the total heating rate adds up to 0.22 K h^{-1} for a mean of 0.17 K h^{-1}. Hence, the heating rates are more sensitive to the input parameters in the orography setup than in the warm bubble or cold pool setup. The stacked bar plot of the main effect for the total heating rate is shown in Fig. 5.14. At lower altitudes, the height and the width of the mountain ridge have the largest main effects which sum up to contributions of 50%. The contribution from the potential temperature θ_0 slowly increases with height such that at $z = 8000$ m the main effect of the potential temperature (36%) equals the combined contribution from the other parameters. Above this height, the potential temperature and the wind shear are the principal contributors to the output uncertainty. In contrast to the simulations with thermal triggers, the strong impact of the heating by cloud water condensation does not cause a significant change of the main effect of the total diabatic heating rate in Fig. 5.14. However, this plot can be divided into two regimes. On the one hand, the lower altitudes up to 3500 m where the height and the width of the ridge impact the main effect the most and on the other hand the higher altitudes where the potential temperature has the largest main effect. The separation is related to the transition from cooling to heating of the total heating rate which also happens at heights between 3500 m and 4000 m. This suggests that the input parameters describing conditions near the ground, such as the properties of the ridge, mainly affect the heating rate in the lower troposphere. Furthermore, there are more interaction effects in the orography setup as the total main effect reaches only about 80%.

In order to analyze the structure of the heating rates and the differences between the triggers of deep convection in more detail, the temporal evolution of the phase transition rates is inspected. These rates are the basis for the calculation of the heating rates. Thereby it is possible to determine the relative contribution of each process and also which processes already appear in early stages of the simulation. Similar to the heating rates, the emulators are used to predict the domain mean of the phase transition rates for 10,000 simulations covering the whole parameter uncertainty space. The mean of these emu-

lator predictions for the warm bubble setup can be seen in Fig. 5.15a for the absolute rates and in Fig. 5.15b for normalized rates scaled with the respective maximum value.

(a) absolute values   (b) normalized
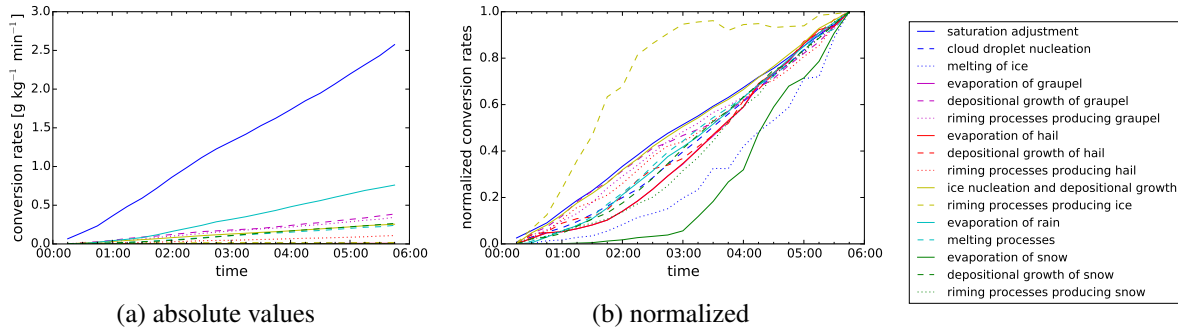
Fig. 5.15.: Domain mean phase transition rates when the convection is triggered by a warm bubble. (a) Absolute values of the rates. (b) Normalized rates scaled with each maximum value.

It is obvious from Fig. 5.15a that the saturation adjustment is the most prominent phase transition rate reaching values of more than $2.5 \, \mathrm{g \, kg^{-1} \, min^{-1}}$. From the start of the simulation onward, more cloud water is produced by saturation adjustment than any other hydrometeor by other processes including phase transitions. This explains the large contribution of the cloud water to the total heating rate compared to the other particle classes. The evaporation of rain reaches absolute values of approximately $0.7 \, \mathrm{g \, kg^{-1} \, min^{-1}}$ and also the melting processes add to the cooling rate connected to rain ($0.3 \, \mathrm{g \, kg^{-1} \, min^{-1}}$). Other processes related to a cooling of the atmosphere such as the evaporation of graupel or hail show no significant conversion rates. Regarding the processes leading to a warming of the atmosphere, the depositional growth and the growth of graupel by riming have large conversion rates of about $0.5 \, \mathrm{g \, kg^{-1} \, min^{-1}}$ at the end of the simulation. These two rates added together drive the substantial heating rate of graupel in the upper troposphere. The depositional growth of snow and the nucleation and depositional growth of ice have a small conversion rate of $0.3 \, \mathrm{g \, kg^{-1} \, min^{-1}}$, whereas the effect of the remaining processes on the total heating rate is negligible. Fig. 5.15b aims at comparing the temporal evolution of the different conversion rates. The riming processes producing ice increase faster than the other processes reaching a plateau between 02:30 h and 04:45 h after the model initialization. Most rates show a linear increase with time as the cloudy area increases. The melting of ice develops rather slowly but accelerates after 03:00 h. Furthermore, the initiation of the evaporation of snow is delayed as an increase of its rate is only visible two hours after the model initialization.

Fig. 5.16 shows the mean and the normalized conversion rates for the simulations where a cold pool is used as trigger mechanism. Also in the cold pool setup, the saturation adjustment is the rate growing fastest which reaches values higher than $2.5 \, \mathrm{g \, kg^{-1} \, min^{-1}}$ after six hours. The evaporation of rain is the largest rate causing cooling of the atmosphere. Moreover, all remaining processes are comparable to the results of the warm bubble simulations. The depositional growth of graupel and the production of

(a) absolute values   (b) normalized
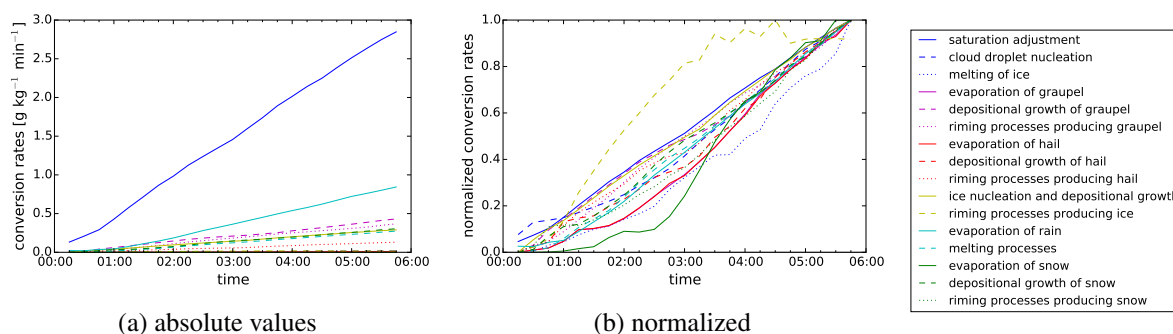
Fig. 5.16.: Domain mean phase transition rates when the convection is triggered by a cold pool. (a) Absolute values of the rates. (b) Normalized rates scaled with each maximum value.

graupel by riming show conversion rates of up to 0.5 g kg^{-1} min^{-1} and 0.4 g kg^{-1} min^{-1}, respectively. Slightly lower rates are found for the depositional growth of snow, nucleation and deposition of ice and melting processes. The remaining processes have conversion rates of less than 0.15 g kg^{-1} min^{-1}. The temporal evolution is illustrated in more detail in Fig. 5.16b which is similar to Fig. 5.15b as well. The phase transition rate rate of the riming processes producing ice develops early in the simulations until it reaches its maximum after four hours of simulation time. Afterwards, the rate is decreasing until the end of the simulation. It takes approximately one hour for the evaporation of snow to evolve but after that the rate strongly increases. The other conversion rates follow a linear trend such that the temporal evolution is roughly the same.

The results for the orography setup are illustrated in Fig. 5.17.

(a) absolute values   (b) normalized
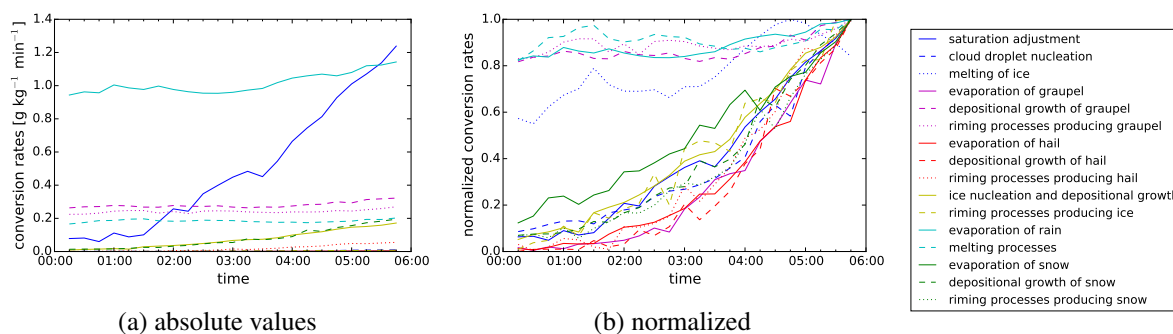
Fig. 5.17.: Domain mean phase transition rates when the convection is triggered by a mountain ridge. (a) Absolute values of the rates. (b) Normalized rates scaled with each maximum value.

As the simulations in the orography setup need a spin up time of five hours to produce deep convection, the phase transition rates do not start from zero in Fig. 5.17, but from an offset of about 1.0 g kg^{-1} min^{-1} for the saturation adjustment and of less than 0.3 g kg^{-1} min^{-1} for the remaining processes . Just as for the warm bubble and the cold pool setups, the saturation adjustment clearly increases during the considered simulation time to values higher than 1.2 g kg^{-1} min^{-1}. However, the evaporation of rain is the

most dominant rate as it already starts at 0.9 g kg^{-1} min^{-1} and increases to 1.1 g kg^{-1} min^{-1} after six hours. The order of the other rates is the same as for the warm bubble setup and the cold pool setup: higher values for the growth of graupel by deposition and riming, followed by the evaporation of rain, deposition of snow and nucleation and deposition of ice. The differences between the results of thermal triggers and those of the mountain ridge are visible in Fig. 5.17b. The early increase of the riming processes producing ice, which was found in Fig. 5.15b and 5.16b, is not present in Fig. 5.17b. Instead, the evaporation of rain and the melting processes but also the growth of graupel by both riming and deposition are established before the other processes. Most of the rates still follow a linear increase, however the slope is not as smooth as for the other triggers.

To sum up, the vertical profiles of the diabatic heating rates are similar for the warm bubble setup and the cold pool setup. In the lowest 1000 m, the atmosphere is cooled due to the evaporation of rain. At higher altitudes, the heating rate increases until it reaches its maximum between 4 km and 6 km and finally decreases above. The heating can mostly be attributed to the production of cloud water in the lower atmosphere and to the production of graupel in the upper troposphere. The standard deviation resulting from 10,000 simulations randomly distributed in the parameter space spans a maximum range of 0.003 Kh^{-1} which suggests moderate variations. Regarding the main effects for the total heating rate, a change in the composition of the stacked bar plots is connected to the heights of maximum heating due to the production of cloud water and thus to the heights of the maximum total heating rate. In these regions, the contributions of the trigger characteristics and the wind shear to the output uncertainty of the total heating rate is enlarged. In the orography setup, the heating rate is negative near the ground as for the warm bubble and cold pool setups. However, the layer of diabatic cooling is thicker and the standard deviations are higher which indicates that there are more variations of the heating rates due to changes in the input parameters than for the thermal triggers. Furthermore, the contributions of the trigger characteristics to uncertainty of the heating rates are highest near the ground and therefore not clearly related to the maximum heating rates. Reasons for the differences can be found in the temporal evolution of the phase transition rates. In the warm bubble and the cold pool setup, the riming processes producing ice develop faster than the other conversion rates whereas in the orography setup this is not visible. Instead graupel and rain processes such as the depositional growth of graupel and the evaporation of rain are already well developed at the beginning of the analysis period because a spin-up time is required in the orography setup to generate sustained convection. Thus, some of the differences between the orography setup and the thermal triggers are caused by the additional spin-up time.

5.4. Sensitivity to CCN concentration

The cloud response to changes in the CCN concentration is a subject of great interest and there are many studies analyzing the impact and consequences of variations of the CCN, e.g. Khain et al. (2011); Morrison (2012); Noppel et al. (2010); Yang et al. (2017). Yet, the results of the above mentioned studies are not uniform and therefore the correlation between changes in the CCN concentration and the precipitation responses is not clearly determined. For example, on the one hand Khain et al. (2011) simulate a hailstorm over south-west Germany for different CCN concentrations and find that an increase of the CCN concentration leads to an increase of the precipitation of hail (Khain et al. (2011), Fig. 4). On the other hand Noppel et al. (2010) analyze the same storm but obtain the opposite result: an increase of the CCN concentration is mainly connected to a decrease of the precipitation of hail (Noppel et al. (2010), Tab. 3). As the emulators require hardly any computational power, they are a convenient tool to run many simulations and investigate the cloud response to variations of the CCN concentration in different environmental conditions. Similar to section 5.2, each input parameter, except for the CCN concentration, is assigned two values representing the lower ranges and the higher ranges of the parameter space. The chosen values are the same as in Tab. 5.2. The parameter range of the CCN concentration is sampled with a set of 10,000 points. In contrast to section 5.2, only five input parameters determine the environmental conditions and therefore 32 different regimes are compared. During the analysis the focus is on the integrated amount of cloud water (TQC), the integrated amount of hail (TQH) and the maximum amount of precipitation by hail to determine the impact on in-cloud variables affecting the amount of precipitating hail. Fig. 5.18 shows the considered output versus the CCN concentration for all 32 regimes and for all trigger mechanisms. The output values are normalized with their respective maximum reached in each regime.

In general, the mean sensitivity of the three output variables to the CCN concentrations behaves similarly for all trigger mechanisms. The cloud water increases whereas both the in-cloud hail and the precipitation of hail decrease with increasing CCN concentration. When a warm bubble is used to trigger convection, the integrated cloud water shows a strong increase for low CCN concentrations which flattens towards higher concentrations. The integrated hail content decreases to approximately 70% of its maximum value when a polluted atmosphere is prescribed. Both the decrease and the spread are more pronounced for the precipitation of hail than for the integrated hail content. On average, the precipitation of hail is reduced to less than 40% when the CCN concentration is increased, while in some other regimes the reduction is even stronger such that no hail is found at the ground. The cold pool setup is most robust to changes of the environmental conditions. The cloud water increases almost linearly from 60% to 100% and the hail content decreases to 70% for CCN concentrations between 100 and 4000 cm^{-3}. Both variables show a maximum spread of about 20%. The precipitation of hail is reduced to values between 40% of the original value and no hail at all. Although the spread is higher for precipitating hail, all atmospheric regimes exhibit the same sign of the change. In the orography setup, large deviations from

(a) warm bubble

(b) cold pool
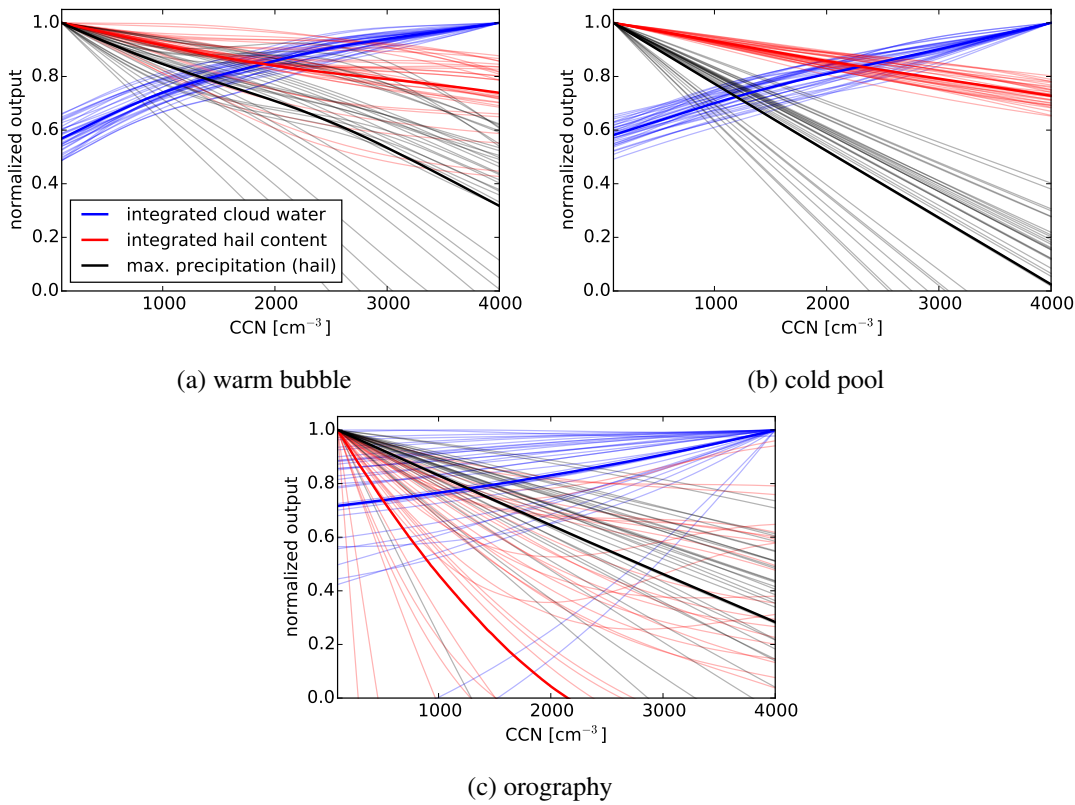
(c) orography

Fig. 5.18.: Sensitivity of mean integrated cloud water, mean integrated hail and precipitation by hail to variations in the CCN concentrations for (a) the warm bubble setup, (b) the cold pool setup, (c) the orography setup. Thin lines represent the results for 32 different environmental conditions and the bold lines denote the means.

the mean trend are found. Beginning at values around 70% of its maximum, the mean of the integrated cloud water is increasing slowly for low CCN concentrations and strongly for high concentration. But there are also regimes where a sensitivity to CCN is hardly visible. Several variations are possible for the trend of the integrated hail content. First, most of the simulations and thus the mean of all results are rapidly decreasing with increasing CCN concentration such that no more in-cloud hail is present before the maximum CCN concentration is reached. Second, some regimes show a moderate decrease to 50%-80% of the maximum value. Finally, there are few regimes where the integrated hail content first follows the trend of the mean but then stops to decrease around a CCN concentration of 2000 cm^{-3} and even slightly increases towards higher CCN concentrations. In contrast, the results of the precipitation of hail are more uniform with linear decreases reaching the minimum value for the highest CCN concentration. As the decrease of the precipitation of hail is not as rapid as the decrease of the integrated hail content, Fig. 5.18c suggests that it is possible to simulate hail at the ground while there is no in-cloud hail. However, mean values are considered for the in-cloud hail whereas maximum values are analyzed for the hail at the ground and therefore no unrealistic results are found for the orography setup.

Summarizing, it can be seen that the sensitivity to the CCN concentrations varies for each regime of environmental conditions. Especially in the orography setup large variations are possible which reflects the complexity of convection above mountainous terrain (Kirshbaum et al., 2018). Still, the overall trend is the same: the sensitivity to an increased CCN concentration is linked to an increase for the integrated cloud water and to a decrease for the integrated hail content and the maximum precipitation of hail. Thus, the results are robust for different environmental conditions and trigger mechanisms. Further, this means that the discrepancies between the findings of Khain et al. (2011) and Noppel et al. (2010) cannot be explained by different environmental conditions.

6. Emulator Studies for Perturbations of the Microphysics

This chapter contains the results of the study where the impact of the cloud microphysics is analyzed. The CCN and IN concentrations, the fall velocities of rain, graupel and hail, the strength of the ice multiplication and the shape parameter of the cloud droplet size distribution are used as uncertain input parameters. A detailed description of the input parameters is given in section 4.4.1.

6.1. Cloud variables and precipitation

The results of the variance-based sensitivity analysis for perturbations of the microphysics are shown for the cloud variables and precipitation in Fig. 6.1.

A first view reveals that all three trigger mechanisms share common features, however the results of the warm bubble and the cold pool are in better agreement than the orography setup. The overall main effect of the integrated cloud water is controlled by the CCN concentration which contributes about 70% to the output uncertainty. In case of the integrated hail content, the fall velocity of hail and the ice multiplication both explain 29% of the uncertainty for the warm bubble setup and 36% and 33% for the cold pool, respectively. The output uncertainty of the integrated ice content is dominated by interaction effects as the main effect is responsible for only 40% which are mainly attributed to the CCN concentration (15%) and the fall velocity of graupel (19%). The fall velocity of graupel accounts for large shares of the output uncertainty for the integrated contents of graupel (90%), snow (34%) and rain (47%). While there are no further contributions from other parameters for the integrated graupel content, the CCN and IN concentrations contribute 48% and 11%, respectively, to the uncertainty of the snow content. Furthermore, the fall velocity of hail contributes 23% to the uncertainty of the integrated rain content. Compared to the thermal trigger mechanisms, the fall velocity of graupel is more important in the orography setup. It contributes at least 56% to the output uncertainties, except for the integrated ice content where it contributes 38%. In general, only smaller contributions are found from the CCN concentration (10%), the IN concentration (6%) and the ice multiplication (5%) for the uncertainty of the cloud variables in the orography setup.

The negligible contribution from the CCN concentration to the output uncertainty of cloud water in the orography setup stands out as both warm bubble setup and cold pool setup show opposite results. As CCN are particles that favor the formation of cloud droplets, their impact is expected to be largest during the formation of the cloud. However, the initial formation of the clouds over the mountain ridge is not

(a) warm bubble

(b) cold pool
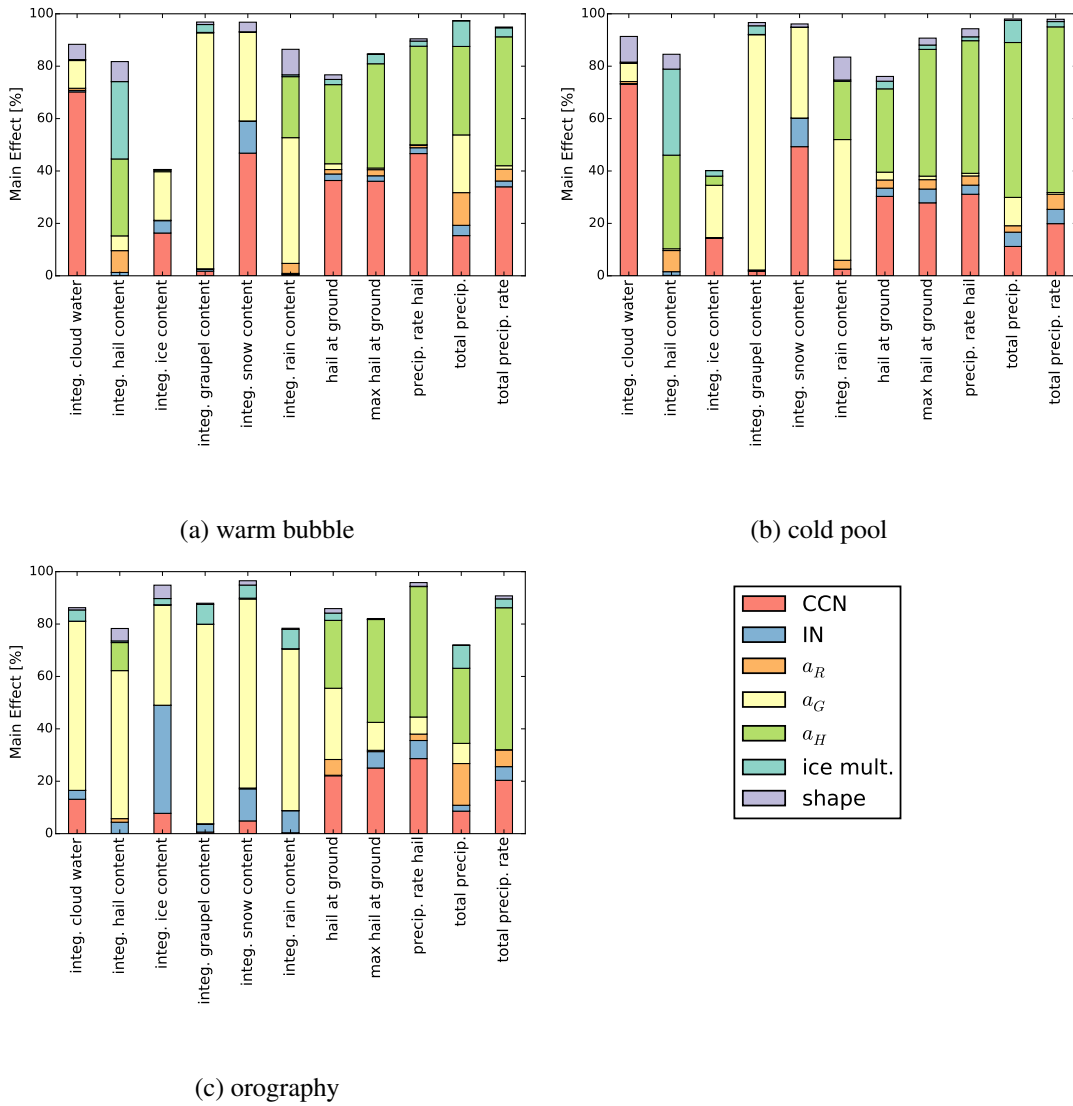
(c) orography

Fig. 6.1.: Bar plot of the main effect for integrated cloud variables and precipitation when (a) a warm bubble, (b) a cold pool, (c) a mountain ridge is used as trigger mechanism.

included in the analysis of the orography setup. The results of an additional sensitivity analysis, where the clouds over the ridge are included, can be found in Fig. 6.2.

The contribution from the CCN concentration to the output uncertainty of the integrated cloud water is increased to 64%. This is similar to the value of the warm bubble and cold pool setups, while in the analysis excluding the ridge the contribution was as low as 13%. In general the CCN concentration shows higher contributions compared to Fig. 6.1c. For example, the impact has almost doubled for the total precipitation rate going from 20% to 35%. Thus, it can be confirmed that the uncertainty in the CCN concentration mainly affects the cloud water during the formation of the cloud over the ridge while its impact is reduced further downwind.
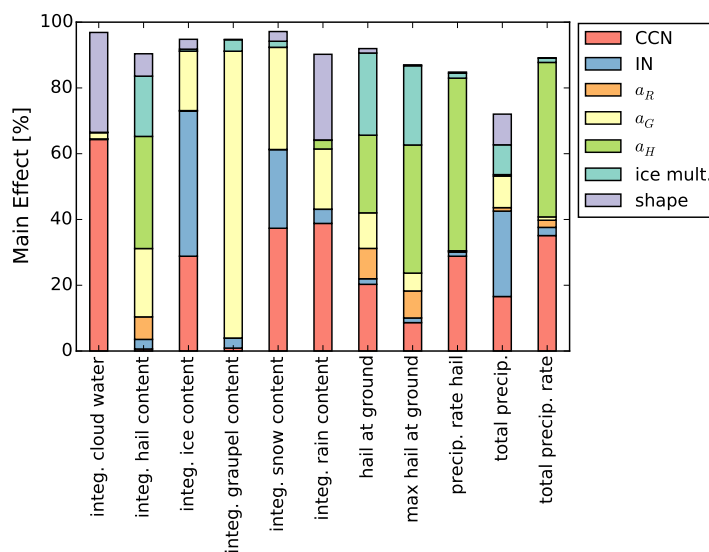
Fig. 6.2.: Bar plot of the main effect for integrated cloud variables and precipitation using a mountain ridge as trigger mechanism when the whole domain is included in the analysis.

When looking at the precipitation variables in Fig. 6.1, a dominance of the CCN concentration and the fall velocity of hail is visible in all setups. In the warm bubble setup, the contribution from the CCN concentration varies between 15% for the total precipitation and 47% for the precipitation rate of hail. In the cold pool setup, the CCN concentration adds between 11% and 31% and in the orography setup between 8% and 28%. The largest contributions from the fall velocity of hail are found in the cold pool setup where it varies between 32% for the mean precipitation of hail and 63% for the total precipitation rate. In the warm bubble setup, the contributions are between 30% and 49% and in the orography setup between 26% and 54%. The remaining parameters contribute to the uncertainties in all setups as well, however their contributions are small compared to those mentioned above.

Summarizing, the results of the cloud variables and the precipitation variables differ. On the one hand, various contributors are found for the cloud variables. So in the warm bubble and cold pool setups, mainly the CCN concentration, the fall velocity of graupel and the fall velocity of hail contribute to the output uncertainty. In the orography setup, these are the IN concentration and the fall velocity of graupel. However, contributions of the CCN concentration, especially to the uncertainty of the integrated cloud water, also appears in the orography setup when the clouds directly over the mountain ridge are included in the analysis. Thus, variations of the CCN concentration substantially affect the amount of cloud water during the formation of clouds. On the other hand, the uncertainty of the precipitation variables is controlled by the CCN concentration and the fall velocity of hail for all trigger mechanisms. Accordingly, the fall velocity of rain, the ice multiplication and the shape parameter of the cloud droplet size distribution are only of minor importance. Overall, the amount of interaction effects is comparable for all three setups.

6.2. Size distribution of hail

As described in section 5.2, 1000 size distributions of surface hail are generated by the emulators and are shown in Fig. 6.3 including their respective means.

(a) warm bubble

(b) cold pool

(c) orography

(d) mean of all triggers
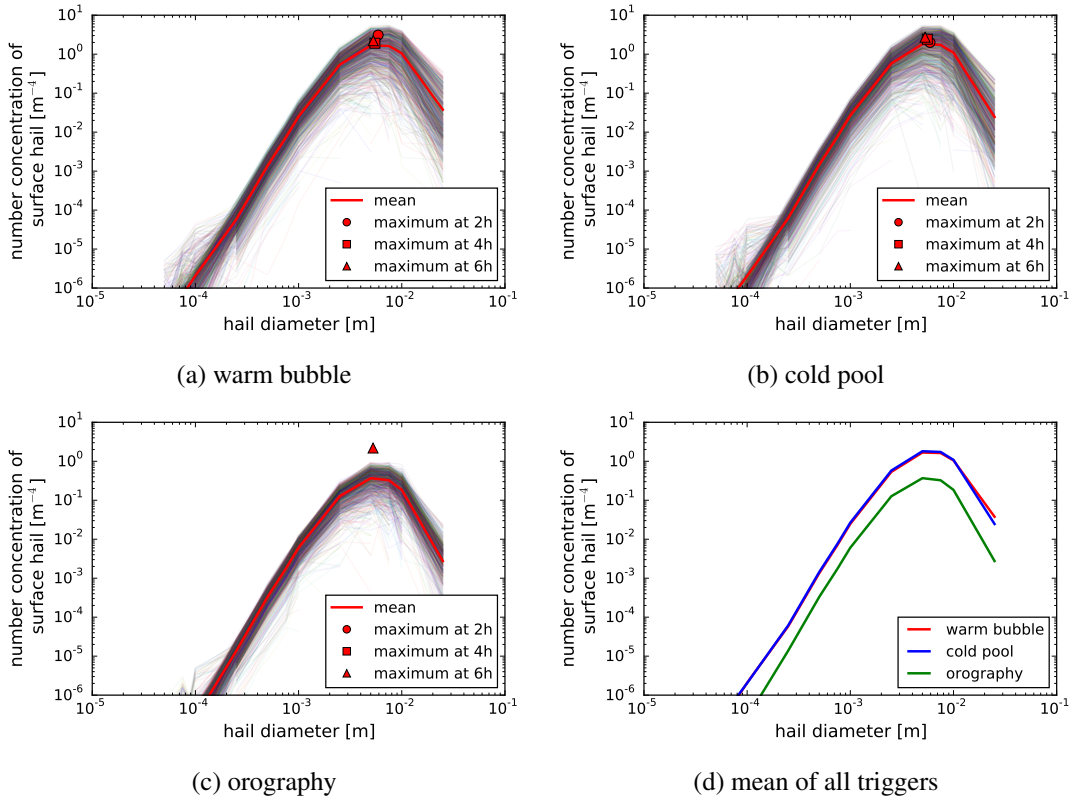
Fig. 6.3.: Size distributions of surface hail of 1000 randomly generated simulations for the warm bubble setup, the cold pool setup and the orography setup. The bold red line denotes the sample mean and the markers stand for the mean position of the maximum of the distribution after two hours, four hours and six hours into the simulation.

In all three setups (Fig. 6.3a - 6.3c), the spread between the different distributions is rather large varying two orders of magnitude. This is especially visible for diameters above 2 mm, while below that threshold the distributions follow the mean distribution. Changes of the maximum of the distributions are only minor during the temporal evolution as the markers depicting the maximum after two, four and six hours of the simulations are close to each other.

In the warm bubble setup (Fig. 6.3a), the highest number concentration of $2\,\mathrm{m}^{-4}$ is found at diameters between 5 and 7.5 mm for the mean distribution. At the largest considered diameter (2.5 cm) the number concentration of surface hail is approximately $4 \cdot 10^{-2}\,\mathrm{m}^{-4}$. After two hours, the maximum is located at a diameter of 6 mm and a number concentration of $3\,\mathrm{m}^{-4}$ but as time evolves it shifts towards smaller diameters and number concentrations ($2\,\mathrm{m}^{-4}$ at 5 mm after 6 h of simulation).

In the cold pool setup (Fig. 6.3b), the maximum of the mean distribution is located similar to that of the warm bubble setup. But for large diameters of the hailstones a concentration of only $2 \cdot 10^{-2}$ m^{-4} is found. The location of the mean of the warm bubble and cold pool setup is illustrated in Fig. 6.3d. First, both lines are almost identical up to the maximum number concentration, but then the cold pool setup shows a more pronounced decrease leading to fewer large hailstones than in the warm bubble setup. During the simulation the maximum of the mean distribution moves from a diameter of 6 mm and a number concentration of 2 m^{-4} at two hours after the initialization to a diameter of 5 mm and a concentration of 3 m^{-4} at six hours after the start of the simulation. Thus, the diameter of the hailstones gets smaller, but at the same time the number concentration increases producing more small hailstones.

In the orography setup (Fig. 6.3c), the diameter is slightly smaller and there are less hailstones as the maximum of the mean distribution is located at a diameter of 5 mm and a number concentration of 0.4 m^{-4}. Additionally, the number concentration of large hailstones is below $3 \cdot 10^{-3}$ m^{-4}. Fig. 6.3d confirms that there is less precipitating hail in the orography setup as its mean distribution lies well below the distributions of the thermal triggers for all considered diameters. Moreover, surface hail is present in the orography setup only after four hours of simulation time. Thus, an analysis of the temporal evolution is not possible.

Summarizing, changes in the microphysics mainly affect the number concentration of the hail size distribution leading to large spreads in the randomly generated sets of size distributions. However, the mean distributions are almost identical for the warm bubble and cold pool setups, whereas in the orography setup less hail is observed. Regarding the temporal evolution, both the warm bubble and the cold pool setup show a decrease of the hail size with time. Further, a small decrease of the number concentration appears for the warm bubble setup but an increase appears for the cold pool setup as time evolves.

As described in section 5.2, the following part focuses on the analysis of the size distributions for different compositions of the microphysical properties. For each of the seven input parameters two discrete values are assigned representing both lower and higher values of the parameter range which are given in Tab. 6.1. So combining all of these parameter values leads to a total of 128 different states of the microphysical conditions for which the size distributions of surface hail are evaluated (Fig. 6.4).

Fig. 6.4a and 6.4c indicate that the 128 size distributions of surface hail obtained for the warm bubble and cold pool setups can be divided into three groups differing in the number concentration. The group with the lowest number concentrations is characterized by a low value of the fall velocity of hail. The maxima of these distributions are found at a diameter of 5 mm and at number concentrations of up to 0.6 m^{-4}. In contrast, the group having the largest number concentrations requires a high value of the fall velocity of hail and the maxima are located at diameters between 5 and 7.5 mm and concentrations between 2.5 and 6 m^{-4}. There is a third group in-between the two aforementioned groups containing both low and high values for the fall velocity of hail. This can be seen as transition zone where distributions

Tab. 6.1.: Input values representing both lower and higher values of the parameter ranges which are used to analyze the size distribution of hail

input	lower value (-)	higher value (+)	units
CCN concentration	500	3000	cm^{-3}
IN concentration	0.1	10	scaling factor
fall velocity of rain (a_R)	0.5	1.5	scaling factor
fall velocity of graupel (a_G)	0.5	1.5	scaling factor
fall velocity of hail (a_H)	0.8	1.2	scaling factor
ice multiplication	$0.7 \cdot 10^8$	$6.3 \cdot 10^8$	kg^{-1}
shape parameter	2	6	-

(a) size distribution (WB)

(b) main effect (WB)

(c) size distribution (CP)
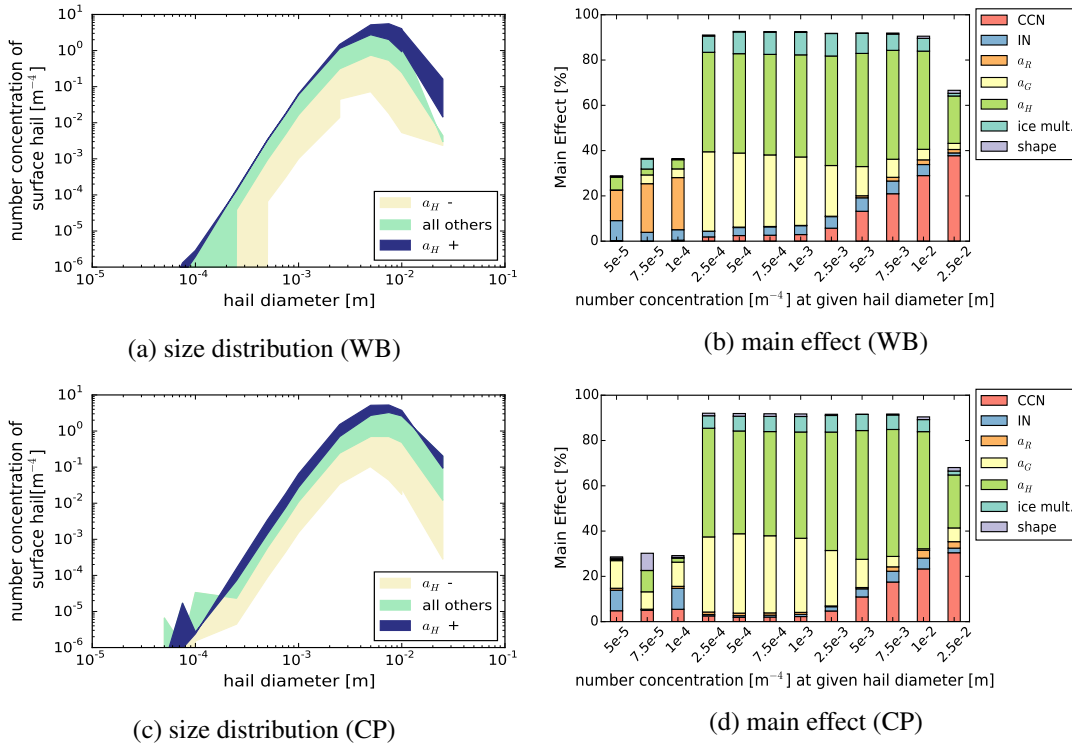
(d) main effect (CP)

Fig. 6.4.: Left: Size distributions of hail at $z = 0$ m for the warm bubble and cold pool setups. The shading in a) and c) illustrates regimes of the size distributions controlled by the fall velocity of hail. Right: Bar plots of the main effect for the mean size distribution of surface hail using the whole parameter range.

with a low fall velocity are found that have larger number concentrations than distributions with a high fall velocity of hail. The controlling parameter of the size distribution a_H is also found to be the main contributor to the output uncertainties of the size distribution in Fig. 6.4b and Fig. 6.4d. It contributes up to 50% to the uncertainty in the warm bubble setup and up to 57% in the cold pool setup. Only at

the largest considered diameter of 2.5 cm the impact of a_H is reduced to about 22% due to an increasing contribution from the CCN concentration.

As it can be seen from Fig. 6.5a, the size distributions of surface hail can also be divided into three groups in the orography setup.

(a) size distribution (Oro)
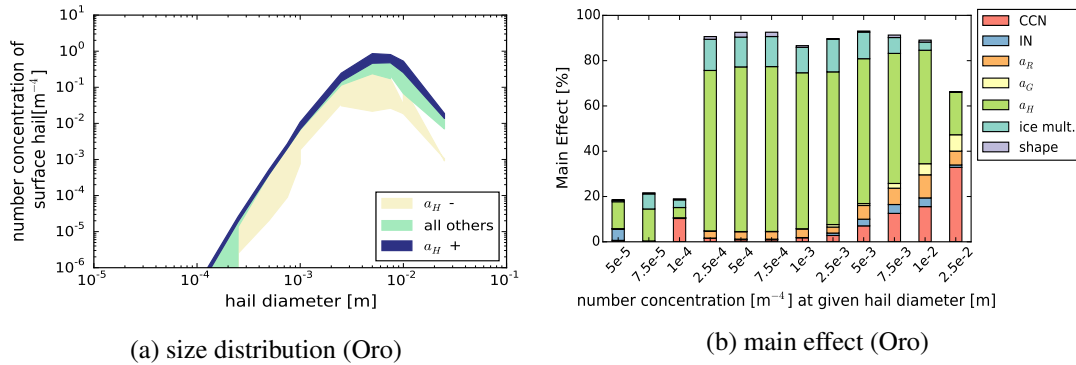
(b) main effect (Oro)

Fig. 6.5.: Left: Size distributions of hail at $z = 0$ m for the orography setup. The shading in a) illustrates regimes of the size distributions controlled by the fall velocity of hail. Right: Bar plot of the main effect for the mean size distribution of surface hail using the whole parameter range.

Similar to the warm bubble and cold pool setups the number concentration is controlled by the fall velocity of hail. Low values of a_H induce low number concentrations and high values of a_H induce high number concentrations with a transition zone in-between as third cluster. In the orography setup, less hail reaches the ground so that the cluster with least hail shows maximum number concentrations between 0.02 and 0.2 m^{-4}. The cluster with most hail has concentrations between 0.4 and 0.9 m^{-4}. Fig. 6.5b confirms the importance of a_H as it contributes up to 73% to the output uncertainty of the size distribution. However, the impact decreases towards larger diameters where the CCN concentration shows increasing contributions (up to 33%).

In all three setups the parameter identified as controlling parameter of the size distribution of surface hail is the fall velocity of hail. As already mentioned in section 5.2, a possible explanation for these dependencies are the size of the hailstones and the associated fall speeds. While the environmental conditions were perturbed, CCN and IN were the input parameters controlling the size and thus the fall speed of the hailstones. In this setup, where the microphysics are perturbed, the fall velocity of hail is an independent parameter. Therefore, input parameters that impact the fall velocity indirectly, such as the CCN and IN concentrations, are only of minor importance. However, both results yield the same conclusion: The slower the hail falls, the smaller the number of modeled hailstones at the ground.

6.3. Diabatic heating rates

The mean vertical profiles of $10,000$ emulator predictions of the heating rates (see section 5.3) are illustrated in Fig. 6.6 for the warm bubble setup where the shaded areas denote the standard deviations.
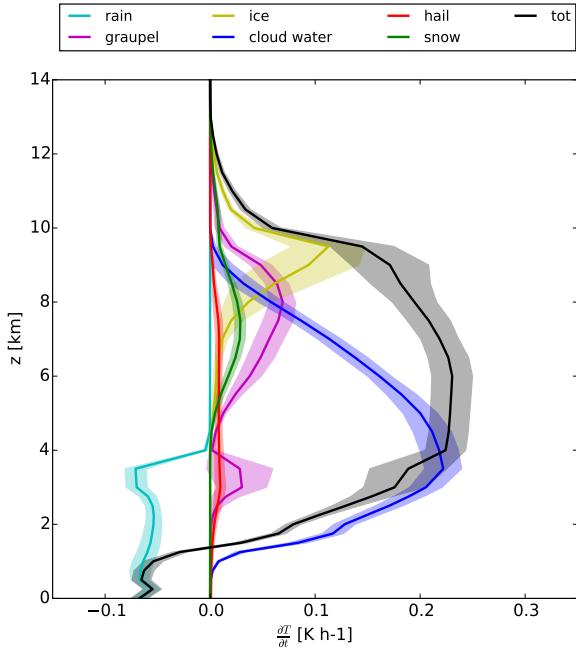
Fig. 6.6.: Vertical profiles of the mean diabatic heating rates by each hydrometeor and the mean total diabatic heating rate for the warm bubble setup. The shaded areas denote the standard deviation.
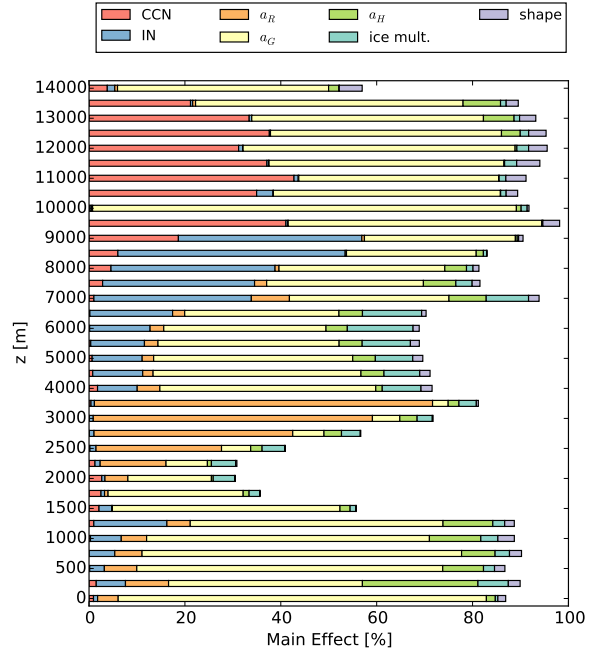
Fig. 6.7.: Bar plot of the main effect for the total diabatic heating rates when a warm bubble is used to trigger convection.

The total heating rate shows a cooling of $0.06\,\mathrm{Kh}^{-1}$ in the lowest $1000\,\mathrm{m}$ above the ground. At heights between of $1250\,\mathrm{m}$ and $1500\,\mathrm{m}$, the cooling changes to a heating of the atmosphere which increases until a height of $6000\,\mathrm{m}$. There, the maximum of $0.23\,\mathrm{Kh}^{-1}$ is reached. Up to $9\,\mathrm{km}$ the rate decreases moderately but a rapid decrease is visible above. The cooling near the ground is caused by the evaporation of rain which is present with rates of $-0.07\,\mathrm{Kh}^{-1}$ up to a height of $4\,\mathrm{km}$. However, the heating due to the formation of cloud water increases quickly above $1000\,\mathrm{m}$ reaching its maximum of $0.22\,\mathrm{Kh}^{-1}$ at $3500\,\mathrm{m}$. Thus, the total heating rate is dominated by the contribution from the cloud water at heights between 1500 and $6000\,\mathrm{m}$. At higher altitudes, heating due to ice phase hydrometeors are prevailing. The formation of hail contributes at heights between $2000\,\mathrm{m}$ and $8000\,\mathrm{m}$, however only small rates of $0.01\,\mathrm{Kh}^{-1}$ are found such that the effect on the total heating rate is insignificant. Below $2\,\mathrm{km}$ and above $10\,\mathrm{km}$, the standard deviation of the total heating rate is almost negligible. Between $2\,\mathrm{km}$ and $10\,\mathrm{km}$, the standard deviation of the total heating rate ranges between 0.02 and $0.04\,\mathrm{Kh}^{-1}$.

Fig. 6.7 shows the main effect representing the sources of uncertainty for the total heating rate. Four layers can be distinguished for which the composition of the overall main effect varies. In the lowest layer up to 2000 m, the fall velocity of graupel a_G is the main contributor. It adds up to 70% to the output uncertainty. Showing contributions of 14% to 70%, the fall velocity of rain is the predominant parameter in the second layer between 2000 m and 4000 m. Between 4000 m and 9000 m, the IN concentration and the fall velocity of graupel primarily add to the output uncertainty. With increasing height also the contribution from the IN concentration increases from about 10% to 47% and at the same time the contribution from a_G decreases from 45% to 27%. In the fourth layer above 9000 m, the CCN concentration contributes up to 43%. The second major parameter at this height is a_G contributing between 42% and 88%. The main effect has values larger than 80% for low and high altitudes, however values between 30% and 70% are found in the middle troposphere. This means that interactions are mainly happening in this region. Moreover, there are relations between the vertical profile of the heating rates and the layers specified above. The second layer with high contributions from a_R coincides with the strong increase of the total heating rate caused by the increase of heating due to cloud water, but also with the cooling due to the evaporation of rain. The layer between 4000 and 9000 m, where the IN concentration and a_G contribute, is connected to the heights of the maximum total heating rate. Furthermore, the ice phase hydrometeors have the largest heating rates at these heights which explains the effect of the IN concentration on the uncertainty.

Fig. 6.8 and 6.9 show the vertical profiles and the main effect of the heating rates for the cold pool setup. The vertical profiles of the heating rates in the cold pool setup are quite similar to those of the warm bubble setup. Cooling of about -0.07 Kh^{-1} exists near the ground which turns into heating at 1500 m altitude. The total heating rate increases until its maximum of 0.26 Kh^{-1} is reached at $z = 6000$ m. At higher altitudes, the total heating rate starts to decrease arriving at 0 Kh^{-1} at about 12 km. The standard deviation depicted by the shaded area is rather small for all of the heating rates. For instance, the maximum standard deviation of the total heating rate is 0.03 Kh^{-1} for a mean value of 0.21 Kh^{-1}. As the vertical profiles of the heating rates are similar for the warm bubble and the cold pool setups, also the results for the main effect (Fig. 6.9) are alike. In the cold pool setup, the first layer ranges from the ground to a height of 2250 m. In this layer the fall velocity of graupel contributes 48% to the output uncertainty of the total heating rate on average. In the second layer, which extends to a height of 3500 m, the impact of a_R increases reaching maximum values of 74%. Moreover, this layer is located at the same height as the strong increase of the heating due to cloud water and the cooling due to rain. Further up between 4000 m and 9000 m, the contribution from the IN concentration is increasing from 2% to 42% making it an important contributor in addition to the fall velocity of graupel (about 30%). Similar to the warm bubble setup, the main effect is reduced in the middle troposphere between 2000 m and 6000 m. The contributions from the IN concentration coincide with these heights where the ice phase hydrometeors provide contributions to the heating of the atmosphere. In the highest layer above 9000 m mainly the fall
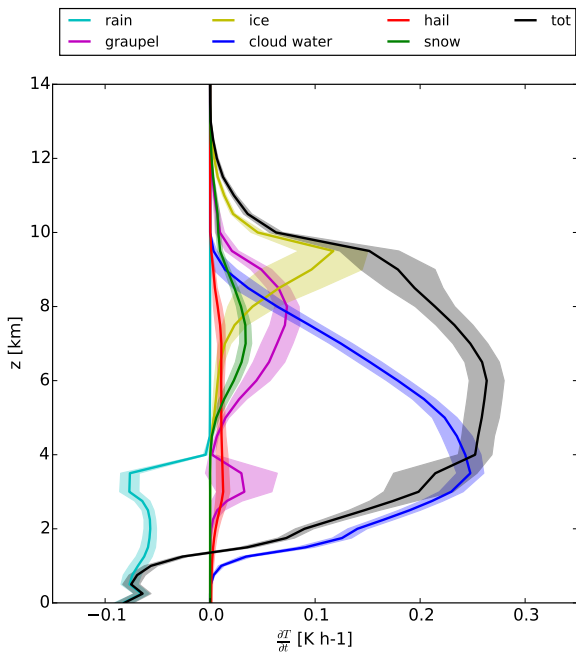
Fig. 6.8.: Vertical profiles of the mean diabatic heating rates by each hydrometeor and the mean total diabatic heating rate for the cold pool setup. The shaded areas denote the standard deviation.
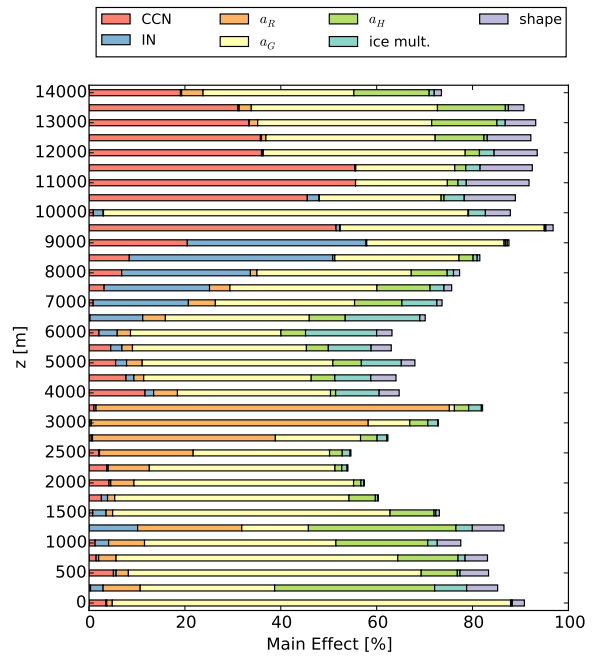
Fig. 6.9.: Bar plot of the main effect for the total diabatic heating rates when a cold pool is used to trigger convection.

velocity of graupel and the CCN concentration contribute to the uncertainty. The contribution from the fall velocity of graupel varies between 19% and 76% and the contribution from the CCN concentration reaches values of up to 56%.

Finally, Fig. 6.10 and 6.11 represent the results for the orography setup.

In the orography setup, the details of the structure of the vertical profiles are differing. The cooling near the ground is more intense (-0.11 Kh^{-1}) and vertically extended to an altitude of 4000 m. The total heating rate reaches its maximum of 0.12 Kh^{-1} at $z = 6000$ m and is decreasing above. The cooling caused by the evaporation of rain is quite pronounced, whereas the heating caused by cloud droplets has a maximum value of 0.05 Kh^{-1} which is less than in the other setups. Thus, the transition from cooling to heating is raised to a higher altitude. The standard deviation is largest for the heating due to cloud water where the standard deviation is 0.02 Kh^{-1} for a mean value of 0.04 Kh^{-1}. For the total heating rate the deviation has the highest value of 0.03 Kh^{-1} around the maximum at 6000 m. In general, the total heating rate is approximately half the value for the warm bubble and cold pool setups. This can be mainly traced back to the small amount of heating due to cloud water, snow and ice.
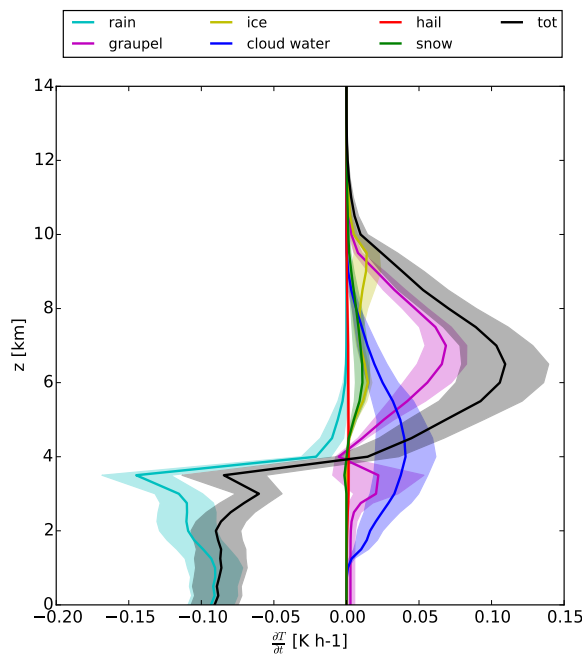
Fig. 6.10.: Vertical profiles of the mean diabatic heating rates by each hydrometeor and the mean total diabatic heating rate for the orography setup. The shaded areas denote the standard deviation.
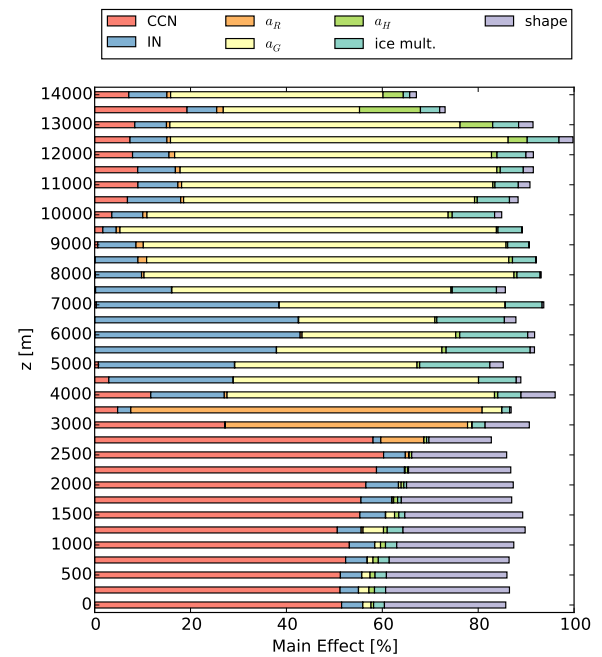
Fig. 6.11.: Bar plot of the main effect for the total diabatic heating rates when a mountain ridge is used to trigger convection.

In contrast, the cooling due to the evaporation of rain is more pronounced leading to stronger cooling in the lower troposphere in the orography setup. While the structure of the vertical profiles is comparable for the thermal triggers and the orography setup, the composition of the main effects of the total heating rate is different. Below 3000 m, the CCN concentration is the main contributor adding more than 50% to the output uncertainty. Between 3000 m and 4000 m, the output uncertainty is dominated by the fall velocity of rain. However above, the fall velocity of graupel is the controlling parameter $(50-73\%)$. The IN concentration has larger contributions of about 30% in the middle troposphere, whereas its impact decreases towards higher altitudes. The main effect represents 80% of the output uncertainty for most heights such that interaction effects are not as relevant. The layer between 3000 m and 4000 m, where the fall velocity of rain has the largest main effect, corresponds with the height in which the total heating rate transitions from negative to positive. Thus, the heights below, where the CCN concentration and the shape parameter are the largest contributors, are related to the net cooling of the atmosphere. The relevant hydrometeors adding to the total heating rate in the lower atmosphere are rain and cloud water. As the CCN concentration and the shape parameter directly affect the cloud water and via collision coalescence processes also indirectly affect the amount of rain, these two input parameters are dominant near the ground. Accordingly, in the layers above, where mainly the fall velocity of graupel adds to the uncertainty, the heating due to graupel is the most important part of the total heating rate.

Summarizing, the heating rates in both the warm bubble and cold pool setup are dominated by large contributions from the heating due to the formation of cloud water. Their results for the main effect are also similar. The fall velocities of rain and graupel, the CCN concentration and the IN concentration all add to the output uncertainty in different heights which correspond to features in the vertical profile. In contrast, the cooling due to rain and the heating due to graupel influence the total heating rate most in the orography setup leading to an enhanced layer of cooling near the ground. Contributions from a_R, a_G and the CCN and IN concentrations to the uncertainty of the total heating rate are also found in the orography setup. However their distribution is different from the results of the thermal triggers.

To further analyze these differences between the thermal triggers and the orography, the phase transition rates on which the heating rate for each hydrometeor class is based are plotted as temporal evolution in Fig. 6.12a - 6.14b.

	(a) absolute values	(b) normalized
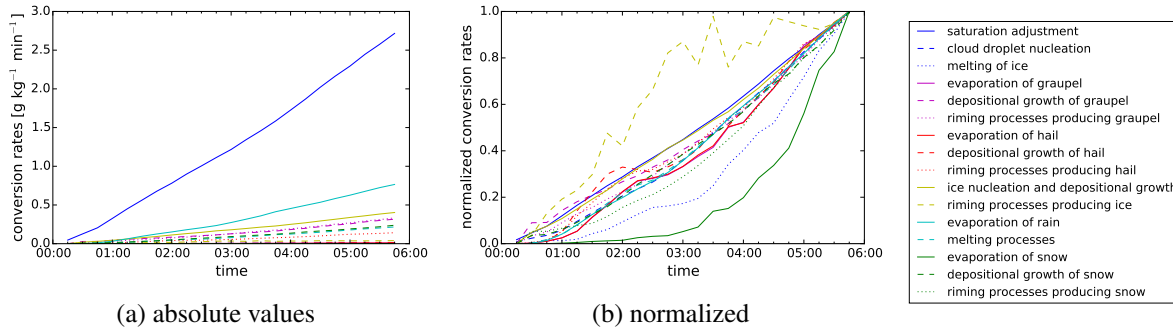
Fig. 6.12.: Conversion rates when the convection is triggered by a warm bubble. (a) Absolute values of the rates. (b) Normalized rates scaled with each maximum value.

The rates of the warm bubble setup are shown in Fig. 6.12. From the beginning of the simulation the saturation adjustment increases linearly to 2.7 g kg^{-1} min^{-1} which makes it the most dominant conversion and thus leads to the considerable contribution from the heating due to cloud water to the total heating rate. The evaporation of rain reaches an absolute value of 0.7 g kg^{-1} min^{-1} adding to the strong cooling in the lower troposphere. Other processes contributing to the heating rates are the ice nucleation and deposition, the depositional growth of graupel and riming processes producing graupel. However, their maximum absolute rates are below 0.5 g kg^{-1} min^{-1}.

In the plot of the temporal evolution of the normalized conversion rates (Fig. 6.12b), it can be seen that the riming processes producing ice are developing the fastest. The rate is increasing until a maximum is reached after 3.5 h. Most of the conversion rates are steadily growing during the whole simulation leading to a linear increase. The melting of ice and the evaporation of snow are developing slowly. Especially the evaporation of snow is almost negligible in the first three hours of the simulation. However, there is a strong exponential increase in the last three hours. Thus, some spin-up time is needed for snow to develop and to evaporate.

As the vertical profiles of the heating rates and the main effect of the total heating rate of the warm bubble and cold pool setups are much alike, a similar result for the phase transition rates is expected for the cold pool setup (Fig. 6.13a and 6.13b).

(a) absolute values   (b) normalized
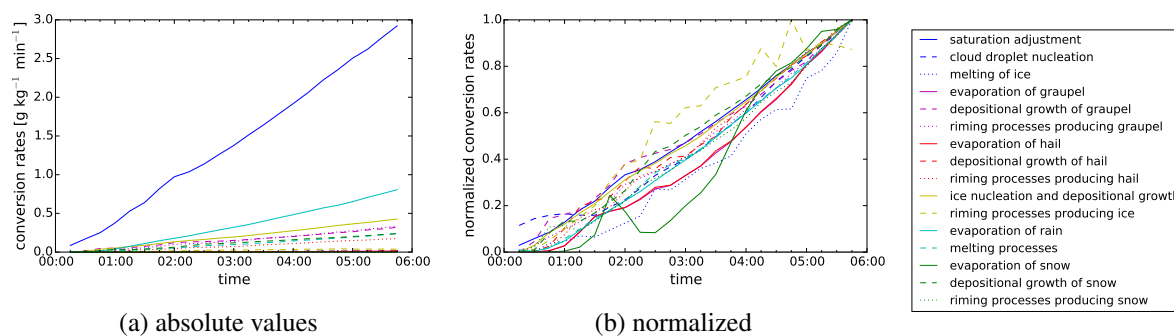
Fig. 6.13.: Conversion rates when the convection is triggered by a cold pool. (a) Absolute values of the rates. (b) Normalized rates scaled with each maximum value.

In the cold pool setup, the saturation adjustment is also the most prominent conversion rate growing linearly to values larger than 2.9 g kg^{-1} min^{-1} at the end of the simulation. The second important process is the evaporation of rain (0.8 g kg^{-1} min^{-1}) causing diabatic cooling near the ground. The processes that contribute to the heating rates in the upper troposphere have lower transition rates. The rates of the saturation adjustment and the evaporation of rain are slightly higher in the cold pool setup than in the warm bubble setup, but other than that the results are the same for both thermal triggers.

For the normalized conversion rates there are some minor differences between the two setups. The riming processes producing ice are not as prominent as in the warm bubble setup. It takes about two hours until this conversion increases faster than the other rates. Another difference is the evaporation of snow which is not as delayed in the cold pool setup. Although there are these two major differences of the riming processes leading to ice and the evaporation of snow between the warm bubble setup and the cold pool setup for the normalized conversion rates, they do not affect the heating rates greatly as the absolute value of these two processes is negligible (Fig. 6.13a).

The vertical profiles and the main effects are quite different in the orography setup, so differences in the phase transition rates (Fig. 6.14a and 6.14b) can be assumed, explaining the contrasting results mentioned above. Fig. 6.14a reveals that the temporal evolution differs from the ones seen before and also the absolute values are reduced by approximately 50%. Since the orography setup requires a spin-up time of five hours, phase transition rates are not equal to zero when the analysis starts. Thus, absolute values of 0.4 g kg^{-1} min^{-1} are found for the evaporation of rain at 00:15 h which increases to 0.7 g kg^{-1} min^{-1} at the end of the simulation. Other processes already present at the beginning of the analysis period are the depositional growth of graupel, riming producing graupel and melting leading to rain. The conversion

(a) absolute values   (b) normalized
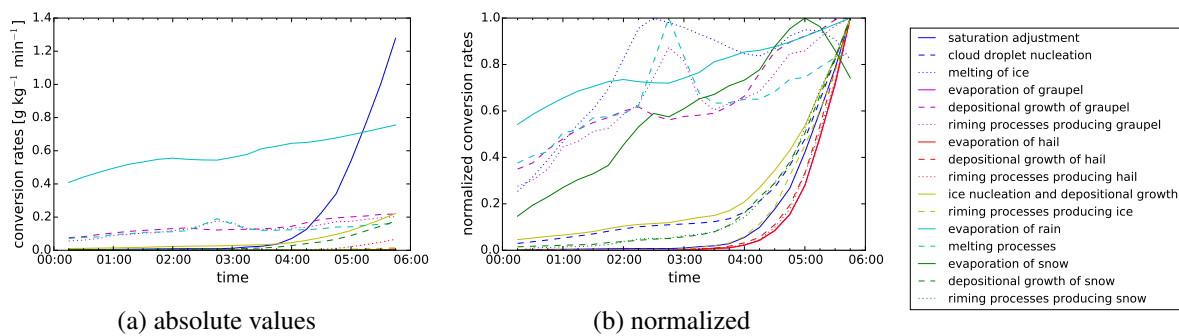
Fig. 6.14.: Conversion rates when the convection is triggered by a mountain ridge. (a) Absolute values of the rates. (b) Normalized rates scaled with each maximum value.

rate of the saturation adjustment increases exponentially from 03:00 h onward to a maximum value of $1.3 \text{ g kg}^{-1} \text{ min}^{-1}$. Apart from the lower absolute values for all processes, the order of the processes sorted by magnitude at the end of the simulation is the same in the orography setup, the warm bubble and the cold pool setup. The saturation adjustment shows the largest conversion rate followed by the evaporation of rain. However, a linear increase of the rates with time is found for the warm bubble and cold pool setup, whereas in the orography setup the rates increase exponentially with a delay of about three hours. Due to this delay there is less time for the conversion rates to grow which explains the reduced values.

In Fig. 6.14b the temporal evolution of the normalized conversion rates is presented for the orography setup. As already seen in Fig. 6.14a, most of the rates are increasing only slowly in the first three hours of the simulation but then increase rapidly in the last three hours. These processes that already developed phase transition rates above zero before the analysis period show a rather linear increase. The linear increase of the rates of the riming processes leading to graupel and the melting leading to rain is intermittent by a local maximum at about 02:45 h after the beginning of the analysis period. In addition, the melting of ice producing cloud water and the evaporation of snow also develop before the majority of the processes where the melting of ice is the fastest growing process in the first 02:30 h of the analysis. Thus, in contrast to the warm bubble and cold pool setups where the melting of ice and the evaporation of snow develop slowly, these rates are increasing before most others in the orography setup. Conversely, the rate of riming producing ice takes some time to increase, while it is the fastest growing rate for the thermal triggers.

To conclude, the conversion rates are similar in the warm bubble and cold pool setups. In both setups, the saturation adjustment shows the largest conversion rate followed by the conversion rate of the evaporation of rain which are all growing linearly as the simulation evolves. Minor differences are found when looking at the temporal evolution of the normalized rates. Compared to the warm bubble setup, the riming processes producing ice particles develop slower in the cold pool setup, whereas the evaporation

of snow and the melting of ice develop faster. However, the absolute values of these rates are rather low such that these differences do not affect the heating rates. Except for the processes including rain and graupel, the increase of the conversion rates is late by approximately three hours in the orography setup. Yet, the same processes as for the other triggers are important at the end of the simulation. Additionally, the maximum absolute values of the rates are about half of the rates observed for the thermal triggers which explains the small heating rates in Fig. 6.10. The temporal evolution of the normalized rates differs mainly for the riming leading to ice, the evaporation of snow and the melting of ice. As their absolute values are small, the differences of the heating rates between the warm bubble and cold pool setups and the orography setup cannot be attributed to the dissimilarities of the temporal evolution of individual conversion rates but rather to the general delay of their increase.

6.4. Sensitivity to CCN concentration

The emulators were used to examine the sensitivity of cloud water and hail to the CCN concentration for different microphysical conditions by looking at all 64 possible combinations of the input parameters when two discrete values are assigned each according to Tab. 6.1. More details of the method are given in section 5.4. The results for all trigger mechanisms are presented in Fig. 6.15. The percentages given in the following paragraphs all refer to their respective maximum values.

In Fig. 6.15a the sensitivities to the CCN concentration are shown for the warm bubble setup. The integrated cloud water increases rapidly up to a CCN concentration of $2000\,\mathrm{cm}^{-3}$. In more polluted environments, the rate of increase is reduced compared to cleaner environments. The spread of the different microphysical regimes is largest for small CCN concentrations. The mean sensitivity reveals that the integrated cloud water is increased by 50% of the maximum value, if the CCN concentration is changed from $100\,\mathrm{cm}^{-3}$ to $4000\,\mathrm{cm}^{-3}$. The integrated hail content is hardly affected by variations of the CCN. A small number of microphysical regimes indicates a slight increase of less than 10% which suggests a minor rise of the integrated hail content for polluted environments on average. Accordingly, the spread of the different regimes is less than 10%. Different characteristics are found for the maximum precipitation of hail. Here, a clear decrease can be seen for increasing CCN. Similar to the cloud water, the decrease is most pronounced between $100\,\mathrm{cm}^{-3}$ and $2000\,\mathrm{cm}^{-3}$. The variations between the microphysical regimes are quite high as in some cases no more hail is found for concentrations higher than $2000\,\mathrm{cm}^{-3}$, whereas in other cases only a reduction of 50% is observed at a CCN concentration of $4000\,\mathrm{cm}^{-3}$.

In the cold pool setup (Fig. 6.15b) the integrated cloud water increases for more polluted environments where the slope is steepest below CCN concentrations of $1000\,\mathrm{cm}^{-3}$. This results in an additional 40% of cloud water for a CCN concentration of $4000\,\mathrm{cm}^{-3}$. Although all regimes show an increase, the trend varies between the microphysical regimes such that the spread is about 20% for most parts of the CCN range. Also the results for the integrated hail content are more diverse than in the warm bubble setup.
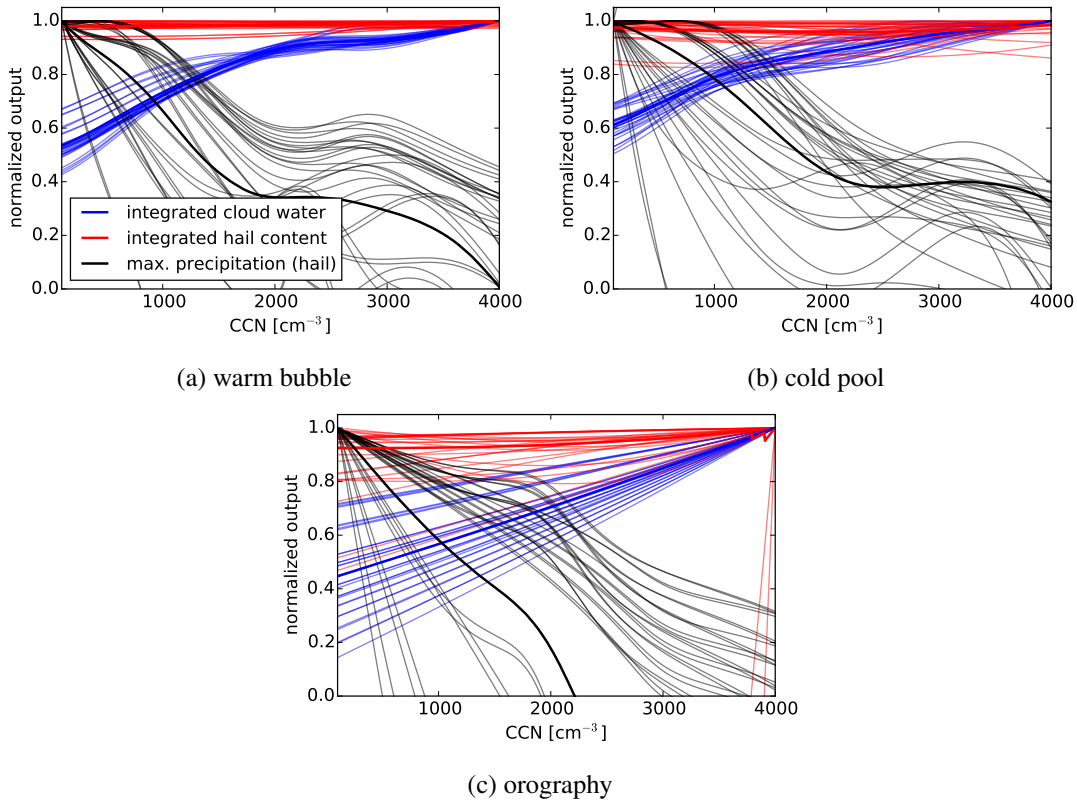
Fig. 6.15.: Sensitivity of mean integrated cloud water, mean integrated hail and precipitation by hail to variations in the CCN concentrations for (a) the warm bubble setup, (b) the cold pool setup, (c) the orography setup. Thin lines represent the results for 64 different environmental conditions and the bold lines denote the means. The results are divided by their respective maximum values for normalization.

Some regimes lead to an increase of 15% while other regimes show a decrease. However, the majority of the regimes are rather insensitive to changes of the CCN concentration. In contrast, the mean trend of the hail at the ground exhibits a distinct decrease for increasing CCN concentration. For some regimes a small increase is found between concentrations of $2000\,\mathrm{cm}^{-3}$ and $3500\,\mathrm{cm}^{-3}$. This leads to a local maximum of surface hail for rather polluted conditions with CCN concentrations between $3000\,\mathrm{cm}^{-3}$ and $3500\,\mathrm{cm}^{-3}$. Moreover, in most of the regimes the precipitation of hail is reduced by 60%-90% of their maximum values. Yet, in some regimes the precipitation of hail is reduced by 100% before the maximum CCN concentration is reached such that the spread around the mean is more than 50%.

In the orography setup (Fig. 6.15c), the same behavior of the three outputs is observed. As the CCN concentration increases, the integrated cloud water grows evenly where an increase of 55% is detected for the mean sensitivity. The spread of the different regimes is approximately 50% at a CCN concentration of $100\,\mathrm{cm}^{-3}$, but it decreases towards more polluted environments. Regarding the integrated hail content, most of the microphysical regimes are less affected by variations of the CCN concentrations than the other two variables. From concentrations of $100\,\mathrm{cm}^{-3}$ to $4000\,\mathrm{cm}^{-3}$, the mean increases by

approximately 10%, whereas some regimes show an increase by 50%. For single regimes, even a small decrease is visible followed by an increase. Thus, the spread of the results of the integrated hail content is largest in the orography setup. The precipitation of hail rapidly reduces for higher numbers of the CCN concentration. In most cases the amount of surface hail in polluted conditions is less than 20% of the amount found in clean conditions.

Comparing the results of the three trigger mechanisms shows that an increase of integrated cloud water in polluted environments is observed for all setups. This increase is most pronounced in the orography setup where the cloud water grows linearly. In contrast the increase retards at higher CCN concentrations in the warm bubble and cold pool setups. This behavior suggests that saturation occurs in polluted environments such that a further increase of the CCN concentration does not significantly increase the amount of cloud water. For all trigger mechanisms the sensitivity of the integrated hail content to the CCN concentration is quite low. Some variations are found due to changes of the microphysical conditions in the cold pool and orography setups, however the means vary less than 10%, if the environment is changed from clean to polluted conditions. This insensitivity of the integrated hail content to the CCN concentration was already seen in Fig. 6.1 where the main effect is illustrated. The contribution to the uncertainty of the hail content from the CCN concentration is only about 1%. Instead the main contributing parameters are the fall velocity of hail and the ice multiplication in the warm bubble and cold pool setups and the fall velocity of graupel in the orography setup. Although the precipitation of hail is decreasing in polluted environments for all trigger mechanisms, there are differences in the amount of the reduction. In the cold pool setup, the hail at the ground is reduced by 70% on average, in the warm bubble setup by almost 100% and in the orography setup no more hail is found at the ground before the maximum CCN concentration is reached. Thus, the precipitation of hail has the largest sensitivity to the CCN concentration based on the normalized values. In this analysis regarding the microphysics, the warm bubble setup is most robust to changes of the microphysical properties as the variations due to the different regimes are rather small. However, the variations of the maximum precipitation of hail are comparable for all three setups. Overall, while details of the sensitivities are differing, the mean trend is the same regardless of the trigger mechanism.

7. Emulator Studies for Perturbations of both the Environmental Conditions and the Microphysics

This chapter contains the results of the study where the impact of both the environmental conditions and the cloud microphysics is analyzed. The CCN and IN concentrations, wind shear, θ_0 and the fall velocities of graupel and hail are used as uncertain input parameters. A detailed description of the input parameters is given in section 4.5.1.

7.1. Cloud variables and precipitation

The main effect describing the percentage by which the output uncertainty could be reduced for a well-known input is illustrated in Fig. 7.1. The colors are chosen such that each parameter is assigned the same color as in chapters 5 and 6.

Fig. 7.1a presents the results for the warm bubble setup. Regarding the integrated cloud variables, each output has different parameters contributing most to its output uncertainty. For the cloud water, the CCN concentration contributes 63% and the wind wind shear 23%. In contrast, the output uncertainty of the hail content is made of comparable contributions from the CCN concentration (7%), the wind shear (13%), the potential temperature θ_0 (15%), the fall velocity of graupel (14%) and the fall velocity of hail (23%). The uncertainty of the ice content is dominated by θ_0 (61%) and the uncertainty of the graupel content is controlled by the fall velocity of graupel (83%). The uncertainty of the snow content is composed of all input parameters except for the fall velocity of hail. Both the wind shear (42%) and the fall velocity of graupel (32%) add to the uncertainty of the rain content. In the cold pool setup (Fig. 7.1b), the composition of the main effect is also diverse for the integrated cloud variables. Similar to the warm bubble setup, the CCN concentration is the main contributor to the output uncertainty of the cloud water adding 59%. The important parameters for the hail content are the fall velocities of graupel (25%) and hail (33%). The ice content and the graupel content show an opposite behavior. The uncertainty of the ice content is controlled by θ_0 (53%) and an additional contribution from the fall velocity of graupel (16%) is found, whereas for the graupel content, the fall velocity of graupel adds 88% to the uncertainty and θ_0 contributes 5%. The fall velocity of graupel is the largest contributor to the uncertainty of the snow content (41%). Most of the parameters contribute to the uncertainty of the rain content. The wind shear is responsible for 29% while the CCN concentration, θ_0, the fall velocity of graupel and the fall velocity of hail each add between 12% and 19%. In contrast to the various input parameters contributing to the uncertainties in the warm bubble and cold pool setups, the composition of the uncertainties of the

(a) warm bubble

(b) cold pool
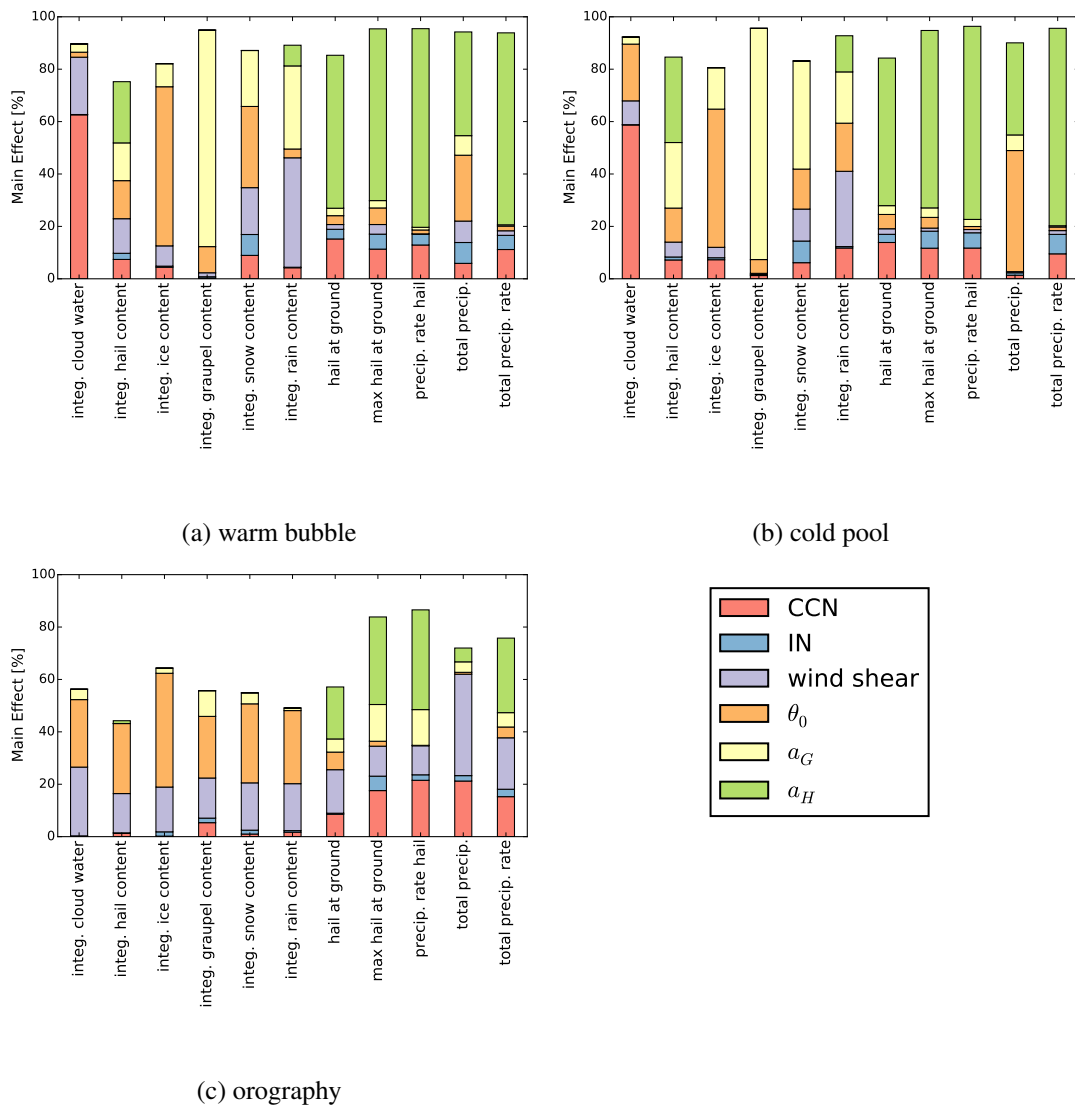
(c) orography

Fig. 7.1.: Bar plot of the main effect for integrated cloud variables and precipitation when (a) a warm bubble, (b) a cold pool, (c) a mountain ridge is used as trigger mechanism.

cloud variables is rather uniform in the orography setup. The potential temperature and the wind shear are identified as governing parameters where the largest contribution from θ_0 (43%) is found for the integrated ice content. While the sum of all main effects of the cloud variables is mostly above 80% in the warm bubble and cold pool setups, the main effects of the cloud variables sum up to a maximum of 63% in the orography setup. Thus, the uncertainty arising from interactions of the parameters with each other is almost as important as the uncertainty caused by each input parameter individually.

Regarding the precipitation variables in the warm bubble setup, the compositions of the uncertainties are more consistent than those of the cloud variables. The fall velocity of hail has the largest main effect for all variables. It contributes 40% to the output uncertainty of the total amount of precipitation and

more than 65% to the remaining variables. A contribution from the CCN concentration is found for all variables adding between 6% (total precipitation) and 15% (mean amount of hail at the ground). The results of the cold pool setup are comparable to those of the warm bubble setup. The fall velocity of hail is responsible for most of the uncertainty: it adds 35% to the total precipitation and up to 75% to the total precipitation rate. The uncertainty of the total precipitation is dominated by the potential temperature which adds 46%. Except for the total precipitation, the CCN concentration contributes $10\% - 14\%$ to the output uncertainties of the precipitation variables. In the orography setup, larger contributions are found not only from the CCN concentration and the fall velocity of hail but also from the wind shear and the fall velocity of graupel. The uncertainty of the mean amount of hail at the ground consists of comparable contributions from the wind shear (17%) and the fall velocity of hail (20%). The fall velocity of hail is the largest contributor for the maximum amount of hail and the precipitation rate of hail providing 33% and 38% of the uncertainty, respectively. The uncertainty of the total precipitation is controlled by the wind shear which explains 38%. The main contributors to the output uncertainty of the total precipitation rate are the fall velocity of hail (28%), the wind shear (20%) and the CCN concentration (15%). Similar to the cloud variables, the interaction effects are larger in the orography setup. Here, the first-order main effects explain on average 70% of the output uncertainty, whereas in the warm bubble and cold pool setups they sum up to about 90%.

Overall, the potential temperature θ_0 contributes to the output uncertainty for all trigger mechanisms. In the warm bubble and cold pool setups, the fall velocity of graupel and also the CCN concentration explain parts of the uncertainty. In the orography setup, the wind shear is contributing in addition to θ_0. Thus, the wind shear is particularly important in the orography setup where it determines the flow over the orography which then triggers convection. Regarding the precipitation variables, the fall velocity of hail is dominant in all three setups. Thus, it significantly affects the output uncertainty of the different precipitation variables regardless of the trigger mechanism. This implies a distinct contribution from the ice phase, especially of hail, to the observed precipitation. In particular for the cloud variables, the interaction effects are as large as the first-order main effects in the orography setup, whereas in the other two setups more than 80% of the uncertainty are explained by the individual main effects. This indicates that the formation of convective clouds is more complex and requires the input parameters to interact when a mountain ridge is used to trigger convection.

7.2. Size distribution of hail

As described in section 5.2, 1000 size distributions of surface hail are generated by the emulators and are shown in Fig. 6.3 including their respective means.
The size distributions of the warm bubble setup are illustrated in Fig. 7.2a. The maximum of the mean number concentration of 2 m^{-4} is located at a diameter of 5 mm. On average, the concentration at

(a) warm bubble

(b) cold pool

(c) orography

(d) mean of all triggers
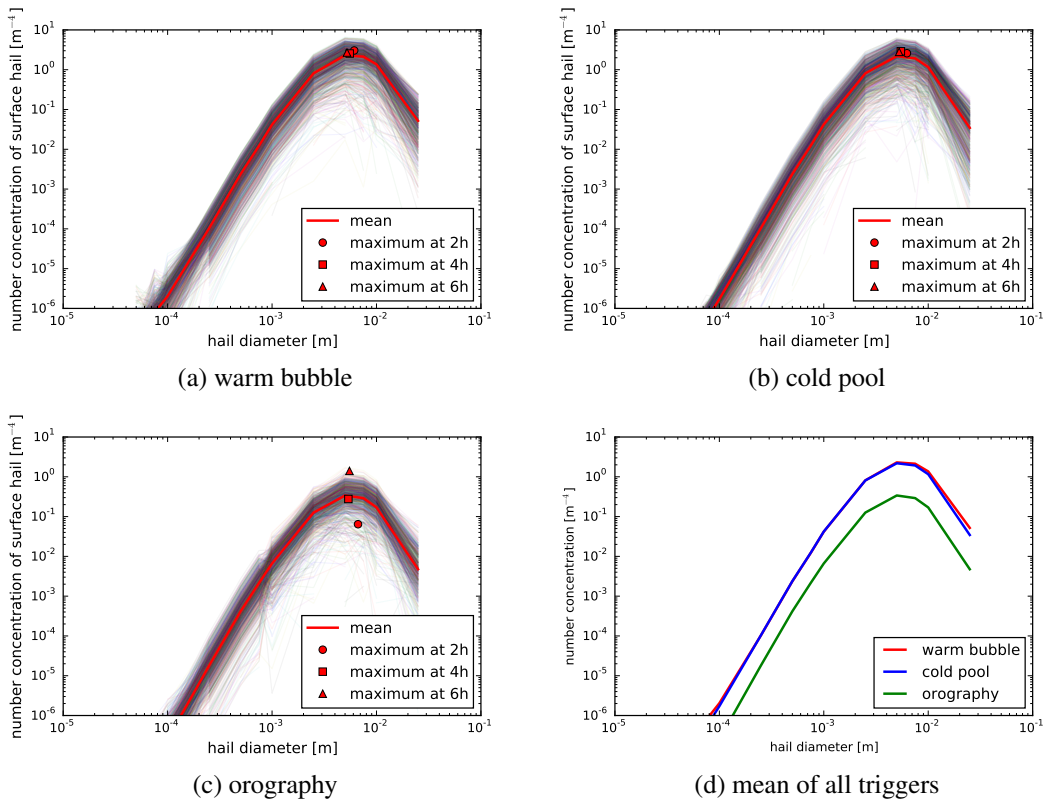
Fig. 7.2.: Size distributions of surface hail of 1000 randomly generated simulations for the warm bubble setup, the cold pool setup and the orography setup. The bold red line denotes the sample mean and the markers stand for the mean position of the maximum of the distribution after two hours, four hours and six hours into the simulation.

the largest considered diameter of 2.5 cm is $5 \cdot 10^{-2}$ m^{-4}. The spread of the distributions is moderate for small hailstones, however it fans out approaching the maximum. The markers indicate that, as the simulation proceeds, the radius for which the highest number concentration is found slightly decreases such that smaller hailstones are produced.

Fig. 7.2b shows the size distributions of the cold pool setup. The maximum of the mean distribution is identical to that of the warm bubble setup while the largest considered diameter has a slightly higher concentration (Fig. 7.2d). Two hours after the start of the simulation, the maximum number concentration is located at a diameter of 6 mm, but as time evolves it shifts towards a smaller diameter of 5 mm while the number concentration is rather constant.

The results of the orography setup are depicted in Fig. 7.2c. For the mean distribution the maximum number concentration of 0.3 m^{-4} is found for a diameter of 5 mm. The concentration is about an order of magnitude below the results of the warm bubble and cold pool setups. Consequently, the number concentration at the largest diameter is also smaller ($5.5 \cdot 10^{-3}$ m^{-4}) (Fig. 7.2d). The maximum number concentration changes considerably during the simulation. After two hours, the maximum is located at diameter of about 7 mm and a number concentration of $6 \cdot 10^{-2}$ m^{-4}. Two hours later, the maximum co-

incides with the maximum of the mean distribution and at the end of the simulation a maximum number concentration of $0.5 \, \text{m}^{-4}$ is found at a diameter of 5.5 mm. So the diameter varies little but the number concentration is increased by a factor of 10.

The highest number concentration is found for a hail diameter of 5 mm in all three setups and also the variations due to the different input combinations are comparable. While the number concentration is almost the same in the warm bubble and cold pool setup, it is lower in the orography setup. Furthermore, the position of the maximum hardly changes in the warm bubble and cold pool setup but in the orography setup a clear increase of the number concentration is visible during the simulation.

For a more detailed analysis, the input parameters are varied systematically to evaluate their impact on the size distribution (see section 5.2). An overview of the discrete values chosen for each input parameter is given in Tab. 7.1.

Tab. 7.1.: Input values representing both lower and higher values of the parameter ranges which are used to analyze the size distribution of hail.

input	lower value (-)	higher value (+)	units
CCN concentration	500	3000	cm^{-3}
IN concentration	0.1	10	scaling factor
wind shear	0.5	1.0	scaling factor
potential temperature θ_0	298	302	K
fall velocity of graupel (a_G)	0.5	1.5	scaling factor
fall velocity of hail (a_H)	0.8	1.2	scaling factor

All possible combinations of these input parameters lead to a total of 64 regimes for which the emulators are used to generate size distributions of the surface hail. The results are shown in Fig. 7.3 where on the left hand side the size distributions are illustrated grouped by governing input parameters and on the right hand side the corresponding main effect is depicted.

Fig. 7.3a presents the size distributions of the warm bubble setup. They can be separated into three groups. The first group are those size distributions that have the lowest number concentration. Their maximum is located between 0.3 and $1 \, \text{m}^{-1}$ at a diameter of 0.75 mm. These distributions are characterized by a low value of θ_0. Opposite, the highest number concentrations of $4 - 6 \, \text{m}^{-4}$ at a hail diameter of 5 mm appear for regimes in which low values of the fall velocity of graupel and high values of the fall velocity of hail are found. The third group comprises the remaining distributions having medium number concentrations and any other combination of input parameters. This is also confirmed by the plot of the main effect (Fig. 7.3b). For hail diameters between 0.1 mm and 1 mm, θ_0 contributes 50% to the output

(a) size distribution (WB)

(b) main effect (WB)

(c) size distribution (CP)

(d) main effect (CP)

(e) size distribution (Oro)

(f) main effect (Oro)
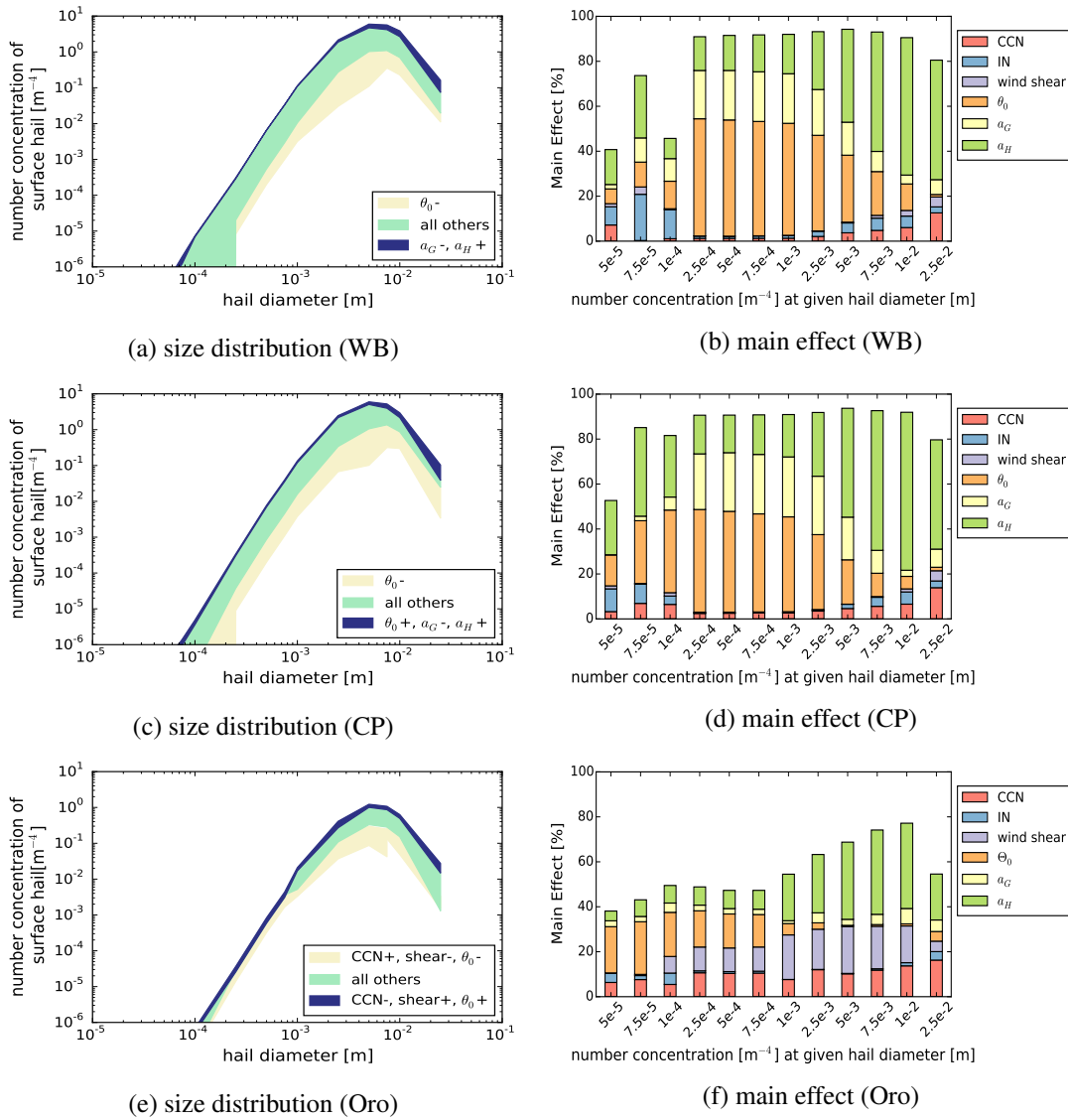
Fig. 7.3.: Left: Size distributions of hail at $z = 0$ m for all trigger mechanisms. The shading in (a) and (c) illustrates regimes of the size distributions controlled by θ_0, the fall velocity of hail and the fall velocity of graupel. The shading in (e) illustrates regimes of the size distributions controlled by the CCN concentration, the IN concentration and θ_0. Right: Bar plots of the main effect for the mean size distribution of surface hail for all trigger mechanisms using the whole parameter range.

uncertainty of the size distribution. Towards larger diameters, the influence of θ_0 declines, whereas the contribution from the fall velocity of hail increases. It adds up to 61% and is the largest contributor to the uncertainty for diameters larger than 5 mm.

Similar to the warm bubble setup, the size distributions of the cold pool setup can also be divided into three groups (Fig. 7.3c). The group with the lowest number concentration of surface hail is characterized by a low value of θ_0. Size distributions with number concentrations between 1 m^{-4} and 5 m^{-4} at

a diameter of 5 mm are the distributions found the most, such that different regimes contribute to this group and no specifications of the input parameters are made. However, the size distributions with the highest number concentrations are produced by regimes that have a high value for θ_0, a low value for the fall velocity of graupel and a high value for the fall velocity of hail. These regimes reach number concentrations of $5 - 6 \, \mathrm{m}^{-4}$ at a diameter of 5 mm. The contributions from the input parameters to the main effect of the size distribution of surface hail are illustrated in Fig. 7.3d. The potential temperature θ_0 contributes to the output uncertainty, especially between diameters of 0.25 mm and 1 mm. Also the fall velocity of graupel mainly contributes for medium diameters. It adds approximately 25% to the uncertainty for diameters from 0.25 mm to 2.5 mm. The last input parameter with large contributions is the fall velocity of hail. In contrast to θ_0 and the fall velocity of graupel, its contributions are found for small and large diameters rather than medium sizes. Thus, the three main contributors to the output uncertainty of the size distribution are the same input parameters that control the maximum number concentrations of the distributions.

Finally, the results of the orography setup are shown in Fig. 7.3e and 7.3f where the size distributions are found in Fig. 7.3e and the corresponding main effect in Fig. 7.3f. For the orography setup three groups of the size distributions can be distinguished as well. However, the governing parameters differ from those of the thermal triggers. The regimes leading to distributions with low number concentrations have a high CCN value, low wind shear and a low value for θ_0. Accordingly, the highest number concentrations require regimes with a low CCN concentration, high wind shear and a high value of θ_0. Other regimes that do not include the mentioned combinations of these three input parameters generate size distributions that have number concentrations in-between the two extremes. Moreover, the CCN concentration, the wind shear and θ_0 also influence the output uncertainty of the size distribution (Fig. 7.3f). The CCN concentration contributes to the uncertainty of the size distribution for all diameters where the contribution increases for larger diameters. Similarly, the contribution from the wind shear increases for larger diameters. The potential temperature shows an opposite behavior, as it has a main effect of 20% for the smallest considered diameter which decreases to 5% at a diameter of 1 mm.

Comparing all setups shows that the size distributions of the warm bubble and cold pool setups have the same controlling parameters (θ_0 and the fall velocities of graupel and hail) and also the main effects are similar for these two setups. In contrast, in the orography setup, the CCN concentration and the wind shear are governing the number concentration in addition to θ_0. Moreover, as seen for other plots of the main effect for the orography setup, the interaction effects are almost as significant as the first-order main effects and therefore interactions are more predominant. Summarizing, the potential temperature θ_0 is clearly influencing the number concentration of surface hail. For low values of θ_0 low number concentrations and for high values of θ_0 large number concentrations are found regardless of the trigger mechanism.

7.3. Diabatic heating rates

The mean vertical profiles of $10,000$ emulator predictions of the heating rates (see section 5.3) are illustrated in Fig. 7.4 for the warm bubble setup where the shaded areas denote the standard deviations.
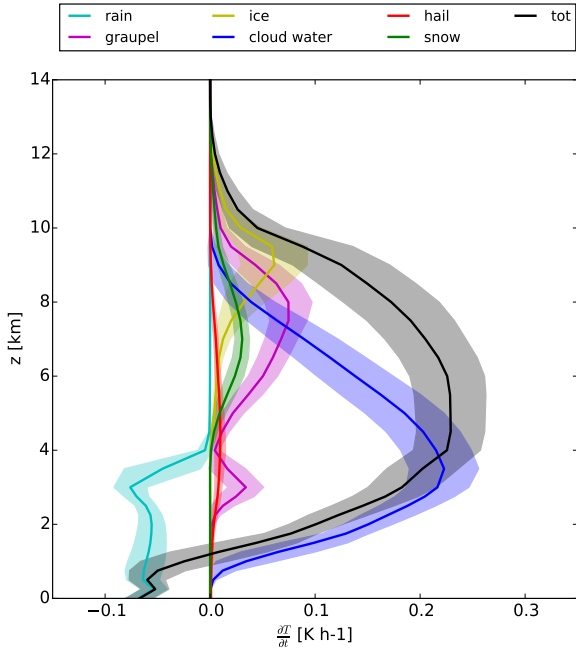
Fig. 7.4.: Vertical profiles of the mean diabatic heating rates by each hydrometeor and the mean total diabatic heating rate for the warm bubble setup. The shaded areas denote the standard deviation.
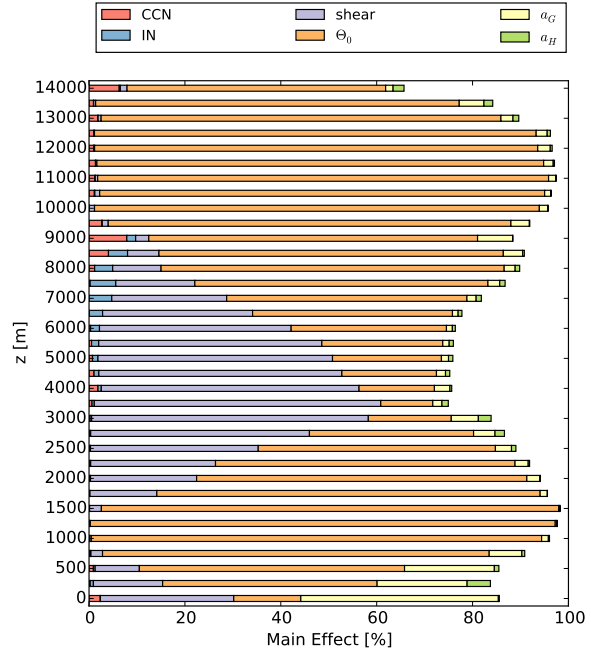
Fig. 7.5.: Bar plot of the main effect for the total diabatic heating rates when a warm bubble is used to trigger convection.

The total heating rate has negative values of about -0.05 Kh^{-1} below heights of 1000 m. This is due to the cooling connected to the evaporation of rain which is found in the lowermost 4 km of the troposphere. However, the total heating rate is negative only up to 1250 m as at this height the heating due to the formation of cloud water rapidly increases. Correspondingly, the total heating rate grows to values of 0.23 Kh^{-1} in the layer between $z = 4000$ m and $z = 6500$ m. When the contribution from the cloud water decreases, the hydrometeor classes of the ice phase, snow, graupel and ice, add to the total heating rate in the upper troposphere until it vanishes at the tropopause. Heating caused by the formation of hail is found in the middle troposphere between 2750 m and 6000 m. However, its maximum rate is below 0.01 Kh^{-1} such that this contribution is not relevant for the total heating rate. The shaded areas denoting the standard deviations are of reasonable size and scale with the absolute values of the rates. The maximum standard deviation of the total heating rate is 0.05 Kh^{-1}, which corresponds to 15% of the mean value, and is found in the middle troposphere where the maximum heating rate is located. Hence,

variations across the whole input parameter space do not lead to major changes of the vertical heating rates. The corresponding main effect of the profile of the total heating rate is shown in Fig. 7.5. In the lower troposphere up to heights of 2500 m, the potential temperature is the largest contributor to the output uncertainty of the total heating rate. From 1750 m onward, the main effect of the wind shear grows from 14% to its maximum of 60% at $z = 3500$ m. Above, it decreases down to 3% at a height of 9 km. Accordingly, the wind shear contributes most to the uncertainty between $z = 2750$ m and $z = 6000$ m. As the contribution of the wind shear decreases with increasing height, the effect of θ_0 dominates the output uncertainty of the total heating rate in the upper troposphere where it contributes up to 94%. In general, the main effects explain more than 80% of the output uncertainty, except for the middle troposphere where the contribution from the wind shear is increased.

Looking at both Fig. 7.4 and Fig. 7.5, it is evident that the increase of the main effect of the wind shear between 2 km and 7 km coincides with the contribution from the cloud water to the vertical profile of the total heating rate. Thus, the wind shear appears to be an important parameter determining the location of the formation of cloud water and its amount.

The vertical heating rates and their standard deviations generated by the emulators of the cold pool setup are shown in Fig. 7.6.
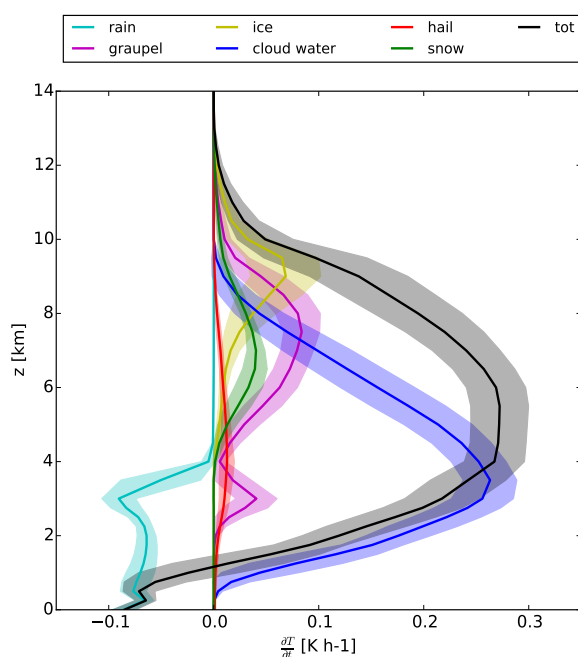
Fig. 7.6.: Vertical profiles of the mean diabatic heating rates by each hydrometeor and the mean total diabatic heating rate for the cold pool setup. The shaded areas denote the standard deviation.
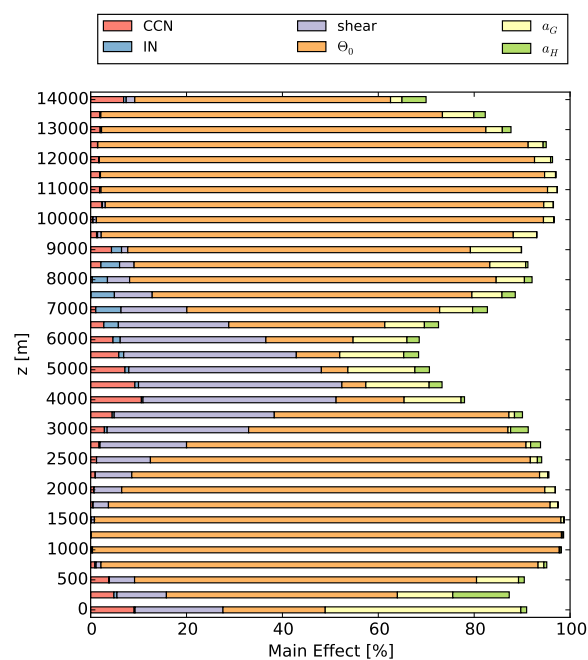
Fig. 7.7.: Bar plot of the main effect for the total diabatic heating rates when a cold pool is used to trigger convection.

The cooling connected to the evaporation of rain is pronounced in the lowest 4 km above the ground. On average, the rate is $-0.07 \, \text{Kh}^{-1}$. Above 500 m, the heating caused by cloud water increases until its maximum of $0.26 \, \text{Kh}^{-1}$ is reached at a height of 3500 m. Accordingly, the total heating rate is negative below 1000 m and becomes positive above. While the heating related to cloud water starts to decrease above 3500 m, the heating rates related to ice phase hydrometeors emerge in the middle and upper troposphere. The total heating rate has a standard deviation of $0.03 \, \text{Kh}^{-1}$ at a height of 3500 m which corresponds to 10% of the mean value. Fig. 7.7 illustrates the main effect of the total heating rate as stacked bar charts. Similar to the warm bubble setup, the potential temperature is the most important parameter in the lower troposphere where it contributes up to 98% to the output uncertainty. While the influence of θ_0 decreases above 2500 m, the main effect of the wind shear increases making it the largest contributor in the middle troposphere (up to 42%). Above a height of 6500 m, the effect of the wind shear decreases and the contribution from θ_0 is the largest contributor to the uncertainty. In the upper troposphere, θ_0 contributes more than 90% such that the effect of the remaining parameters is of minor importance. As seen for the warm bubble setup, first order main effect are responsible for more than 80% of the uncertainty except for the middle troposphere where the contribution from the wind shear is largest.

Combining Fig. 7.6 and Fig. 7.7 reveals that the large contributions from the wind shear to the uncertainty in the middle troposphere are not perfectly aligned with the vertical profile of the heating rate caused by cloud water as it was the case in section 5.3. The maximum of the main effect of the wind shear is found at a height of 4500 m, while the maximum of the heating rate of cloud water is located at a height of 3500 m. Furthermore, the reduced sum of the main effects in this layer indicates that especially in these heights, where the total heating rate is largest, the interactions of the input parameters have an enlarged effect on the uncertainty.

Fig. 7.8 shows the mean vertical heating rates and their standard deviations for the orography setup. As already seen for the warm bubble and cold pool setups, the total heating rate is negative close to the ground because of the evaporation of rain and becomes positive at a height of $z = 3500 \, \text{m}$ due to the heating caused by the formation of cloud water. The total heating rate reaches its maximum of $0.12 \, \text{Kh}^{-1}$ at $z = 6000 \, \text{m}$ and decreases at higher levels. In contrast to Fig. 7.4 and Fig. 7.6, the standard deviations are quite pronounced in Fig. 7.8. Especially the heating caused by the formation of cloud water shows large standard deviations of $0.1 \, \text{Kh}^{-1}$ which is the double of the mean value. So, the formation of cloud water clearly reacts to variations of the input parameters. Even though the standard deviations of the other hydrometeors are in a moderate range, the total heating rate shows a maximum standard deviation of $0.1 \, \text{Kh}^{-1}$ which is almost equal to the corresponding mean. The main effects of the vertical profile of the total heating rate are presented in Fig. 7.9.
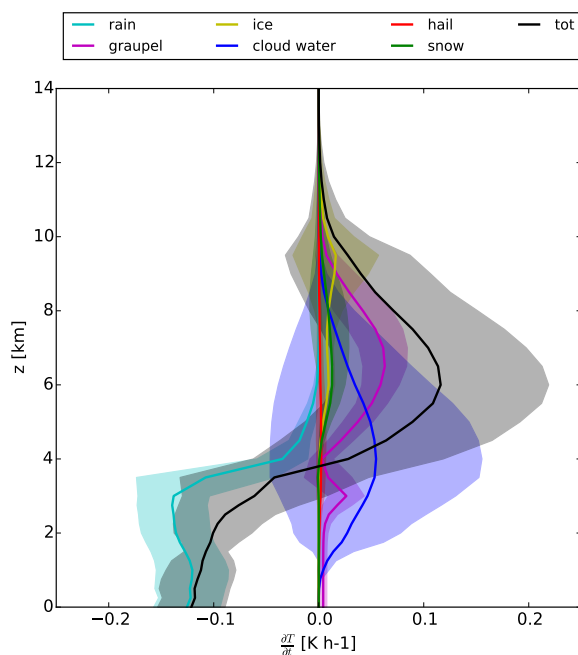
Fig. 7.8.: Vertical profiles of the mean diabatic heating rates by each hydrometeor and the mean total diabatic heating rate for the orography setup. The shaded areas denote the standard deviation.
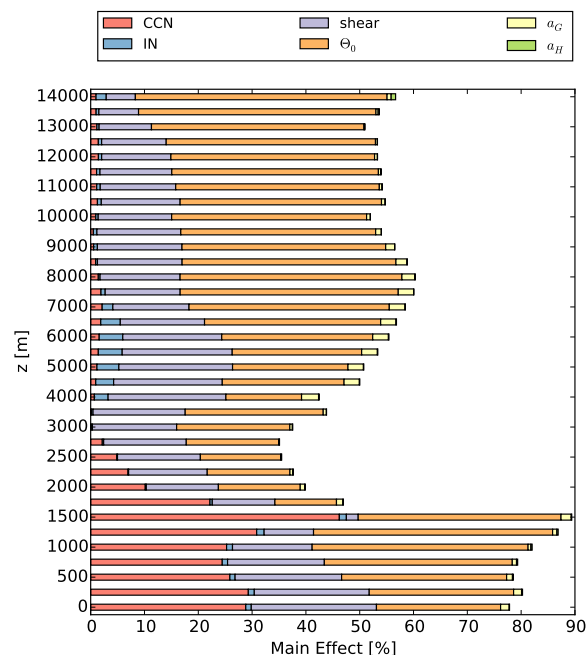
Fig. 7.9.: Bar plot of the main effect for the total diabatic heating rates when a mountain ridge is used to trigger convection.

Below 2000 m, the CCN concentration, the wind shear and θ_0 all contribute to the output uncertainty of the total heating rate where the contributions from the CCN concentration and θ_0 are of comparable size. At higher levels, the contribution from the CCN concentration decreases and the wind shear and θ_0 are the main contributors. Between 2 km and 4 km altitude, both the wind shear and θ_0 add $15-20\%$. As there are hardly any contributions from other parameters, the sum of all main effects drops below 40% in this layer. In the upper troposphere, the contribution from θ_0 increases to about 40% such that θ_0 is the most dominant parameter. Except for the lower troposphere, where the first-order main effects sum up to about 80%, less than 60% of the uncertainty can be explained by the individual contributions from the input parameters. Thus, the interactions of the parameters are almost as important as the first-order main effects.

Comparing the vertical profiles of the heating rates of all trigger mechanisms shows that the profiles of the warm bubble setup and the cold pool setup are quite similar. They exhibit the same structures and the maxima of each rate are located at the same heights. However, in the cold pool setup the rates are slightly higher. Moreover, the variance is reduced in the cold pool setup. On the one hand, the heating rates are in general smaller in the orography setup, especially for the heating related to cloud water.

On the other hand, the cooling near the ground connected to rain is most pronounced in the orography setup as cooling rates of more than $-0.1\,\mathrm{Kh^{-1}}$ are reached. The most distinct difference is the standard deviation which is larger in the orography setup. This leads to the conclusion that the heating rates and specifically the heating due to the formation of cloud water are not as robust and easily react to variations of the input parameters. Regarding the main effect, the uncertainty of the total heating rate is controlled by θ_0 and the wind shear in all setups. In the warm bubble and cold pool setups, the contributions from the wind shear are mainly found in the middle troposphere connected to the maximum heating rate of the cloud water, while in the orography setup contributions from the wind shear are present in all heights. So for the thermal triggers, the wind shear affects only that volume of the cloud where cloud water is generated. In the orography setup, convection is triggered by flow over a mountain ridge such that the wind shear affects not only the middle troposphere but is responsible for the formation of clouds across all heights.

For a more detailed analysis, the heating rates are split into processes including phase transitions which contribute to the heating rates such as riming or melting. The mean rates of these processes are shown in Fig. 7.10a for the warm bubble setup. As the absolute values differ for the considered processes, Fig. 7.10b further depicts the mean conversion rates normalized with their respective maximum such that the temporal evolution of each process is traceable.

(a) absolute values   (b) normalized
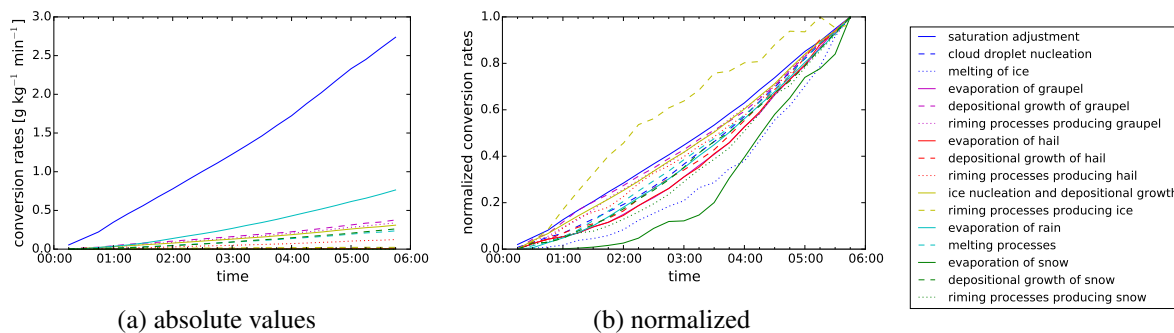
Fig. 7.10.: Conversion rates when the convection is triggered by a warm bubble. (a) Absolute values of the rates.
(b) Normalized rates scaled with each maximum value.

From the beginning of the simulation onward, the saturation adjustment has the largest conversion rate which increases to $2.7\,\mathrm{g\,kg^{-1}\,min^{-1}}$ at the end of the simulation contributing significantly to the heating caused by cloud water. The phase transition rate of the evaporation of rain has the second largest absolute value reaching a rate of $0.8\,\mathrm{g\,kg^{-1}\,min^{-1}}$. In combination with the melting processes leading to rain, which have a maximum conversion rate of $0.2\,\mathrm{g\,kg^{-1}\,min^{-1}}$, the evaporation of rain is responsible for the cooling in the lower troposphere. The two processes determining the heating rate of graupel are the depositional growth of graupel and riming processes producing graupel. Both have conversion rates of about $0.4\,\mathrm{g\,kg^{-1}\,min^{-1}}$ at the end of the simulation. Other processes are only of minor importance

for the heating rates. Fig. 7.10b shows that most of the phase transition rates, the saturation adjustment and the depositional growth of graupel for example, grow linearly from the beginning to the end of the simulation. This suggests steady processes during the simulation. However, a few processes follow a different temporal evolution. On the one hand, riming processes producing cloud ice are developing fastest at the beginning such that more than 50% of the maximum value are already reached after a third of the simulation time. On the other hand, processes like the melting of ice producing cloud water and the evaporation of snow are delayed in their evolution compared to the other processes. This behavior is most pronounced for the evaporation of snow.

The absolute value of the conversion rates and the normalized conversion rates for the cold pool setup are presented in Fig. 7.11a and Fig. 7.11b.

(a) absolute values　　　　　　　(b) normalized
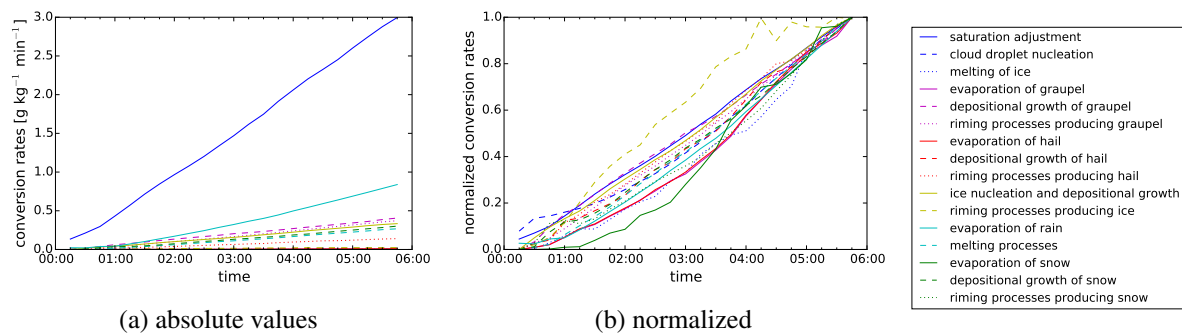
Fig. 7.11.: Conversion rates when the convection is triggered by a cold pool. (a) Absolute values of the rates. (b) Normalized rates scaled with each maximum value.

Just as for the heating rates, the results of the warm bubble setup and the cold pool setup are similar where higher absolute values appear in the cold pool setup. Thus, after a linear growth, the saturation adjustment has the largest conversion rate with a maximum value of $3 \, \mathrm{g \, kg^{-1} \, min^{-1}}$ driving the heating due to the formation of cloud water. Next, the absolute value of the conversion rate of the evaporation of rain is $0.8 \, \mathrm{g \, kg^{-1} \, min^{-1}}$ at the end of the simulation. Regarding the heating caused by the formation of graupel, both the depositional growth and riming processes add equally, having conversion rates of $0.4 \, \mathrm{g \, kg^{-1} \, min^{-1}}$ each. Remaining processes such as the evaporation of graupel can be neglected. Looking at the detailed temporal evolution in Fig. 7.11b, most of the conversion rates are increasing evenly during the simulation. After about an hour, the rate of the riming processes producing cloud ice intensifies and reaches its maximum rate at 04:15 h. The delay of the evolution of some processes found for the warm bubble setup is not as distinct for the cold pool setup. Only the evaporation of rain shows larger deviations. There is a spin up time of about 01:15 h before this process starts to develop, but due to a rapid increase the rate of the evaporation of snow is well within the range of the normalized conversion rates of the other processes after 03:45 h.

Finally, the conversion rates of the orography setup are shown in Fig. 7.12a and 7.12b.

(a) absolute values   (b) normalized
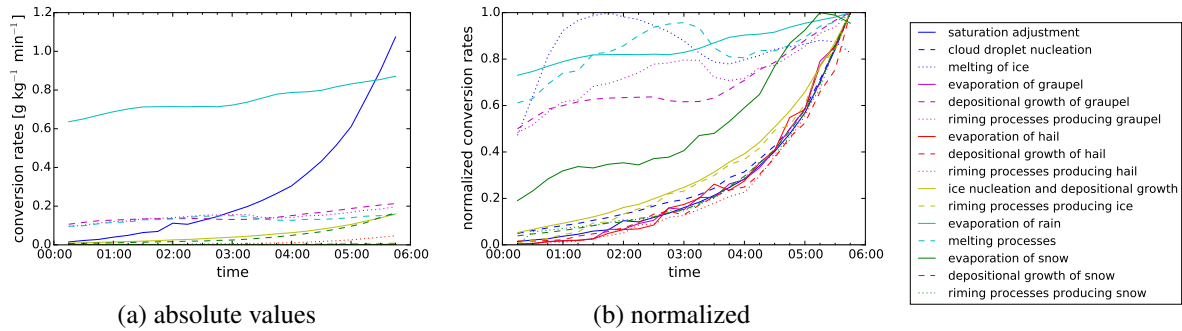
Fig. 7.12.: Conversion rates when the convection is triggered by a mountain ridge. (a) Absolute values of the rates. (b) Normalized rates scaled with each maximum value.

As the orography setup requires some spin up time to generate convection, the phase transition rates are not necessarily equal to zero at the beginning of the evaluation period. So a conversion rate of approximately $0.6\,\mathrm{g\,kg^{-1}\,min^{-1}}$ is found for the evaporation of rain at 00:15 h. This rate increases irregularly to an absolute value of $0.9\,\mathrm{g\,kg^{-1}\,min^{-1}}$ at the end of the simulation. The rate of the saturation adjustment is rapidly increasing to $1.1\,\mathrm{g\,kg^{-1}\,min^{-1}}$ at 04:00 h after it was growing slowly at the beginning. This explains the dominant appearance of the heating connected to rain and the limited contribution from the heating caused by the formation of cloud droplets in Fig. 7.8. Also the melting processes leading to rain, the depositional growth of graupel and the riming leading to graupel have an offset of $0.1\,\mathrm{g\,kg^{-1}\,min^{-1}}$. While the conversion rates related to graupel increase to $0.2\,\mathrm{g\,kg^{-1}\,min^{-1}}$, the rate of the evaporation of rain is rather constant. Other processes have conversion rates of less than $0.1\,\mathrm{g\,kg^{-1}\,min^{-1}}$. Furthermore, the detailed temporal evolution of the normalized conversion rates in Fig. 7.12b is different from the results of the warm bubble and the cold pool setup. About two thirds of the processes follow an exponential function. The conversion rate of the evaporation of snow also follows an exponential function, however its offset at the beginning is larger such that it deviates from the other processes. Both the riming processes producing graupel and the melting processes leading to rain have a local maximum at 03:00 h.

Comparing the results of the three trigger mechanisms shows that the structure of the vertical profiles of the heating rates is roughly the same in all setups: The total heating rate is negative near the ground and reaches its maximum in the middle troposphere between 4 km and 6 km. The values of the heating rates and the size of the standard deviations are comparable for the warm bubble setup and the cold pool setup. In contrast, the heating rates are considerably reduced in the orography setup and thus also the conversion rates are smaller. This means that the cloud volume of the generated deep convection is diminished such that less phase transitions occur. Moreover, the standard deviations are increased which leads to the conclusion that the orography setup reacts a lot to changes of the input parameters, whereas the warm

bubble and cold pool setups are rather robust. The conversion processes happening the most in all setups are the saturation adjustment and the evaporation of rain contributing to the heating by cloud water and rain, respectively. In the orography setup, the phase transitions including rain and graupel develop early in the simulation which explains the large impact of the heating by rain and graupel on the total heating rate. In the warm bubble and cold pool setups, the total heating rate is mainly influenced by the heating related to cloud water. In general, the conversion rates grow linearly for the thermal triggers and exponentially for the mountain ridge. Regarding the results of the main effect, the potential temperature θ_0 is an important contributor to the output uncertainty of the total heating rate for all triggers. However, there are also differences visible between the three setups. While in the warm bubble and cold pool setups the wind shear contributes to the uncertainty only in the middle troposphere coinciding with the maximum contribution to the total heating rate from the heating caused by cloud water, the wind shear is adding to the uncertainty in all levels in the orography setup. In addition, the effect of parameter interactions is larger when a mountain ridge is used to trigger convection.

7.4. Sensitivity to CCN concentration

The emulators were used to examine the sensitivity of cloud water and hail to the CCN concentration for different conditions by looking at all 32 possible combinations of the input parameters when two discrete values are assigned each according to Tab. 7.1. More details of the method are given in section 5.4. The results for all trigger mechanisms are presented in Fig. 6.15. The percentages given in the following paragraphs all refer to their respective maximum values.

In Fig. 7.13a the results of the warm bubble setup are shown. The integrated cloud water increases, if the CCN concentration increases where the growth is stronger for small CCN concentrations. This behavior is found in all regimes such that most of the results are located within a spread of $\pm 10\%$ of the maximum value around the mean. On average, the amount of cloud water in clean conditions is 55% of the amount observed in polluted conditions. Contrary, the integrated hail content decreases for an increasing CCN concentration. Following a linear decrease, the mean is reduced by 30% in a polluted environment. Accordingly, the maximum precipitation by hail is also decreased in polluted conditions. Here, large variations between the regimes are visible as in some cases no more hail is observed at the ground even before the maximum concentration is reached, whereas in other cases only a reduction of 25% is found. The mean is linearly reduced to 44% of the maximum value.

In the cold pool setup (Fig. 7.13b), the same trends are detected. For small CCN concentrations the integrated cloud water increases rapidly until the growth slows down at a CCN concentration of about $2000\,\mathrm{cm}^{-3}$. For the mean sensitivity the total increase is more than 40% of the maximum value. The spread of the different regimes is largest for clean conditions but is continuously reduced as the CCN concentration increases. The integrated hail content is on average reduced by 30% in polluted conditions. All of the considered regimes follow the decreasing linear trend where some develop a

(a) warm bubble

(b) cold pool
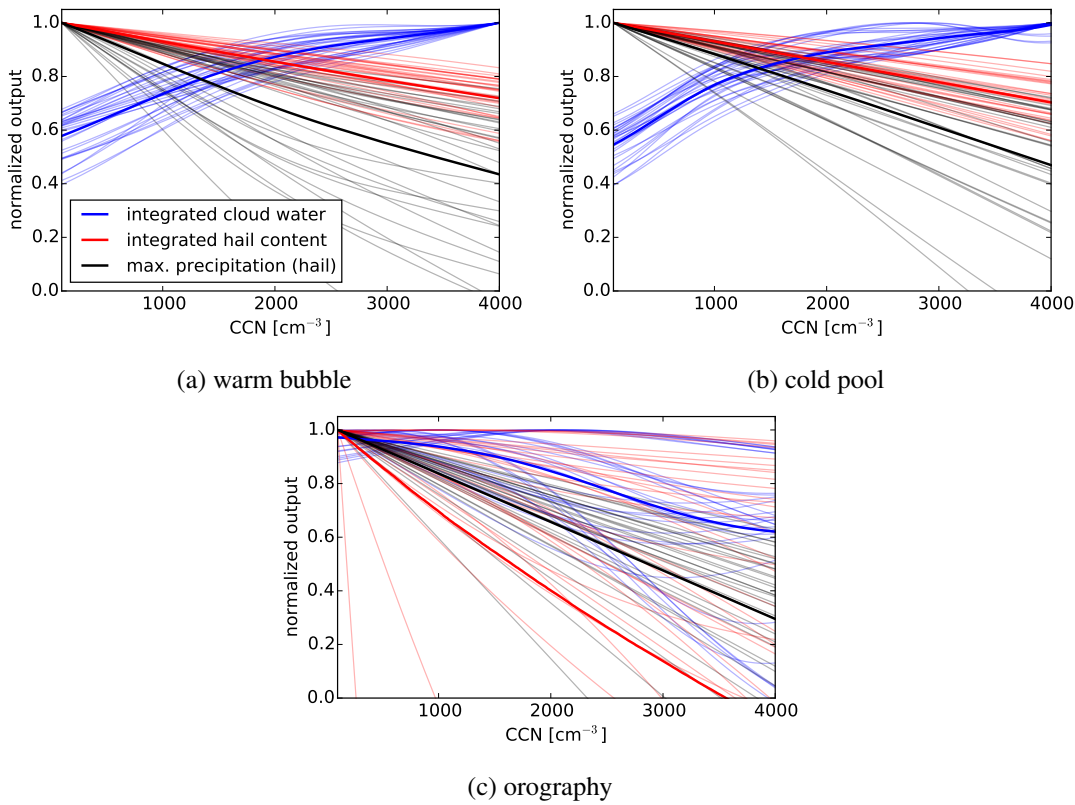
(c) orography

Fig. 7.13.: Sensitivity of mean integrated cloud water, mean integrated hail and precipitation by hail to variations in the CCN concentrations for (a) the warm bubble setup, (b) the cold pool setup, (c) the orography setup. Thin lines represent the results for 32 different environmental conditions and the bold lines denote the means.

reduction of less than 20% and others of more than 40%. Corresponding to the decline of the in-cloud hail, the amount of hail observed at the ground decreases for increasing CCN concentrations as well. The mean shows a decrease down to less than 50% of the amount found in clean conditions. However, in polluted conditions the amounts of precipitation by hail range between 0% and 70% of the maximum value. Therefore, changes of the input parameters clearly proceed to the output of the precipitation of hail as there are considerable differences between the regimes.

The sensitivities in the orography setup are most diverse. In contrast to the other two triggers the mean of the sensitivities of the integrated cloud water decreases for an increasing CCN concentration. This decrease is not as pronounced in environments with a CCN concentration of less than $2000 \, \mathrm{cm^{-3}}$, but it gets stronger in more polluted environments. In this case, the individual results differ from the mean. For example, in some regimes the cloud water increases until a maximum is reached at a CCN concentration of about $2250 \, \mathrm{cm^{-3}}$ and decreases for higher concentrations. In other regimes the initial decrease changes into an increase at CCN concentrations of $2500 - 3000 \, \mathrm{cm^{-3}}$. In particular, the mean exhibits a decrease of less than 40%. The decrease of the mean of the integrated hail content is quite distinct as it shows a complete removal of in-cloud hail in polluted conditions. However, similar to the inte-

grated cloud water the variations between the different regimes are remarkable and the amounts found in polluted conditions can take basically any value. Further, the precipitation by hail also shows a linear decrease for increasing CCN concentrations. The mean is reduced to 30% of the maximum value, but the spread between the regimes is large. So for polluted environments the amount of hail at the ground varies in a range of about 60% of the maximum value.

Summarizing, in all three setups the amount of hail, both in-cloud and at the ground, decreases as the CCN concentration rises. In the warm bubble setup and the cold pool setup, the integrated cloud water is found to increase for increasing CCN concentration, whereas in the orography setup the trend shows a decrease. However, the results of the different regimes are diverse in the orography setup so that for some of the regimes the integrated cloud water at least partly increases for more polluted conditions. The changes in the amount of the considered output between clean and polluted conditions are similar for the thermal triggers. In these two setups, the integrated cloud water in clean conditions amounts to approximately 55% of the value in polluted conditions and the values of the integrated hail content and the maximum precipitation of hail are reduced by 30% and 55%, respectively, in polluted environments. While the difference between low and high CCN concentrations of the integrated cloud water is comparable except for the sign in the orography setup, both the integrated hail content and the hail at the ground are more affected by the CCN concentration leading to smaller amounts in polluted conditions. Regarding the variance of the regimes, the sensitivity to the CCN concentration is most robust to changes of the input parameters in the cold pool setup as the spread of the regimes is low for the three considered outputs. Nevertheless, the spread in the warm bubble setup is only marginally larger such that the sensitivity to the CCN concentration is also rather robust in this setup when the input parameters are varied. In contrast, large variations between the different regimes are seen in the orography setup. Thus, the orography setup is sensitive to changes of the input parameters. This can be explained by the fact that convection over orography is influenced by various processes on different spatio-temporal scales and that it forms a complex system which is not fully understood to the present day (Schneider et al., 2018; Kirshbaum et al., 2018).

8. Comparison of the Different Emulator Studies and Discussion

While in the chapters before the focus was on the similarities and differences between the trigger mechanisms for each setup of input parameters, this chapter aims at comparing the results of the different sets of input parameters for each trigger mechanism. Thus, variations caused by changes of the set of input parameters are detectable. Especially, the alternating influence of parameters describing the environmental conditions and those describing the cloud microphysics can be analyzed. The setups in which either the environmental conditions or the microphysics are varied are referred to as S1 and S2, respectively. The setup that includes variations of both environmental conditions and microphysics is called S3.

8.1. Cloud variables and precipitation

To compare the main effects of the three emulator studies, the results are combined in a bubble plot (Fig. 8.1) where the contribution of each considered input parameter to the output uncertainty is represented by the size of a circle. The circles of the different sets of input parameters are placed in columns next to each other for the output of the cloud variables and precipitation. The results of the warm bubble setups are depicted in Fig. 8.1.

The CCN and IN concentrations are used as input parameters in all setups such that three results can be compared. The contributions from the CCN concentration to the output uncertainty of the integrated cloud water are similar in S1, S2 and S3. For the other variables, the contribution in S3 is rather comparable to the contribution in S1, while the contribution in S2 is either smaller (hail, graupel and rain contents) or larger (ice and snow contents). The trend is more consistent for the precipitation output. For all considered variables the main effect of the CCN concentration is largest in S2. Therefore, the impact of the CCN concentration is generally larger, if only the microphysics are perturbed. However, the effect of the environmental conditions is more dominant such that the result for the combined input parameters of S3 resembles the result of the study where the input parameters are environmental conditions only (S1). The contributions from the IN concentration are mostly small for the cloud variables and thus the contrast between the role of the environmental conditions and the role of the microphysics is not evidently observable. In contrast, the main effect of the IN concentration is larger in S1 than in S2 for the precipitation variables. The main effects in S3 are a compromise of S1 and S2, but the results are closer to those of S2 than to those of S1. Thus, the main effect of the IN concentration is smaller, if microphysical parameters are used as input.
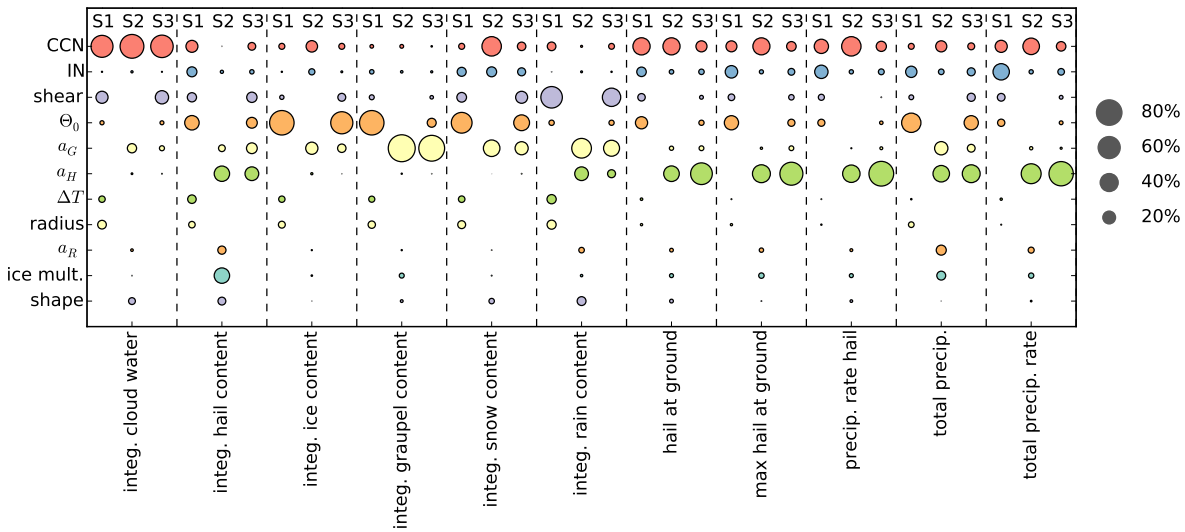
Fig. 8.1.: Bubble chart of the contributions from all input parameters of the different emulator studies to the output uncertainty of the cloud and precipitation variables when the convection is triggered by a warm bubble. The main effects of all input parameters given on the y-axis are depicted as circles where the size corresponds to the value of the main effect. The different columns labeled with S1, S2 and S3 represent the results of each emulator study (S1: environmental conditions, S2: microphysics, S3: both environmental conditions and microphysics).

The behavior of the wind shear is not consistent for the considered output variables. When looking at the integrated graupel and rain contents, the contribution to the output uncertainty from the wind shear is smaller in S3, whereas for the remaining cloud variables it is larger in S3 compared to S1. Concerning the precipitation, the contribution from the wind shear is in general smaller in S3 which means that the wind shear has a larger impact on the output uncertainty, if only the environmental conditions are varied.

In contrast to the wind shear, the result of θ_0 is the same for all output variables. While the impact of θ_0 is rather large in S1, it is clearly reduced in S3. So θ_0 is an important factor, if the effect of environmental conditions is analyzed, but compared to the effect of cloud microphysics its impact is diminished.

In general, the main effect of the fall velocity of graupel is larger for the cloud variables than for the precipitation. Furthermore, in most of the cases the fall velocity of graupel has a smaller effect on the output uncertainty in S3, but for all variables directly connected to hail (integrated hail content, mean and maximum precipitation of hail and the precipitation rate of hail) the impact on the output uncertainty is larger, if also input parameters describing environmental conditions are varied.

When looking at the cloud variables, the contribution from the fall velocity of hail to the output uncertainty is negligible except for the integrated hail and rain contents. However, it is the largest contributor to the uncertainty of the precipitation variables. Here, its impact is larger in S3 compared to S2 for all variables so that its importance expands when also environmental conditions are involved. It can be said that the uncertainty of the precipitation mainly emerges from the uncertainty of the microphysics,

in particular from the fall velocity of hail, as the contributions from the parameters characterizing the environmental conditions are rather small in S3.

The remaining input parameters are only used once so that a comparison of different studies is not possible. Still, they are included in Fig. 8.1 for completeness.

The comparison of the emulator studies for the cold pool setup is illustrated in Fig. 8.2.
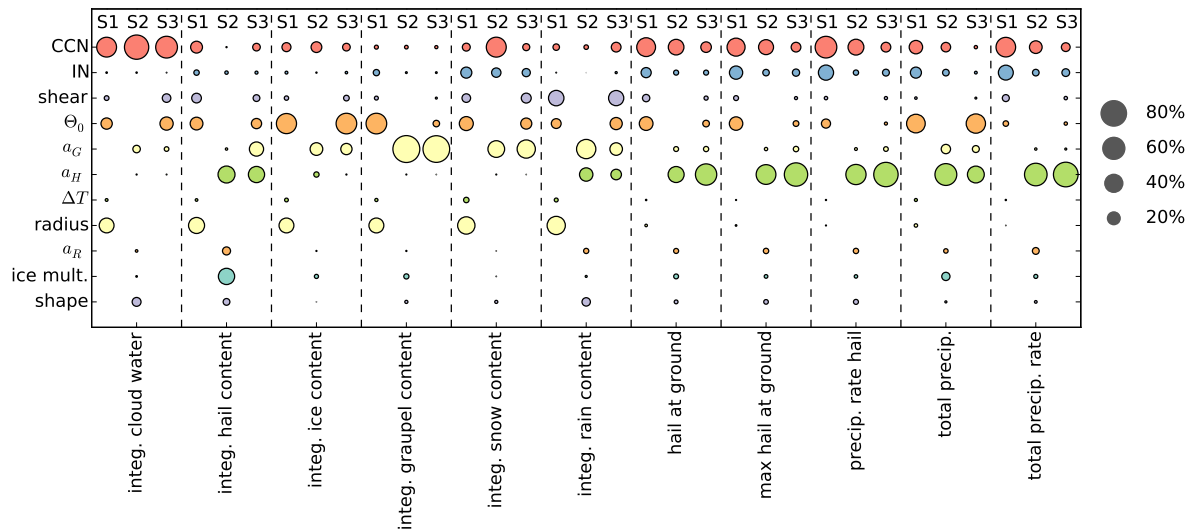
Fig. 8.2.: Bubble chart of the contributions from all input parameters of the different emulator studies to the output uncertainty of the cloud and precipitation variables when the convection is triggered by a cold pool. The main effects of all input parameters given on the y-axis are depicted as circles where the size corresponds to the value of the main effect. The different columns labeled with S1, S2 and S3 represent the results of each emulator study (S1: environmental conditions, S2: microphysics, S3: both environmental conditions and microphysics).

For S1, S2 and S3 the largest contribution from the CCN concentration is found for the output uncertainty of the integrated cloud water where the contribution in S2 is slightly larger than in S1 and S3. The other cloud variables also show that the CCN concentration contributes similar amounts to the uncertainty in S1 and S3, while the contributions in S2 are either larger (integrated cloud water, integrated ice content, integrated snow content) or smaller (integrated contents of hail, graupel and rain). So for the integrated cloud variables, the contribution from the CCN concentration of the study, in which the environment and the microphysics are perturbed, is comparable to the study that includes only parameters describing the environmental conditions. Regarding the precipitation, the impact of the CCN concentration decreases continuously such that the smallest contribution is connected to S3.

Similar to the behavior of the CCN concentration for the precipitation output, the contribution from the IN concentration is in general highest for S1 and smaller for S2 and S3. This means that the impact of the IN concentration on the output uncertainty is reduced, if perturbations of the microphysics are included in the set of input parameters.

The variations of the main effect of the wind shear due to the different sets of input parameters is almost negligible such that its effect is comparable for S1 and S3. Furthermore, this suggests that the impact of the wind shear depends only slightly on the other input parameters.

Moreover, the contributions from the potential temperature θ_0 are also comparable for S1 and S3 for the cloud variables. An exception is the integrated graupel content where θ_0 contributes less in S3. The opposite is visible for the precipitation variables. Here, the impact of θ_0 is clearly reduced in S3 except for the amount of total precipitation where the contributions of S1 and S3 are almost equal. Thus, θ_0 adds less to the uncertainty, if microphysical properties are part of the input parameters.

For the fall velocity of graupel, the relation between the result of S2 and S3 varies depending on the output variable. The main effect in S3 is larger for the integrated contents of hail and snow, the maximum amount of hail at the ground the the precipitation rate of hail, whereas the main effect is smaller in S3 for the integrated contents of cloud water, ice and rain and the total amount of precipitation. Furthermore, the contributions of S2 and S3 are similar for the integrated graupel content, the mean amount of hail at the ground and the total precipitation rate. The decrease of the contribution from θ_0 to the uncertainty of the integrated graupel content in S3 is related to the dominant main effect of the fall velocity of graupel.

Except for the integrated hail and rain contents, the contributions from the fall velocity of hail to the output uncertainties of the cloud variables are rather small, yet for all cloud outputs the results are comparable for S2 and S3. The main effect of the fall velocity of hail is larger in S3 than in S2 for the precipitation variables. This corresponds with the decrease of the main effect of the other input parameters, especially of the CCN concentration and θ_0. However, for the total amount of precipitation the contribution is smaller in S3 which is linked to the large impact of θ_0 on the total precipitation. Thus, the uncertainty of the precipitation is mainly dominated by the fall velocity of hail which means that microphysical properties influence the precipitation more than environmental conditions.

Finally, Fig. 8.3 shows the main effects of the different emulator studies for the orography setup.

The contributions from the CCN concentration to the output uncertainties of the cloud variables are rather small, but the results of S1 and S3 are mostly comparable. For the precipitation output there are various orders of the sizes of the circles visible without any regularity. For some variables, the result of S3 is close to the result of S1 (e.g. mean amount of hail at the ground) as seen for the cloud variables but for other variables the impact is largest for S1 and then decreases towards S3 (e.g. precipitation rate of hail).

The IN concentration shows the largest main effect for the cloud variables for S2, while it is smaller for S1 and S3. So, its contribution to the output uncertainty is scaled down because of the larger contributions from the input parameters characterizing the environmental conditions. Regarding the precipitation variables, the largest contribution is found for S1, while the results are comparable for S2 and S3. This means that if both types of input parameters are present, the IN concentration follows the result for the set of microphysical input parameters.
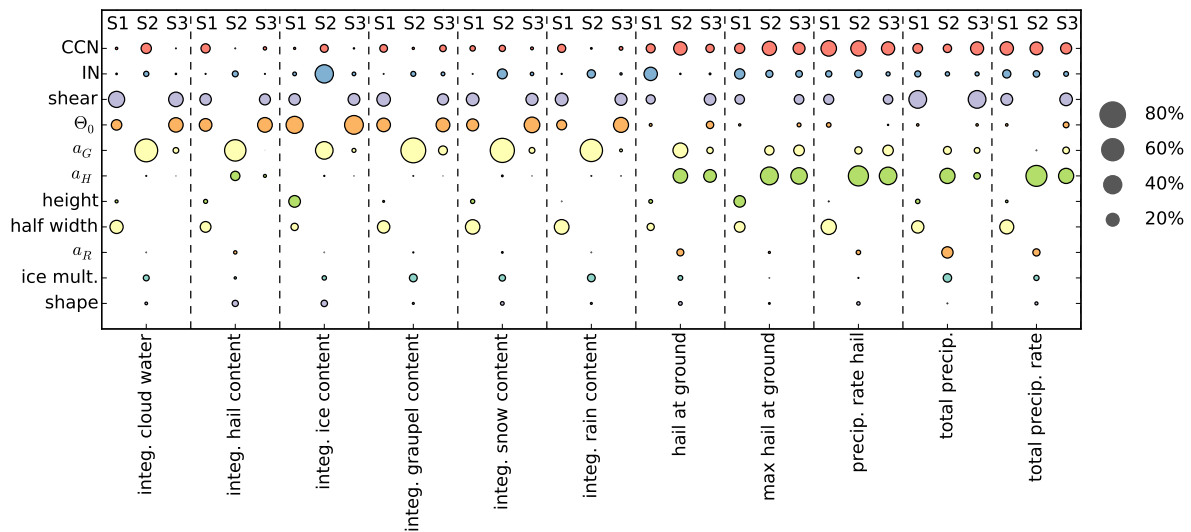
Fig. 8.3.: Bubble chart of the contributions from all input parameters of the different setups to the output uncertainty of the cloud and precipitation variables when the convection is triggered by a mountain ridge. The main effects of all input parameters given on the y-axis are depicted as circles where the size corresponds to the value of the main effect. The different columns labeled with S1, S2 and S3 represent the results of each emulator study (S1: environmental conditions, S2: microphysics, S3: both environmental conditions and microphysics).

The main effect of the wind shear is robust to changes of the set of input parameters as it is similar for S1 and S3 for all considered output variables.

The contribution from θ_0 to the output uncertainty of the cloud variables is slightly larger in S3 so that it has a greater influence than the microphysical parameters. θ_0 contributes only little to the uncertainty of the precipitation variables, but also for these variables the main effect of S3 is larger.

The main effect of the fall velocity of graupel shows strong variations between the different emulator studies. In S2 the fall velocity of graupel is the most important contributor to the output uncertainty of all cloud variables, whereas in S3 its contribution is almost negligible. In S3, the impact of the fall velocity of graupel is replaced by the contributions from the wind shear and θ_0. For the precipitation variables, the results of S3 are either larger (maximum amount of hail at the ground, precipitation rate of hail and the total precipitation rate) or smaller (mean amount of hail at the ground and total precipitation) than the results of S2.

The fall velocity of hail is not important at all for the uncertainty of the cloud variables except for the integrated hail content, whereas it is one of the largest contributors to the uncertainty of the precipitation variables. However, this contribution is decreased in S3 giving room to the effects of environmental conditions, in particular to the wind shear. As both the fall velocity of hail and the fall velocity of graupel show reduced contributions for S3, it can be concluded that the environmental conditions are a larger source of uncertainty than the microphysical parameters when a mountain ridge is used to trigger convection.

In contrast to the warm bubble and cold pool setups, the orography setup shows large interaction effects, mainly affecting the cloud variables which is already mentioned in the previous chapters. In Fig. 8.3 the interactions can be estimated from the size of all circles in each column: the larger the sum, the less interactions happen. Because of the considerable contribution to the uncertainty from the fall velocity of graupel, S2 has the least impact of interactions such that the first-order main effects are comparable to those of the warm bubble and cold pool setups. Thus, the parameters responsible for the interactions in the orography setup are connected to environmental conditions.

In the literature the focus of sensitivity studies is mainly on the effect of the CCN concentrations on clouds, but there are also studies examining the effect of other parameters such as wind shear, the temperature perturbation or the shape parameter of the cloud droplet size distribution. For example, Brooks (1992) analyses the effect of the warm bubble characteristics on deep convection. He finds that variations of ΔT cause only minor differences of the precipitation and the updrafts are strongest for medium horizontal radii of the bubble. The effect of the horizontal radius on the precipitation is not mentioned. These results are in good agreement with the findings of this work. Both ΔT and the radius of the bubble hardly contribute to the output uncertainty of the precipitation variables and also the impact on the cloud variables is rather small (Fig. 8.1). Regarding the wind shear, Dennis and Kumjian (2017) observe a significant effect of the wind shear on the hail production. Here, the contribution of the wind shear to the output uncertainties of hail variables is rather small for the warm bubble and cold pool setups, but for the orography setup the wind shear is an important contributor in both S1 and S3. It is expected to see a larger impact for the warm bubble and cold pool setup, if the wind shear does not have to compete with the more dominant effects of other parameters comparable to Dennis and Kumjian (2017). The impact of CAPE on deep convection is analyzed by Storer et al. (2010). In their study the cloud generally reacts to changes of CAPE, while in particular the integrated amount of cloud water does not depend strongly on CAPE. Furthermore, they conclude that the impacts of the CAPE and the CCN concentration are comparable. Fig. 8.1, 8.2 and 8.3 confirm that the contribution of θ_0 to the uncertainty of the integrated cloud water in S1 and S3 is not dominant. The impact of these parameters varies for each variable such that for some variables the CCN concentration is more important and for others it is θ_0. Thus, in total the effect of the two parameters is about the same, but for each considered output variable, usually only one of these parameters is dominant. A combined study dealing with both the effect of the wind shear and the CAPE is conducted by McCaul and Weisman (2001) where they find that both parameters influence the storm intensity. In the present study, the wind shear is mainly contributing to the uncertainty of the output in the orography setup, but larger contributions of θ_0 are found for all trigger mechanisms. Igel and van den Heever (2017) examine shallow cumulus clouds for different shape parameters of the cloud droplet size distribution and notice an effect on the droplet concentration, but not on the mass mixing ratios. The results of this study also agree with their work, as the shape parameter is only of minor importance for the integrated cloud variables. With respect to the aerosol effect, our findings are in good agreement with

the work of Fan et al. (2013) and Yang et al. (2017), for instance. Fan et al. (2013) observe changes of 25% of the anvil expansion due to changes of the CCN concentration and Yang et al. (2017) find clear differences in the vertically integrated condensate mixing ratio such as an increase of ice from 6 to $18\,\mathrm{g}$ kg^{-1} for increasing CCN. This is comparable to the influence of the CCN concentration on the output uncertainty found here.

8.2. Size distribution of hail

In chapters 5 , 6 and 7 it was possible to separate the size distributions of surface hail into different groups which were controlled by certain input parameters. To compare these size distributions for the different emulator studies, the clusters are extracted at a diameter of 5 mm and are plotted next to each other. So, the number concentrations of the clusters can be compared. The shading is related to the clusters defined in each of the previous three chapters and represents the different influencing parameters. The respective parameters are given by the legend and indicate which parameters are necessary for the distributions to either have a very low number concentration or a very high number concentration. This is shown in Fig. 8.4 for the results of the warm bubble setup.
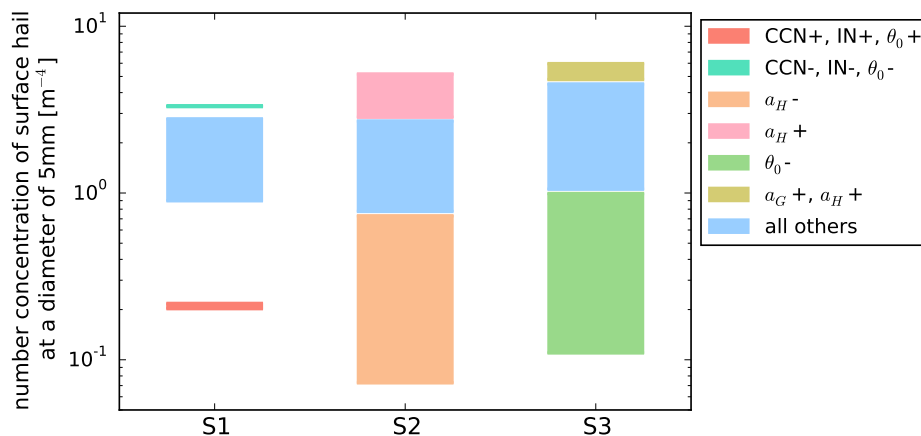
Fig. 8.4.: Number concentration of surface hail at a diameter of $d = 5$ mm when the convection is triggered by a warm bubble. The colors denote different controlling input parameters.

Most of the size distributions are associated with the groups in the middle (light blue). These groups have a similar range of number concentrations $(0.8 - 2 \ \mathrm{m}^{-4})$ for all S1, S2 and S3. However, in S3 there is a tendency towards higher concentrations as also values of up to $5\,\mathrm{m}^{-4}$ are reached by the middle cluster. In S1, the clusters showing the lowest and highest number concentrations have a very limited range compared to S2 and S3 such that the maximum number concentrations of these groups are well defined. The clusters of the extreme number concentrations have the widest ranges for S2. For example, the distributions with the highest concentrations are found in a range from $3 - 6\,\mathrm{m}^{-4}$. The clusters with the lowest and highest concentrations of S3 are comparable to these of S2, except that they are shifted to slightly higher values. Thus, microphysical parameters as input parameters lead to larger ranges of

each cluster and therefore a larger spread of the distributions. Yet, the group in the middle, where most of the distributions are found, shows higher concentrations, if parameters describing the environmental conditions are used as input parameters. Regarding the controlling parameters of the size distributions, they are the CCN concentration, the IN concentration and θ_0 for S1, the fall velocity of hail for S2 and θ_0 and the fall velocities of graupel and hail for S3. So, in the combined study S3, both environmental conditions and microphysics control the size distributions, but the microphysical parameters are those leading to high number concentrations.

The results of the three emulator studies are shown in Fig. 8.5 for the cold pool setup.
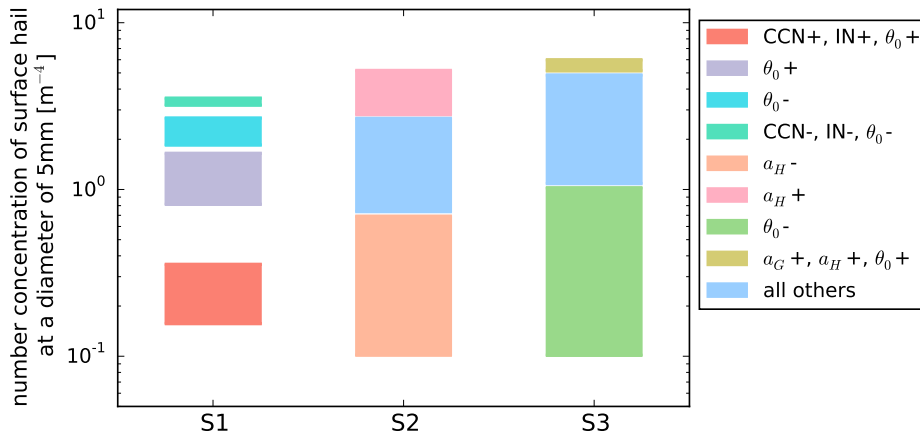
Fig. 8.5.: Number concentration of surface hail at a diameter of $d = 5$ mm when the convection is triggered by a cold pool. The colors denote different controlling input parameters.

In S1, θ_0 has a strong influence on the size distributions as the group containing most of the distributions can be separated in a part with higher concentrations characterized by a low value of θ_0 and a part with lower concentrations characterized by a high value of θ_0. These two groups together are comparable to the number concentrations of the middle cluster of S2. The corresponding cluster of S3 shows higher number concentrations. S3 also has the largest total range covering number concentrations from 0.1 m^{-4} to 6 m^{-4}. As already mentioned, the size distributions of S1 can be separated into four different groups where the extremes are controlled by the CCN concentration, the IN concentration and θ_0. The distributions with low number concentrations in S2 are controlled by a low fall velocity of hail, whereas the higher concentrations are connected to high fall velocities of hail. In S3, the rather narrow range of distributions with high number concentrations is caused by high fall velocities of graupel and hail and a high value of θ_0. In contrast, a low value of θ_0 causes the large range of lower number concentrations. Thus, also in S3 θ_0 is quite dominant influencing both the distributions with low and high concentrations. In general, the spread of the distributions is larger, if microphysical parameters are part of the input parameters. Furthermore, microphysical input parameters lead to higher number concentrations than parameters describing environmental conditions.

Fig. 8.6 compares the number concentrations at a hail diameter of 5 mm of the three emulator studies for the orography setup.
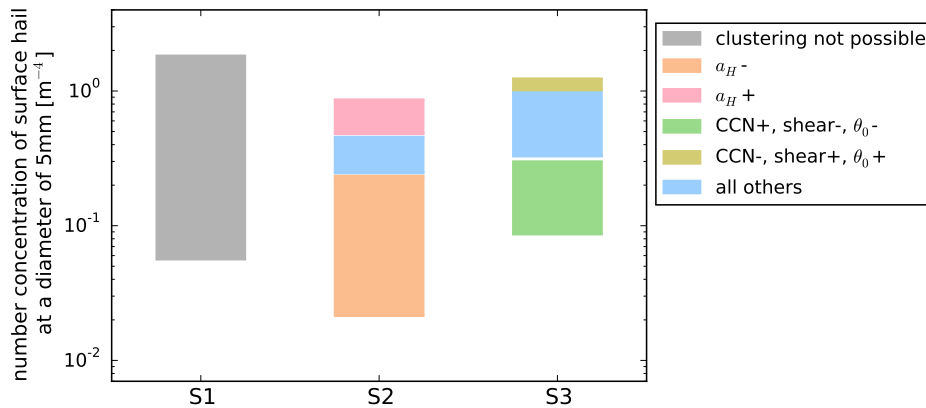
Fig. 8.6.: Number concentration of surface hail at a diameter of $d = 5$ mm when the convection is triggered by a mountain ridge. The colors denote different controlling input parameters.

The group in the middle colored in light blue containing the majority of the size distributions has higher number concentrations in S3 than in S2. Although clustering is not possible for S1, presumably the number concentration of this group is also higher as the total range of possible number concentrations is higher than in S2. Thus, a general trend towards higher concentrations is visible, if environmental conditions are part of the input parameters (S1 and S3). In S2, the quite extended lower range is characterized by a low fall velocity of hail, while the high number concentrations between $0.5\,\mathrm{m}^{-4}$ and $0.9\,\mathrm{m}^{-4}$ are linked to a high fall velocity of hail. The group with the highest number concentrations has a narrow range in S3 and is determined by the CCN concentration, the wind shear and θ_0. So, it is possible to conclude that in the orography setup the environmental conditions are more important for the size distribution of surface hail than the microphysics.

Summarizing, microphysical input parameters cause a larger spread of the number concentrations of large hail than the input of environmental conditions in the warm bubble and cold pool setups. In addition, the group with the highest number concentration is dominated by microphysical parameters such that it can be said that the microphysics are responsible for the maximum number concentration of surface hail. In contrast, the environmental conditions have the more dominant effect on the hail size distributions in the orography setup.

The results above should not be regarded as definite number concentrations as a bulk model is used here and several studies note that the representation of hydrometeor sizes is more accurate in bin schemes (Dennis and Kumjian, 2017; Lee et al., 2008). To approach this issue, Loftus and Cotton (2014) introduce a modified microphysics setup where a three-moment scheme is implemented for an improved prediction of hail. They find that increasing the CCN concentration induces an increase of the hail sizes,

but a decrease of the number of hailstones. The CCN concentration is identified as controlling parameter of the size distribution in this emulator study as well, but not for all considered setups. Since Loftus and Cotton (2014) investigate the effect of the CCN concentration only, it is possible that in the emulator study the effect of the CCN concentration is covered by larger impacts of other input parameters such as the fall velocity of hail. Thus, the classification of controlling parameters of the size distribution of hail could be appropriate although a bulk microphysics scheme is implemented in the COSMO model. Further studies similar to Loftus and Cotton (2014) incorporating modifications of the microphysics scheme and the variation of not only one but several parameters are necessary to confirm these findings.

8.3. Diabatic heating rates

Vorticity indicates the rotation of air masses due to both local effects and the rotation of the earth and is therefore necessary to describe the motion of air parcels (Etling, 2008). As it is connected to the circulation of a fluid, vorticity is conserved in barotropic conditions following Kelvin's circulation theorem. Ertel introduced a generalization, the potential vorticity (PV), which is also conserved in baroclinic conditions for adiabatic motion (Schubert et al., 2004). It is given by

$$PV = \frac{\vec{\omega}_a \cdot \nabla \theta}{\rho} \qquad [8.1]$$

where $\vec{\omega}_a$ is the absolute vorticity vector, θ is the potential temperature and ρ is the density of air. This measure is used in dynamics to trace air masses or to explain cyclogenesis. Moreover, temperature, pressure and wind fields can be derived from the distribution of PV (Hoskins et al., 1985). If diabatic processes are considered, PV is not conserved anymore. Following Hoskins et al. (1985) and Joos and Wernli (2011) the tendency can be calculated as

$$\frac{D}{Dt}PV \approx \frac{\eta_z}{\rho} \cdot \frac{\partial}{\partial z}\left(\frac{\partial T}{\partial t}\right) \qquad [8.2]$$

where η_z denotes the vertical component of the absolute vorticity. The term $\frac{\partial}{\partial z}\left(\frac{\partial T}{\partial t}\right)$ describes the diabatic heating and thus the diabatic heating rates have a an impact on the dynamics of storms. Below the maximum of heating, potential vorticity is produced while it is destroyed above (Wernli and Davies, 1997). To compare the possible impact of the heating rates on the tendency of background PV for the different emulator studies, the term $\frac{\partial}{\partial z}\left(\frac{\partial T}{\partial t}\right)$ is calculated for the total heating rate and the vertical profiles are plotted for each set of input parameters.

Fig. 8.7 illustrates the results for the warm bubble setup where the dashed lines represent the heights in which the transition from production to depletion of potential vorticity happens.
The production of potential vorticity near the ground is clearly visible as positive values and it reaches its maximum at a height of 1375 m. For S1 and S3 destruction of potential vorticity is found above $z = 4500$ m, whereas for S2 the transition is lifted to a height of almost 6000 m marking the height of
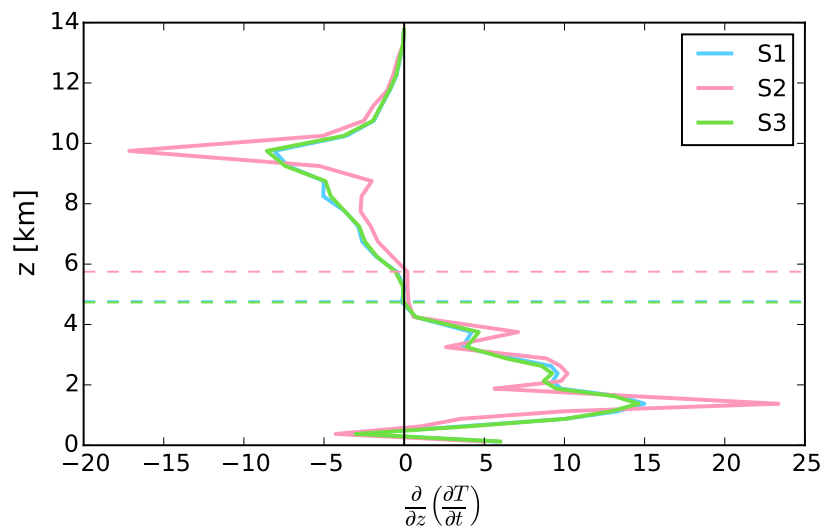
Fig. 8.7.: Vertical profiles of the tendency of potential vorticity caused by diabatic processes when the convection is triggered by a warm bubble.

maximum diabatic heating. In all studies, the reduction is largest 10 km above the ground. The profiles of S1 and S3 are almost identical throughout all height levels while the profile of S2 differs especially in the middle troposphere. Thus, in S3 the influence of the input parameters describing environmental conditions is more dominant than the effect of the microphysical parameters.

Similar results are found for the cold pool setup which are presented in Fig. 8.8.
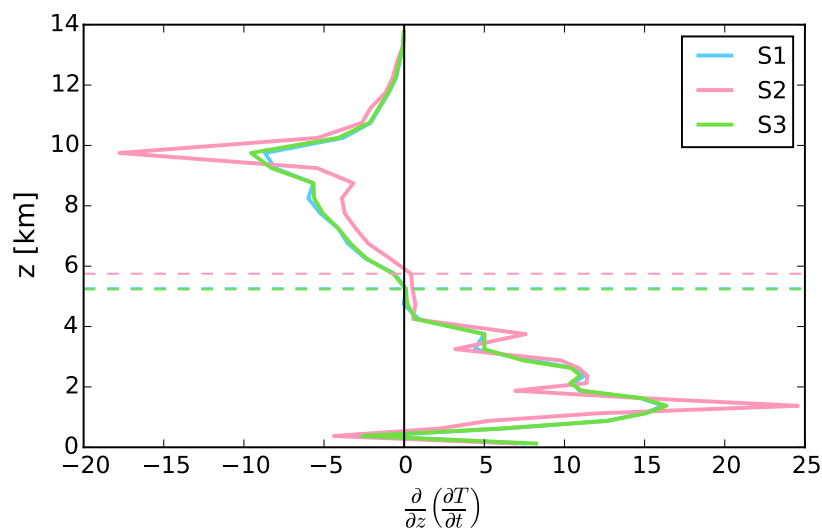
Fig. 8.8.: Vertical profiles of the tendency of potential vorticity caused by diabatic processes when the convection is triggered by a cold pool.

The profiles of all studies add to the production of potential vorticity in the lower atmosphere where the contribution is largest at $z = 1375$ m. The transition from positive to negative values is located at a height of approximately 5000 m for S1 and S3. The transition height of S2 is found above at $z = 6000$ m. Further, the maximum reduction of potential vorticity is at a height of 10 km for all studies. As already seen for the results of the warm bubble setup, the profiles of S1 and S3 are quite similar, whereas the profile of S2 only roughly follows the trend of S1 and S3 having the maximum production and depletion at the same heights. Yet, details are different as S2 shows larger peaks and deviates from the other profiles above a height of 6 km. Therefore, these results indicate that the environmental conditions have a stronger influence on the diabatic heating rates than microphysical parameters as the profile of S3 is similar to that of S1.

Fig. 8.9 shows the vertical profiles of the three emulator studies for the orography setup.
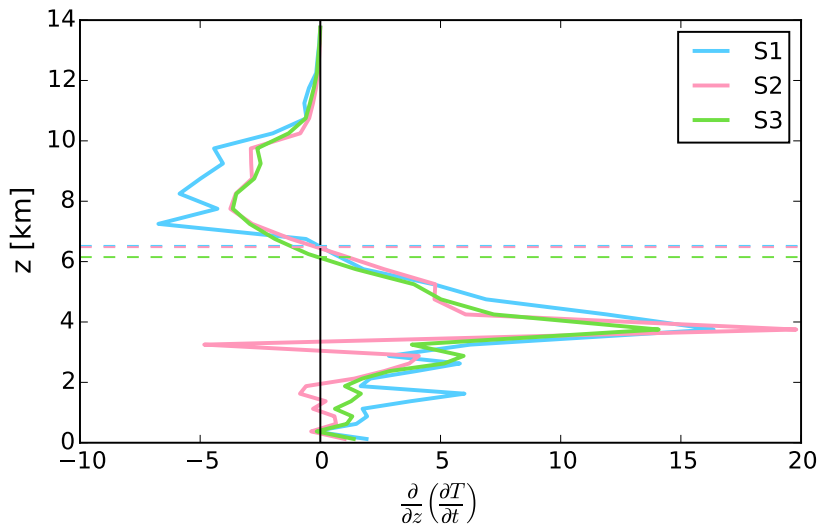
Fig. 8.9.: Vertical profiles of the tendency of potential vorticity caused by diabatic processes when the convection is triggered by a mountain ridge.

The production of potential vorticity near the ground has its maximum at a height of 3750 m for all studies and the depletion of potential vorticity is most dominant at $z = 7250$ m for S1 and at $z = 7750$ m for S2 and S3. The change from positive to negative values between these two extremes is at the lowest height for S3 (~ 6000 m). For S1 and S2 production of potential vorticity is found up to a height of 6500 m. Apart from the same height of the maximum, the profiles of the three studies are diverse in the lower troposphere. Above the transition from positive to negative values, the profiles of S2 and S3 approach each other and are in fairly good agreement. It appears as if in the lower troposphere the profile of S3 is a compromise of both S1 and S2, whereas it is closer to the profile of S2 in the upper troposphere. Thus, unlike the warm bubble and cold pool setups, there is no prevailing effect of either the environmental conditions or the microphysics on the diabatic heating rates.

Besides the vertical profiles of the heating rates, the temporal evolution of the conversion rates is analyzed in chapters 5.3, 6.3 and 7.3. Fan et al. (2017) find that in mixed-phase orographic clouds depositional growth of hydrometeors is more important than riming. Although in this study deep convective clouds are analyzed, similar characteristics are identified. Except for hail where riming has a larger conversion rate, deposition has a higher contribution to the generation of graupel, snow and ice than riming processes. Yet, for S2 the conversion rates of deposition and riming are almost equal for the warm bubble and cold pool setups. Moreover, there are no major differences between the different studies for each trigger mechanism, rather there is a feature that the results have in common: the impact of the saturation adjustment. For all sets of input parameters and all triggers the saturation adjustment is the prevailing process having the highest conversion rate. Hence, the diabatic heating related to cloud water is a substantial contributor to the total heating rate in the lower and middle troposphere. Wang et al. (2013) find that there are discrepancies of the results between models including saturation adjustment and those explicitly calculating diffusional growth of cloud droplets. These differences are mainly characterized by an overestimation of the condensation in the lower troposphere affecting the diabatic heating rates. In addition, Lebo et al. (2012) also state that saturation adjustment artificially increases condensation. This increase appears to be quite strong as it is also represented by the emulators. Therefore, modified results of the sensitivity studies are expected for the heating rates, if the saturation adjustment is replaced by more realistic calculations. However, Dennis and Kumjian (2017) specify in their work that process rates are not an essential factor causing discrepancies in the formation of hail for different model setups.

Furthermore, Houze (1989) examines the structure of idealized mesoscale convective systems including vertical profiles of the heating rates. Comparing the profiles generated by the emulator with the results of Houze (1989) excluding radiative processes shows that the vertical structure in all cases includes cooling near the ground and heating above with the maximum located in the middle troposphere. However, the maximum rates of Houze (1989) are about six times higher than the rates found here as the domain mean of the heating rates is considered. In addition, the impact of the saturation adjustment on the heating rates is visible as the transition from cooling to heating happens in Houze (1989) at a height of approximately 4 km which is comparable to the cooling caused by evaporation of rain in this study. But because of the large contribution from the heating caused by the formation of cloud droplets the total heating rate strongly increases, leading to positive values at lower heights. Nevertheless, the emulators are able to reproduce heating rates comparable to other studies.

8.4. Sensitivity to CCN concentration

In general, the mean sensitivities of integrated cloud water, integrated hail content and the maximum precipitation of hail to the CCN concentration show the same trends for the emulator studies of each trigger.

Yet, there are differences in the individual sensitivities of the regimes defined by different combinations of the input parameters.

For the warm bubble setup, the integrated cloud water is increasing and both the in-cloud hail and the precipitation by hail are decreasing for increasing CCN concentration regardless of the parameters used as input. An exception is S2 where the integrated hail content is insensitive to changes of the CCN concentration. So, the results of S1 and S3 are more alike. However, neither the environmental conditions nor the microphysics have a dominant effect in S3.

Similarly, the amount of integrated cloud water increases while the hail decreases for polluted conditions in the cold pool setup. In addition, the integrated hail content does not respond greatly to variations of the CCN concentration and the spread of the sensitivities of the different regimes of input parameters is larger in S2. Accordingly, the mean sensitivities of S3 are rather comparable to those of S1 but the spread of the results of the different regimes of S3 tends towards the spread of S2 combining effects of both the environmental conditions and the microphysics.

In the orography setup, an increase of cloud water and a decrease of hail are found for an increasing CCN concentration, too. However, a decrease of cloud water for polluted conditions is detected in S3, although both S1 and S2 show an increase. Thus, this could be caused by the emulator fit. In contrast to the warm bubble and cold pool setups, the spread is smaller in S2 than in S1 and S3 such that using environmental conditions as input parameters leads to a higher variability in the orography setup.

Many studies investigate the aerosol effect on clouds and precipitation for different conditions and the results are quite diverse. For example, Tao et al. (2007) simulate deep convective cloud systems over Oklahoma, Florida and the Pacific and see a suppression of precipitation for the storm in Oklahoma, whereas an enhancement of rain is observed for the storm over the Pacific if the CCN concentration is increased. Furthermore, Morrison (2012) analyze an idealized supercell storm with different microphysical or thermodynamical processes turned on or off. Depending on this composition, they notice either a weakening or an invigoration of the storm for an increased number of CCN. Lee et al. (2008) investigate how the sensitivity to the CCN concentration depends on the CAPE and the wind shear. They find that for high CAPE and strong wind shear the precipitation increases for polluted conditions, whereas it decreases for low CAPE and low wind shear. The results of this study only partly agree with these results of Lee et al. (2008). Instead of the total precipitation, the precipitation by hail is examined here, yet the mean of all different considered regimes indicates a clear decrease of hail at the ground for polluted conditions. There are deviations of the individual regimes from the mean trend revealing certain ranges of the CCN concentration where the amount of hail increases. However, this is mainly the case in S2 where neither the θ_0 nor the wind shear is varied. Nevertheless, the results of Lee et al. (2008) support the detection of a spread of the individual results specifying a dependency of the sensitivity to the CCN concentration on the initial conditions of the model setup.

Apart from that, the results of Loftus and Cotton (2014) indicate that there are more numerous and smaller cloud droplets for an increasing CCN concentration, but the hail mass is reduced for both low and high CCN concentrations having a maximum at medium concentrations. On the one hand, for these results here an increased amount of cloud water for polluted conditions is found as well. On the other hand, the mean trend of the hail mass shows a decrease for increasing CCN. Some individual results of the considered regimes differ from the mean and display a higher amount of hail for medium CCN concentrations, however a decrease towards low CCN concentrations is not seen.

Furthermore, these results are in good agreement with the findings of Noppel et al. (2010) where the COSMO model is used as well. They simulate a hailstorm for different CCN concentrations and see that the total precipitation decreases for an increasing CCN concentration. Simultaneously, Khain et al. (2011) simulate the same storm and obtain opposite results. This study shows that the discrepancy between Noppel et al. (2010) and Khain et al. (2011) can neither be explained by variations of the environmental conditions nor the microphysical parameters, as the results of the different regimes are not as diverse as necessary to support both the hypothesis of an increase and a decrease. Therefore, the divergence of the results is probably caused by the approach used for the calculation of the microphysics. Khain et al. (2011) implement a spectral bin model, whereas Noppel et al. (2010) employ a bulk model. Here, the same bulk model is used and thus the results of Noppel et al. (2010) are reproduced. An effect of the microphysics scheme on the precipitation is also assumed by Fan et al. (2017).

9. Conclusions and Outlook

9.1. Conclusions

The aim of this work was to determine the effect of environmental conditions and perturbations of the model microphysics on deep convective clouds focusing on three key questions introduced in chapter 1:

- Which parameters primarily cause uncertainty in the prediction of convective cloud parameters? In particular also of hail occurrence and size?
  Depending on the considered output, different input parameters are responsible for the uncertainty. In general, the CCN and IN concentrations, the wind shear, θ_0 and the fall velocities of graupel and hail are identified as important parameters contributing to the output uncertainty. Regarding hail and its size distribution in particular, the CCN concentration, the fall velocity of hail and θ_0 cause uncertainty in the prediction.

- How much are the diabatic heating rates affected by variations of the input parameters?
  The mean vertical profiles of the heating rates are quite robust as changes of the input parameters result in small standard deviations.

- Are the results robust for different trigger mechanisms of deep convection?
  The results of the sensitivity analyses vary for each trigger mechanism. The results of the warm bubble and cold pool setups are comparable, while the results of the orography setup differ.

To address these questions, the COSMO model was used to simulate deep convective clouds in an idealized setup. The convection was either triggered by a warm bubble, a cold pool or a mountain ridge. Thus, a comparison of the results for the various triggers was possible. The straightforward approach for analyzing the sensitivity of the model output to changes in the input parameters is to vary a chosen parameter in a given range, while the other parameters are kept constant. However, instead of this one-at-a-time analysis, statistical emulation and variance-based sensitivity analysis were employed where the contributions of the input parameters to the uncertainty of the output are quantified. Therefore, the simulations of the COSMO model were used to train the emulators, while the variance-based sensitivity was based on the predictions of the emulators allowing for an identification of not only the impact of each parameter independently, but also their interactions which cannot by captured by one-at-a-time analyses. In total, three sets of input parameters were evaluated. First, a set describing environmental conditions such as potential temperature and wind shear was used. The second set of input parameters focused on

cloud microphysics consisting of parameters such as the shape parameter of the cloud droplet size distribution or the fall velocity of graupel. Based on the findings of the two previous sets of input parameters, the third set combined influential parameters of both environmental conditions and microphysics. For all trigger mechanisms and all sets of input parameters, the integrated hydrometeor contents, the precipitation, the size distribution of surface hail and diabatic heating rates were examined with respect to output uncertainty and response to variations of the input.

The analysis reveals that, in general, environmental conditions and the microphysics have a comparable impact for the warm bubble and cold pool setups. Parameters of both sets contribute to the output uncertainty of the cloud variables in the combined set, especially the CCN concentration, θ_0 and the fall velocity of graupel. Furthermore, for input parameters describing the environmental conditions the size distribution of surface hail is controlled by the CCN concentration and θ_0, while it is controlled by the fall velocity of hail when microphysical parameters are used as input. For the third set of input parameters θ_0 and the fall velocity of hail are determining the number concentration and thus both environmental conditions and microphysics have a similar effect on the hail size distribution. Also the variability of the vertical profiles of the diabatic heating rates is comparable for all sets of input parameters. Additionally, they show a small standard deviation and are therefore quite robust to modifications of the input parameters. However, there are two exceptions where either environmental conditions or the microphysics are more dominant than the other. On the one hand, microphysics have a larger impact on the precipitation as especially the fall velocity of hail adds substantially to the output uncertainty of these variables for the third set of input parameters. On the other hand, the output uncertainty of the total heating rate is controlled by environmental conditions even if there are also microphysical parameters included in the input.

In contrast, the environmental conditions, especially the wind shear, are the dominant parameters for the orography setup. For the combined set of input parameters, the wind shear contributes considerably to the output uncertainties of all output variables of interest. Regarding the size distribution of surface hail, various parameters are adding to the uncertainty for the first set of input parameters such that no governing parameters can be identified. Yet, for the set of input parameters combining environmental conditions and microphysics, the controlling parameters of the hail size distribution are the CCN concentration, the wind shear and θ_0. Thus, only parameters describing the environmental conditions characterize the size distribution for the last set of input parameters, although the fall velocity of hail, which is the controlling parameter for the set of microphysical inputs, is part of this input set as well. Moreover, there is a large variability of the vertical profiles of the heating rates, if environmental conditions are part of the input parameters. Accordingly, the standard deviations are high for the first and the last set of input parameters while it is comparable to those of the warm bubble and cold pool setups for the second set of input parameters where the microphysics are perturbed. As a consequence, changes of the environment influence the heating rates more prominently than changes of the microphysics. But

there is an exception from the dominance of the environmental conditions: Similarly to the warm bubble and cold pool setups, the fall velocity of hail and thus the microphysical input parameters are the largest source of uncertainty for the precipitation.

Summarizing, we see that the results depend on the trigger mechanism, where the largest differences are found between the orography setup and the thermal triggers. So far, sensitivity studies have usually been conducted using a single method to trigger convection (Storer et al., 2010; Adams-Selin et al., 2013; Chen and Lin, 2005) and thus the same sensitivities have not been compared for different trigger mechanisms. These results indicate that sensitivities found for one trigger mechanism cannot be completely transferred to other triggers. Part of the differences can be attributed to the structure of the initial convection in the orography setup where several cells are triggered along the mountain ridge compared to the warm bubble and cold pool setups where single cells are triggered. However, there are also differences between the warm bubble setup and the cold pool setup. This limits the transferability of identified sensitivities to real-case simulations, in which all three trigger mechanisms can happen in modified forms.

Concluding, statistical emulation enables a dense sampling of the whole parameter space in a short amount of time and thus a comprehensive sensitivity analysis. The quantification and comparison of contributions from input parameters to the output uncertainty would have not been possible without these methods. However, in the process information is lost because mean and maximum values are used in this analysis. In future studies this problem could be reduced by multivariate emulation (Hankin, 2012; Overstall and Woods, 2016), where multiple variables are fitted with a single emulator. Such emulators are more difficult to generate as further specifications must be made as to how the multiple output variables depend on each other, which are not always known. Furthermore, an emulator is not a replacement for a numerical model based on physical equations, yet the validation ensures that the specific relation between input and output described by each emulator is well represented. In the present work, deep convective clouds have been considered in idealized setups only. The results are expected to depend on assumptions in the two-moment scheme such as the use of saturation adjustment. Thus, the sensitivities might vary for real case simulations. Overall the emulator approach appears to be a powerful tool for the analysis of complex weather prediction models, and is recommended for further use.

9.2. Outlook

This work combined various independent sensitivity studies (see chapter 2) into a single study and showed that, depending on the output of interest, different parameters contribute to the uncertainty. Although the impact of the CCN concentration is a focus of current research, the results revealed that other parameters have comparable contributions to the output uncertainty which should be investigated in more detail. For example, the contribution of the fall velocity of hail to the uncertainty of precipitation

is similar or rather larger than that of the CCN concentration. As the relation of size and fall speed of hydrometeors is parameterized in numerical weather prediction models, a significant reduction of the uncertainty of the precipitation forecast could be achieved, if the parameterizations were improved. This study showed that the results of the orography setup differ from those of the warm bubble and cold pool setups. Therefore, detailed model simulations could be performed in future studies to identify the cause of the discrepancies. Furthermore, a bulk microphysics scheme was used here to calculate the size distribution of hail, but several studies suggest that a more realistic representation of the size distributions is obtained for a bin microphysics scheme (Lee et al., 2008; Loftus and Cotton, 2014; Dennis and Kumjian, 2017). Thus, a similar analysis of the size distribution could be repeated for a bin scheme to inspect whether the sensitivities are also affected by the use of different microphysics schemes.

Moreover, the emulator approach and the variance-based sensitivity analysis can be used to identify those parameters causing the largest uncertainty in the output. Thus, the number of important parameters can be reduced based on the findings of the sensitivity analysis. As the emulator requires a single output value, such as mean or maximum values, it is not possible to determine which of the processes the considered parameters are involved in are responsible for the output uncertainty. However, the identification of the essential contributing parameters and the associated reduction of the number of parameters makes a conventional sensitivity study, where full model simulations are analyzed, feasible. Therefore, detailed model simulations should be performed in a next step to understand the sources of the contributions to the output uncertainties at process level (Fig. 9.1).
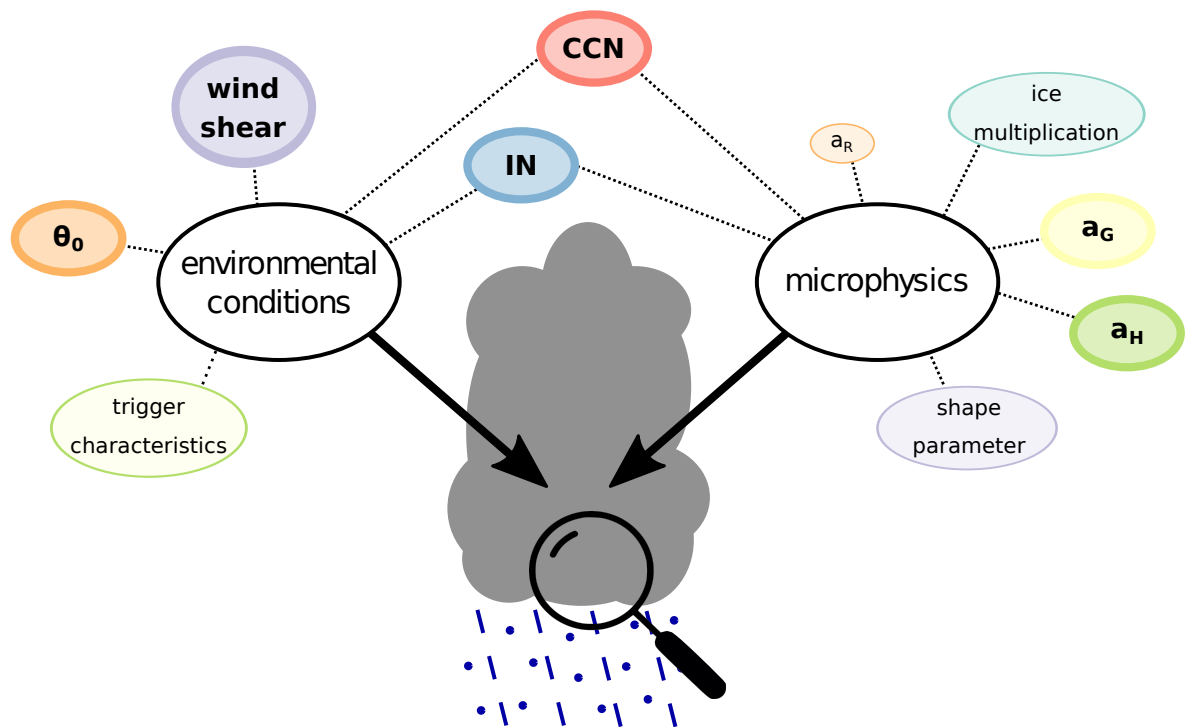
Fig. 9.1.: Schematic overview of the sensitivity studies conducted in this thesis including results and an outlook. The parameters that are identified to contribute most to the output uncertainties are highlighted by bold text and thick lines. In future studies the processes responsible for the uncertainties could be determined.

A. List of Figures

B. List of Tables

C. Bibliography

Adams-Selin, R. D., van den Heever, S. C., and Johnson, R. H.: Impact of Graupel Parameterization Schemes on Idealized Bow Echo Simulations, Monthly Weather Review, 141, 1241–1262, doi: 10.1175/MWR-D-12-00064.1, 2013.

Baldauf, M., Seifert, A., Förstner, J., Majewski, D., Raschendorfer, M., and Reinhardt, T.: Operational Convective-Scale Numerical Weather Prediction with the COSMO Model: Description and Sensitivities, Monthly Weather Review, 139, 3887–3905, doi:10.1175/MWR-D-10-05013.1, 2011.

Bastos, L. S. and O'Hagan, A.: Diagnostics for Gaussian Process Emulators, Technometrics, 51, 425–438, doi:10.1198/TECH.2009.08019, 2009.

Bigg, E. K.: The formation of atmospheric ice crystals by the freezing of droplets, Quarterly Journal of the Royal Meteorological Society, 79, 510–519, doi:10.1002/qj.49707934207, 1953.

Bluestein, H. B.: Severe convective storms and tornadoes : observations and dynamics, Springer-Praxis in Books in Environmental Sciences, Springer, Berlin;Heidelberg [u.a.], 2013.

Boose, Y., Kanji, Z. A., Kohn, M., Sierau, B., Zipori, A., Crawford, I., Lloyd, G., Bukowiecki, N., Herrmann, E., Kupiszewski, P., Steinbacher, M., and Lohmann, U.: Ice Nucleating Particle Measurements at 241 K during Winter Months at 3580 m MSL in the Swiss Alps, Journal of the Atmospheric Sciences, 73, 2203–2228, doi:10.1175/JAS-D-15-0236.1, 2016.

Bougiatioti, A., Fountoukis, C., Kalivitis, N., Pandis, S. N., Nenes, A., and Mihalopoulos, N.: Cloud condensation nuclei measurements in the marine boundary layer of the Eastern Mediterranean: CCN closure and droplet growth kinetics, Atmospheric Chemistry and Physics, 9, 7053–7066, doi: 10.5194/acp-9-7053-2009, 2009.

Brooks, H.: Operational implications of the sensitivity of modeled thunderstorms to thermal perturbations, Fourth AES/CMOS Workshop on Operational Meteorology, 110, 398–407, 1992.

Brooks, H. E. and Wilhelmson, R. B.: Numerical simulation of a low-precipitation supercell thunderstorm, Meteorology and Atmospheric Physics, 49, 3–17, doi:10.1007/BF01025398, 1992.

Chen, S.-H. and Lin, Y.-L.: Effects of Moist Froude Number and CAPE on a Conditionally Unstable Flow over a Mesoscale Mountain Ridge, Journal of the Atmospheric Sciences, 62, 331–350, doi: 10.1175/JAS-3380.1, 2005.

Connolly, P. J., Choularton, T. W., Gallagher, M. W., Bower, K. N., Flynn, M. J., and White-way, J. A.: Cloud-resolving simulations of intense tropical Hector thunderstorms: Implications for aerosol–cloud interactions, Quarterly Journal of the Royal Meteorological Society, 132, 3079–3106, doi:10.1256/qj.05.86, 2006.

Crosier, J., Bower, K. N., Choularton, T. W., Westbrook, C. D., Connolly, P. J., Cui, Z. Q., Crawford, I. P., Capes, G. L., Coe, H., Dorsey, J. R., Williams, P. I., Illingworth, A. J., Gallagher, M. W., and Blyth, A. M.: Observations of ice multiplication in a weakly convective cell embedded in supercooled mid-level stratus, Atmospheric Chemistry and Physics, 11, 257–273, doi:10.5194/acp-11-257-2011, 2011.

Cui, Z., Carslaw, K. S., Yin, Y., and Davies, S.: A numerical study of aerosol effects on the dynamics and microphysics of a deep convective cloud in a continental environment, Journal of Geophysical Research: Atmospheres, 111, doi:10.1029/2005JD005981, 2006.

Cui, Z., Davies, S., Carslaw, K. S., and Blyth, A. M.: The response of precipitation to aerosol through riming and melting in deep convective clouds, Atmospheric Chemistry and Physics, 11, 3495–3510, doi:10.5194/acp-11-3495-2011, 2011.

Davies-Jones, R.: A review of supercell and tornado dynamics, Atmospheric Research, 158-159, 274 – 291, doi:https://doi.org/10.1016/j.atmosres.2014.04.007, 2015.

de Boer, G., Hashino, T., and Tripoli, G. J.: Ice nucleation through immersion freezing in mixed-phase stratiform clouds: Theory and numerical simulations, Atmospheric Research, 96, 315 – 324, doi: https://doi.org/10.1016/j.atmosres.2009.09.012, 2010.

DeMott, P. J., Prenni, A. J., Liu, X., Kreidenweis, S. M., Petters, M. D., Twohy, C. H., Richardson, M. S., Eidhammer, T., and Rogers, D. C.: Predicting global atmospheric ice nuclei distributions and their impacts on climate, Proceedings of the National Academy of Sciences, 107, 11 217–11 222, doi: 10.1073/pnas.0910818107, 2010.

Dennis, E. J. and Kumjian, M. R.: The Impact of Vertical Wind Shear on Hail Growth in Simulated Supercells, Journal of the Atmospheric Sciences, 74, 641–663, doi:10.1175/JAS-D-16-0066.1, 2017.

Doms, G. and Baldauf, M.: A Description of the Nonhydrostatic Regional COSMO-Model, Part I: Dynamics and Numerics, Deutscher Wetterdienst (DWD), Offenbach, Germany, 2015.

Dusek, U., Frank, G. P., Hildebrandt, L., Curtius, J., Schneider, J., Walter, S., Chand, D., Drewnick, F., Hings, S., Jung, D., Borrmann, S., and Andreae, M. O.: Size Matters More Than Chemistry for Cloud-Nucleating Ability of Aerosol Particles, Science, 312, 1375–1378, doi:10.1126/science.1125261, 2006.

Etling, D., ed.: Theoretische Meteorologie : Eine Einführung, SpringerLink : Bücher, Springer Berlin Heidelberg, Berlin, Heidelberg, 3. erweiterte und aktualisierte auflage edn., 2008.

Fan, J., Leung, L. R., Rosenfeld, D., Chen, Q., Li, Z., Zhang, J., and Yan, H.: Microphysical effects determine macrophysical response for aerosol impacts on deep convective clouds, Proceedings of the National Academy of Sciences, 110, E4581–E4590, doi:10.1073/pnas.1316830110, 2013.

Fan, J., Leung, L. R., Rosenfeld, D., and DeMott, P. J.: Effects of cloud condensation nuclei and ice nucleating particles on precipitation processes and supercooled liquid in mixed-phase orographic clouds, Atmospheric Chemistry and Physics, 17, 1017–1035, doi:10.5194/acp-17-1017-2017, URL https://www.atmos-chem-phys.net/17/1017/2017/, 2017.

Gal-Chen, T. and Somerville, R. C.: On the use of a coordinate transformation for the solution of the Navier-Stokes equations, Journal of Computational Physics, 17, 209–228, doi:10.1016/0021-9991(75)90037-6, 1975.

Hallet, J. and Mossop, S. C.: Production of secondary ice particles during the riming process, Nature, 249, 26–28, doi:10.1038/249026a0, 1974.

Hankin, R.: Introducing multivator: A Multivariate Emulator, Journal of Statistical Software, Articles, 46, 1–20, doi:10.18637/jss.v046.i08, 2012.

Harris-Hobbs, R. L. and Cooper, W. A.: Field Evidence Supporting Quantitative Predictions of Secondary Ice Production Rates, Journal of the Atmospheric Sciences, 44, 1071–1082, doi:10.1175/1520-0469(1987)044<1071:FESQPO>2.0.CO;2, 1987.

Hobbs, P. V. and Rangno, A. L.: Ice Particle Concentrations in Clouds, Journal of the Atmospheric Sciences, 42, 2523–2549, doi:10.1175/1520-0469(1985)042<2523:IPCIC>2.0.CO;2, 1985.

Hobbs, P. V., Politovich, M. K., and Radke, L. F.: The Structures of Summer Convective Clouds in Eastern Montana. I: Natural Clouds, Journal of Applied Meteorology, 19, 645–663, doi:10.1175/1520-0450(1980)019<0645:TSOSCC>2.0.CO;2, 1980.

Hoskins, B. J., McIntyre, M. E., and Robertson, A. W.: On the use and significance of isentropic potential vorticity maps, Quarterly Journal of the Royal Meteorological Society, 111, 877–946, doi:10.1002/qj.49711147002, 1985.

Houze, R. A.: Observed structure of mesoscale convective systems and implications for large-scale heating, Quarterly Journal of the Royal Meteorological Society, 115, 425–461, doi:10.1002/qj.49711548702, 1989.

Houze, R. A.: Cloud dynamics, International geophysics series ; 53, Academic Press, San Diego [u.a.], 1993.

Huffman, P. J. and Vali, G.: The Effect of Vapor Depletion on Ice Nucleus Measurements with Membrane Filters, Journal of Applied Meteorology, 12, 1018–1024, doi:10.1175/1520-0450(1973)012<1018:TEOVDO>2.0.CO;2, 1973.

Igel, A. L. and van den Heever, S. C.: The Importance of the Shape of Cloud Droplet Size Distributions in Shallow Cumulus Clouds. Part II: Bulk Microphysics Simulations, Journal of the Atmospheric Sciences, 74, 259–273, doi:10.1175/JAS-D-15-0383.1, 2017.

Igel, A. L., Igel, M. R., and van den Heever, S. C.: Make It a Double? Sobering Results from Simulations Using Single-Moment Microphysics Schemes, Journal of the Atmospheric Sciences, 72, 910–925, doi:10.1175/JAS-D-14-0107.1, 2015.

James, R. P., Markowski, P. M., and Fritsch, J. M.: Bow Echo Sensitivity to Ambient Moisture and Cold Pool Strength, Monthly Weather Review, 134, 950–964, doi:10.1175/MWR3109.1, 2006.

Johnson, J. S., Cui, Z., Lee, L. A., Gosling, J. P., Blyth, A. M., and Carslaw, K. S.: Evaluating uncertainty in convective cloud microphysics using statistical emulation, Journal of Advances in Modeling Earth Systems, 7, 162–187, doi:10.1002/2014MS000383, 2015.

Joos, H. and Wernli, H.: Influence of microphysical processes on the potential vorticity development in a warm conveyor belt: a case-study with the limited-area model COSMO, Quarterly Journal of the Royal Meteorological Society, 138, 407–418, doi:10.1002/qj.934, 2011.

Khain, A., Rosenfeld, D., Pokrovsky, A., Blahak, U., and Ryzhkov, A.: The role of CCN in precipitation and hail in a mid-latitude storm as seen in simulations using a spectral (bin) microphysics model in a 2D dynamic frame, Atmospheric Research, 99, 129–146, doi:10.1016/j.atmosres.2010.09.015, 2011.

Kirshbaum, D. J., Adler, B., Kalthoff, N., Barthlott, C., and Serafin, S.: Moist Orographic Convection: Physical Mechanisms and Links to Surface-Exchange Processes, Atmosphere, 9, doi:10.3390/atmos9030080, 2018.

Knight, N. C. and Heymsfield, A. J.: Measurement and Interpretation of Hailstone Density and Terminal Velocity, Journal of the Atmospheric Sciences, 40, 1510–1516, doi:10.1175/1520-0469(1983)040<1510:MAIOHD>2.0.CO;2, 1983.

Kunz, M., Blahak, U., Handwerker, J., Schmidberger, M., Punge, H. J., Mohr, S., Fluck, E., and Bedka, K. M.: The Severe Hailstorm in SW Germany on 28 July 2013 : Characteristics, Impacts, and Meteorological Conditions, Quarterly journal of the Royal Meteorological Society, 144, 231–250, doi:10.1002/qj.3197, 2018.

Lamb, D. and Verlinde, J.: Physics and chemistry of clouds, Cambridge University Press, Cambridge, 2011.

Lebo, Z. J., Morrison, H., and Seinfeld, J. H.: Are simulated aerosol-induced effects on deep convective clouds strongly dependent on saturation adjustment?, Atmospheric Chemistry and Physics, 12, 9941–9964, doi:10.5194/acp-12-9941-2012, URL https://www.atmos-chem-phys.net/12/9941/2012/, 2012.

Lee, L. A., Carslaw, K. S., Pringle, K. J., Mann, G. W., and Spracklen, D. V.: Emulation of a complex global aerosol model to quantify sensitivity to uncertain parameters, Atmospheric Chemistry and Physics, 11, 12 253–12 273, doi:10.5194/acp-11-12253-2011, 2011.

Lee, L. A., Pringle, K. J., Reddington, C. L., Mann, G. W., Stier, P., Spracklen, D. V., Pierce, J. R., and Carslaw, K. S.: The magnitude and causes of uncertainty in global model simulations of cloud condensation nuclei, Atmospheric Chemistry and Physics, 13, 8879–8914, doi:10.5194/acp-13-8879-2013, 2013.

Lee, S. S., Donner, L. J., Phillips, V. T. J., and Ming, Y.: The dependence of aerosol effects on clouds and precipitation on cloud system organization, shear and stability, Journal of Geophysical Research: Atmospheres, 113, doi:10.1029/2007JD009224, 2008.

Locatelli, J. D. and Hobbs, P. V.: Fall speeds and masses of solid precipitation particles, Journal of Geophysical Research, 79, 2185–2197, doi:10.1029/JC079i015p02185, 1974.

Loeppky, J. L., Sacks, J., and Welch, W. J.: Choosing the Sample Size of a Computer Experiment: A Practical Guide, Technometrics, 51, 366–376, doi:10.1198/TECH.2009.08040, 2009.

Loftus, A. and Cotton, W.: Examination of CCN impacts on hail in a simulated supercell storm with triple-moment hail bulk microphysics, Atmospheric Research, 147-148, 183 – 204, doi:https://doi.org/10.1016/j.atmosres.2014.04.017, URL http://www.sciencedirect.com/science/article/pii/S0169809514001999, 2014.

McCaul, E. W. and Weisman, M. L.: The Sensitivity of Simulated Supercell Structure and Intensity to Variations in the Shapes of Environmental Buoyancy and Shear Profiles, Monthly Weather Review, 129, 664–687, doi:10.1175/1520-0493(2001)129<0664:TSOSSS>2.0.CO;2, URL https://doi.org/10.1175/1520-0493(2001)129<0664:TSOSSS>2.0.CO;2, 2001.

Morris, M. D. and Mitchell, T. J.: Exploratory designs for computational experiments, Journal of Statistical Planning and Inference, 43, 381–402, doi:10.1016/0378-3758(94)00035-T, 1995.

Morrison, H.: On the robustness of aerosol effects on an idealized supercell storm simulated with a cloud system-resolving model, Atmospheric Chemistry and Physics, 12, 7689–7705, doi:10.5194/acp-12-7689-2012, 2012.

Noppel, H., Blahak, U., Seifert, A., and Beheng, K. D.: Simulations of a hailstorm and the impact of CCN using an advanced two-moment cloud microphysical scheme, Atmospheric Research, 96,

286–301, doi:10.1016/j.atmosres.2009.09.008, 15th International Conference on Clouds and Precipitation, 2010.

Oakley, J. E. and O'Hagan, A.: Probabilistic sensitivity analysis of complex models: a Bayesian approach, Journal of the Royal Statistical Society: Series B (Statistical Methodology), 66, 751–769, doi:10.1111/j.1467-9868.2004.05304.x, 2004.

O'Hagan, A., ed.: Kendalls advanced theory of statistics, vol. 2B: Bayesian inference, Arnold, London, 2. edn., 2004.

O'Hagan, A.: Bayesian analysis of computer code outputs: A tutorial, Reliability Engineering & System Safety, 91, 1290–1300, doi:10.1016/j.ress.2005.11.025, 2006.

Overstall, A. M. and Woods, D. C.: Multivariate emulation of computer simulators: model selection and diagnostics with application to a humanitarian relief model, Journal of the Royal Statistical Society: Series C (Applied Statistics), 65, 483–505, doi:10.1111/rssc.12141, URL https://rss.onlinelibrary.wiley.com/doi/abs/10.1111/rssc.12141, 2016.

Phillips, V. T. J., Donner, L. J., and Garner, S. T.: Nucleation Processes in Deep Convection Simulated by a Cloud-System-Resolving Model with Double-Moment Bulk Microphysics, Journal of the Atmospheric Sciences, 64, 738–761, doi:10.1175/JAS3869.1, URL https://doi.org/10.1175/JAS3869.1, 2007.

Phillips, V. T. J., Yano, J.-I., Formenton, M., Ilotoviz, E., Kanawade, V., Kudzotsa, I., Sun, J., Bansemer, A., Detwiler, A. G., Khain, A., and Tessendorf, S. A.: Ice Multiplication by Breakup in Ice–Ice Collisions. Part II: Numerical Simulations, Journal of the Atmospheric Sciences, 74, 2789–2811, doi: 10.1175/JAS-D-16-0223.1, 2017.

Pruppacher, H. R. and Klett, J. D.: Microphysics of clouds and precipitation, Atmospheric and oceanographic sciences library ; 18, Kluwer, Dordrecht [u.a.], 1997.

Pujol, G., Iooss, B., with contributions from Khalid Boumhaout, A. J., Veiga, S. D., Delage, T., Fruth, J., Gilquin, L., Guillaume, J., Le Gratiet, L., Lemaitre, P., Nelson, B. L., Monari, F., Oomen, R., Ramos, B., Roustant, O., Song, E., Staum, J., Touati, T., and Weber, F.: sensitivity: Global Sensitivity Analysis of Model Outputs, URL https://CRAN.R-project.org/package=sensitivity, r package version 1.15.0, 2017.

R Core Team: R: A Language and Environment for Statistical Computing, R Foundation for Statistical Computing, Vienna, Austria, URL https://www.R-project.org/, 2017.

Rasmussen, C. E.: Gaussian Processes in Machine Learning, in: Advanced Lectures on Machine Learning: ML Summer Schools 2003, Canberra, Australia, February 2 - 14, 2003, Tübingen, Germany,

August 4 - 16, 2003, Revised Lectures, edited by Bousquet, O., von Luxburg, U., and Rätsch, G., pp. 63–71, Springer Berlin Heidelberg, Berlin, Heidelberg, doi:10.1007/978-3-540-28650-9_4, 2004.

Rasmussen, C. E. and Williams, C. K. I.: Gaussian Processes for Machine Learning, MIT Press, London, 2006.

Rosenfeld, D., Lohmann, U., Raga, G. B., O'Dowd, C. D., Kulmala, M., Fuzzi, S., Reissell, A., and Andreae, M. O.: Flood or Drought: How Do Aerosols Affect Precipitation?, Science, 321, 1309–1313, doi:10.1126/science.1160606, 2008.

Rotunno, R. and Klemp, J.: On the Rotation and Propagation of Simulated Supercell Thunderstorms, Journal of the Atmospheric Sciences, 42, 271–292, doi:10.1175/1520-0469(1985)042<0271:OTRAPO>2.0.CO;2, 1985.

Roustant, O., Ginsbourger, D., and Deville, Y.: DiceKriging, DiceOptim: Two R Packages for the Analysis of Computer Experiments by Kriging-Based Metamodeling and Optimization, Journal of Statistical Software, Articles, 51, 1–55, doi:10.18637/jss.v051.i01, 2012.

Saltelli, A., Tarantola, S., and Chan, K. P.-S.: A Quantitative Model-Independent Method for Global Sensitivity Analysis of Model Output, Technometrics, 41, 39–56, doi:10.1080/00401706.1999.10485594, 1999.

Saltelli, A. H., ed.: Sensitivity analysis, Wiley paperback series, Wiley, Chichester [u.a.], paperback edn., 2008.

Schättler, U., Doms, G., and Schraff, C.: A description of the nonhydrostatic regional COSMO-model, Part VII: User's Guide, 2016.

Schlesinger, R. E.: A Three-Dimensional Numerical Model of an Isolated Thunderstorm: Part I. Comparative Experiments for Variable Ambient Wind Shear, Journal of the Atmospheric Sciences, 35, 690–713, doi:10.1175/1520-0469(1978)035<0690:ATDNMO>2.0.CO;2, 1978.

Schneider, L., Barthlott, C., Barrett, A. I., and Hoose, C.: The precipitation response to variable terrain forcing over low mountain ranges in different weather regimes, Quart. J. Roy. Meteorol. Soc., doi: 10.1002/qj.3250, 2018.

Schubert, W., Ruprecht, E., Hertenstein, R., Nieto Ferreira, R., Taft, R., Rozoff, C., Ciesielski, P., and Kuo, H.-C.: English translations of twenty-one of Ertel's papers on geophysical fluid dynamics, Meteorologische Zeitschrift - METEOROL Z, 13, doi:10.1127/0941-2948/2004/0013-0527, 2004.

Segal, Y. and Khain, A.: Dependence of droplet concentration on aerosol conditions in different cloud types: Application to droplet concentration parameterization of aerosol conditions, Journal of Geophysical Research: Atmospheres, 111, doi:10.1029/2005JD006561, 2006.

Seifert, A. and Beheng, K. D.: A two-moment cloud microphysics parameterization for mixed-phase clouds. Part 1: Model description, Meteorology and Atmospheric Physics, 92, 45–66, doi:10.1007/s00703-005-0112-4, 2006a.

Seifert, A. and Beheng, K. D.: A two-moment cloud microphysics parameterization for mixed-phase clouds. Part 2: Maritime vs. continental deep convective storms, Meteorology and Atmospheric Physics, 92, 67–82, doi:10.1007/s00703-005-0113-3, 2006b.

Storer, R. L., van den Heever, S. C., and Stephens, G. L.: Modeling Aerosol Impacts on Convective Storms in Different Environments, Journal of the Atmospheric Sciences, 67, 3904–3915, doi:10.1175/2010JAS3363.1, 2010.

SwissRe: Sigma: Natural catastrophes and man-made disasters in 2013, Tech. rep., Swiss Re Economic Research & Consulting, 2014.

Tao, W., Li, X., Khain, A., Matsui, T., Lang, S., and Simpson, J.: Role of atmospheric aerosol concentration on deep convective precipitation: Cloud resolving model simulations, Journal of Geophysical Research: Atmospheres, 112, doi:10.1029/2007JD008728, 2007.

Tao, W., Chen, J., Li, Z., Wang, C., and Zhang, C.: Impact of aerosols on convective clouds and precipitation, Reviews of Geophysics, 50, doi:10.1029/2011RG000369, 2012.

Wang, Y., Fan, J., Zhang, R., Leung, L. R., and Franklin, C.: Improving bulk microphysics parameterizations in simulations of aerosol effects, Journal of Geophysical Research: Atmospheres, 118, 5361–5379, doi:10.1002/jgrd.50432, 2013.

Weisman, M. and Klemp, J.: The Dependence of Numerically Simulated Convective Storms on Vertical Wind Shear and Buoyancy, Monthly Weather Review, 110, 504–520, 1982.

Weisman, M. L. and Klemp, J. B.: The Structure and Classification of Numerically Simulated Convective Stormsin Directionally Varying Wind Shears, Monthly Weather Review, 112, 2479–2498, doi:10.1175/1520-0493(1984)112<2479:TSACON>2.0.CO;2, 1984.

Weisman, M. L. and Rotunno, R.: The Use of Vertical Wind Shear versus Helicity in Interpreting Supercell Dynamics, Journal of the Atmospheric Sciences, 57, 1452–1472, doi:10.1175/1520-0469(2000)057<1452:TUOVWS>2.0.CO;2, 2000.

Weisman, M. L., Skamarock, W. C., and Klemp, J. B.: The Resolution Dependence of Explicitly Modeled Convective Systems, Monthly Weather Review, 125, 527–548, doi:10.1175/1520-0493(1997)125<0527:TRDOEM>2.0.CO;2, 1997.

Wellmann, C., Barrett, A. I., Johnson, J. S., Kunz, M., Vogel, B., Carslaw, K. S., and Hoose, C.: Using Emulators to Understand the Sensitivity of Deep Convective Clouds and Hail to Environmental Conditions, Journal of Advances in Modeling Earth Systems, 10, 3103–3122, doi:10.1029/2018MS001465, 2018.

Wernli, B. H. and Davies, H. C.: A lagrangian-based analysis of extratropical cyclones. I: The method and some applications, Quarterly Journal of the Royal Meteorological Society, 123, 467–489, doi:10.1002/qj.49712353811, URL https://rmets.onlinelibrary.wiley.com/doi/abs/10.1002/qj.49712353811, 1997.

Weyl, H.: Mean Motion, American Journal of Mathematics, 60, 889–896, 1938.

Wicker, L. J. and Skamarock, W. C.: Time-Splitting Methods for Elastic Models Using Forward Time Schemes, Monthly Weather Review, 130, 2088–2097, doi:10.1175/1520-0493(2002)130<2088:TSMFEM>2.0.CO;2, 2002.

Yang, H., Xiao, H., Guo, C., Wen, G., Tang, Q., and Sun, Y.: Comparison of aerosol effects on simulated spring and summer hailstorm clouds, Advances in Atmospheric Sciences, 34, 877–893, doi: 10.1007/s00376-017-6138-y, 2017.

Yuter, S. E., Kingsmill, D. E., Nance, L. B., and Löffler-Mang, M.: Observations of Precipitation Size and Fall Speed Characteristics within Coexisting Rain and Wet Snow, Journal of Applied Meteorology and Climatology, 45, 1450–1464, doi:10.1175/JAM2406.1, 2006.

D. Acknowledgments

I thank Tobias Höfler for proof reading the thesis and pointing me to potential questions of non-meteorologists.

I thank my family and friends for their continuous support during my studies, entertaining conversations while having a never-ending brunch and fun activities outside of science.

My biggest thank you goes to my husband David, the best I could ask for.